CHALMERS

FE analyses of horizontal deformations due to excavation processes in deep layers of soft Gothenburg clay

- The importance of fabric anisotropy and small strain stiffness in the modeling of realistic soil behavior

Master of Science Thesis in the Master's Programme Infrastructure and Environmental Engineering

SIMON DAWD
RASMUS TRYGG

Department of Civil and Environmental Engineering
Division of GeoEngineering
Geotechnical Engineering Research Group

CHALMERS UNIVERSITY OF TECHNOLOGY
Göteborg, Sweden 2013
Master's Thesis 2013:80

MASTER'S THESIS 2013:80

FE analyses of horizontal deformations due to excavation processes in deep layers of soft Gothenburg clay

- The importance of fabric anisotropy and small strain stiffness in the modeling of realistic soil behavior

Master of Science Thesis in the Master's Programme Infrastructure and Environmental Engineering

SIMON DAWD

RASMUS TRYGG

Department of Civil and Environmental Engineering
Division of GeoEngineering
Geotechnical Engineering Research Group
CHALMERS UNIVERSITY OF TECHNOLOGY
Göteborg, Sweden 2013

FE analyses of horizontal deformations due to excavation processes in deep layers of soft Gothenburg clay
- The importance of fabric anisotropy and small strain stiffness in the modeling of realistic soil behavior

- The importance of fabric anisotropy and small strain stiffness in the modeling of realistic soil behavior

Master of Science Thesis in the Master's Programme Infrastructure and Environmental Engineering

SIMON DAWD

RASMUS TRYGG

Examensarbete / Institutionen för bygg- och miljöteknik,
Chalmers tekniska högskola 2013

Department of Civil and Environmental Engineering
Division of GeoEngineering
Geotechnical Engineering Research Group
Chalmers University of Technology
SE-412 96 Göteborg
Sweden
Telephone: + 46 (0)31-772 1000

Cover:
The intersection between the double railway bridge and the excavation for the final redrawing of the road E45, at Lärjeholm, Gothenburg.

Chalmers Reproservice
Göteborg, Sweden 2013

Finite element analyses of horizontal deformations due to excavation processes in deep layers of soft Gothenburg clay
- The importance of fabric anisotropy and small strain stiffness in the modeling of realistic soil behavior

- *The importance of fabric anisotropy and small* strain stiffness in the modeling of realistic soil behavior
Master of Science Thesis in the Master's Programme Infrastructure and Environmental Engineering

SIMON DAWD

RASMUS TRYGG

Department of Civil and Environmental Engineering
Division of GeoEngineering
Geotechnical Engineering Research Group
Chalmers University of Technology

ABSTRACT

The project has had two main aims. The first has been to examine whether it is possible to increase the degree to which predicted horizontal deformations, simulated in the finite element software Plaxis 2D, correlate to inclinometer readings, compared to previously conducted investigations regarding soil movement around two excavations at Lärjeholm, Gothenburg. The second objective has been to investigate the impact, which the modeling of fabric anisotropy and soil behavior at small strains, has on the predictions of the horizontal soil deformations in the clay at the site, and also whether the anisotropic soil model S-CLAY1, which until now has not been used in an analysis of an unloading problem, manage to produce realistic results in this context. The other models used in the simulations have included modified Cam clay, Hardening Soil and HS Small, the latter of which was used due to its implementation of the Small-Strain Overlay model, accounting for higher soil stiffness at small strains. The findings of the report included indications that anisotropy and soil behavior at small strains has a significant impact on the predicted horizontal deformations, but also that the degree to which the modeling of the two phenomena contribute to improved results, is largely dependent on the accuracy of input parameters, as well as the type of problem being analyzed.

Key words: Unloading, Clay, Excavation, Horizontal deformations, Inclinometer readings, Lärjeholm, Gothenburg, Plaxis 2D, HS Small, S-CLAY1, Anisotropy, Small-strain stiffness, Compression index, Swelling index

Finita element-analyser av horisontella deformationer som följd av schaktningsarbete vid mäktiga lager av lös Göteborgslera
- Betydelsen av anisotropi och jordstyvhet vid små töjningar för modellering av realistiskt jordbeteende

Examensarbete inom masterprogrammet Infrastructure and Environmental Engineering

SIMON DAWD

RASMUS TRYGG

Institutionen för bygg- och miljöteknik
Avdelningen för Geologi och geoteknik
Forskargruppen för geoteknik
Chalmers tekniska högskola

SAMMANFATTNING

Ändamålet med denna rapport har inkluderat två delsyften. Det första har varit att undersöka om det är möjligt att öka korrelationsgraden mellan simulerade horisontella deformationer, utförda i det finita element-programmet Plaxis 2D, och uppmätta inklinometerrörelser, i jämförelse med resultat från en tidigare genomförd utredning gällande markrörelser runt två schakter i närheten av Lärjeholm, Göteborg. Det andra delsyftet har varit att undersöka vilken betydelse jordens anisotropi, samt dess beteende vid små töjningar, har vid modellering av horisontella markdeformationer i leran på den aktuella platsen, samt även om den anisotropa jordmodellen S-CLAY1, som hittills inte har använts i en analys av ett avlastningsproblem, lyckas producera realistiska resultat i detta sammanhang. De modeller som har använts i simuleringarna har, förutom S-CLAY1, varit modified Cam clay, Hardening Soil och HS Small, där den senare användes på grund av dess implementering av Small-Strain Overlay-modellen, som tar hänsyn till högre jordstyvhet vid små töjningar. Slutsatserna i rapporten innefattar indikationer om att anisotropi samt jordens beteende vid små töjningar har en betydande inverkan på förutspådda horisontella jorddeformationer, men även att graden till vilken modellering av de två fenomenen bidrar till förbättrade resultat i hög grad är beroende av korrektheten i ingångsparametrar, liksom vilken typ av problem som analyseras.

Nyckelord: Avlastning, Lera, Schaktning, Horisontella jorddeformationer, Inklinometermätningar, Lärjeholm, Göteborg, Plaxis 2D, HS Small, S-CLAY1, Anisotropi, Styvhet vid små töjningar, Kompressionsindex, Svällningsindex

Table of Content

Preface

This MSc-thesis was conducted at the unit for geotechnical engineering at Norconsult, Gothenburg, between January 18th and June 5th in 2013. It was written on behalf of both Norconsult and the Geotechnical Engineering Research Group at the division of GeoEngineering at Chalmers University of Technology.

We would like to express our gratitude to our supervisor at Chalmers, Professor Minna Karstunen, for all the help we received in the form of lectures at her office during the autumn in 2012, and for the supervision she provided us during the work with this thesis.

We would also like to direct our appreciation to Bernhard Gervide Eckel, team leader at the unit of Geotechnical Engineering, Norconsult, who made this thesis possible through his interest in our ideas regarding numerical modelling within geotechnical engineering.

The last persons we would like to thank is our supervisor at Norconsult, Joel Wessman, who helped us with many of the problems we encountered throughout the project, during our time spent at the Norconsult office, as well as Araz Ismail, who guided us through the pre-investigation of the project, analyzed in this thesis.

Gothenburg, June 2013

Simon Dawd and Rasmus Trygg

Notations

Upper case Roman letters

C_C	Compression index	[-]
C_S	Swelling index	[-]
E	Young's modulus	[kPa]
E_0	Initial- or small-strain Young's modulus (HS Small)	[kPa]
E_{50}	Secant modulus (Hardening Soil model [HS])	[kPa]
E_{oed}	Oedometric modulus (HS)	[kPa]
E_{ur}	Unloading-reloading modulus (HS)	[kPa]
E_{50}^{ref}	Reference Secant modulus (HS)	[kPa]
E_{oed}^{ref}	Reference Oedometric modulus (HS)	[kPa]
E_{ur}^{ref}	Reference Unloading-reloading modulus (HS)	[kPa]
G	Shear modulus	[-]
G_0	Initial- or small-strain shear modulus (HS Small)	[kPa]
G_s	Specific gravity	[kg/m^3]
G_{ur}	Unloading shear modulus	[kPa]
G_0^{ref}	Reference Initial- or small-strain modulus (HS Small)	[kPa]
G_{ur}^{ref}	Reference unloading shear modulus (HS)	[kPa]
H	Stress dependent hardening modulus (HS)	[kPA]
I_P	Plasticity index	[%]
K	Bulk modulus	[kPa]
K_0	Earth pressure coefficient	[-]
$K_{0,x}$	Earth pressure coefficient for over consolidated clay	[-]
K_0^{NC}	Earth pressure coefficient for normal consolidated soil	[-]
M	Slope of the Critical State Line	[-]
M_0	Oedometric modulus for over-consolidated soil	[kPa]
M_L	Oedometric modulus for normal consolidated soil	[kPa]
$M_{compression}$	Slope of critical state line for triaxial compression	[-]
$M_{extension}$	Slope of critical state line for triaxial extension	[-]
$M_{plain-strain}$	Slope of critical state line in plain strain	[-]
OCR	Over-consolidation ratio	[-]
V_S	Volume of solids in a sample	[m^3]
V_V	Volume of voids in a sample	[m^3]

Lower case Roman letters

a	Parameter controlling rate of erasure of bonds (S-CLAY1S)	[-]
b	Parameter controlling rate of erasure of bonds (S-CLAY1S)	[-]
c	Cohesion	[kPa]
c_u	Undrained shear strength	[kPa]
c'	Effective cohesion	[kPa]
e	Void Ratio	[-]
e_0	Initial void ratio	[-]
f	Function of yield locus	[-]
f_c	Function for yield cap (HS)	[-]
f_s	Function for deviatoric yield line (HS)	[-]
g	Plastic potential	[-]
h_i	Parameter for plastic hardening at initial loading (HS Small)	[-]
k_x	Horizontal permeability	[m/day]
k_y	Vertical permeability	[m/day]
m	Exponent for stress dependency of moduli (HS)	[-]
p'	Mean effective stress	[kPa]
p'_0	Mean effective pre-consolidation stress	[kPa]
p_c	Mean effective pre-consolidation stress (HS)	[kPa]
p_p	Hardening parameter for volumetric compression (HS)	[kPa]
p'_m	Mean effective pre-consolidation stress (S-CLAY1)	[kPa]
p'_{mi}	Intrinsic value of p'_m (S-CLAY1S)	[kPa]
p^{ref}	Reference pressure	[kPa]
$p_{ref=100\ kPa}$	Plaxis default reference pressure	[kPa]
q	Deviatoric stress	[kPa]
q_a	Asymptotic value for shear strength (HS)	[kPa]
s'	Mean effective stress in plain-strain conditions	[kPa]
t	Shear stress	[kPa]
ν	Specific volume	[-]
w	Water content	[%]
w_0	Initial water content	[%]
x	Parameter for amount of bonding in a soil	[-]

Lower case Greek letters

α	Rotational hardening parameter (S-CLAY1)	[-]
α_{K0}	Initial inclination of yield locus (S-CLAY1)	[-]
β	Parameter controlling rotation of yield locus (S-CLAY1)	[-]
γ	Shear strain	[%]
γ	Unit weight	[kg/m^3]
$\gamma_{0.7}$	Threshold shear strain at which $G \approx G_0$ (HS Small)	[%]
γ_c	Threshold shear strain after which $G=G_{ur}$ (HS Small)	[%]
γ^{ps}	Hardening parameter for shearing (HS)	[%]
$\delta\varepsilon_p^e$	Increment of elastic volumetric strain	[%]
$\delta\varepsilon_q^e$	Increment of elastic deviatoric strain	[%]
$\delta\varepsilon_p^p$	Increment of plastic volumetric strain	[%]
$\delta\varepsilon_q^p$	Increment of plastic deviatoric strain	[%]
ε_1^p	Plastic strains in the direction of major principal stress	[%]
ε_v^p	Plastic volumetric strains	[%]
η	Stress ratio	[-]
η_{K0}	Stress rate for K_0-compression	[-]
κ	Slope of unloading-reloading line [url]	[-]
κ^*	Modified swelling index	[-]
λ	Inclination of isotropic normal compression line [iso-ncl]	[-]
λ^*	Modified compression index	[-]
λ_i	Slope of intrinsic compression line (S-CLAY1S)	[-]
$d\lambda$	Plastic multiplier (S-CLAY1)	[-]
$d\lambda^c$	Plastic multiplier for compression hardening (HS)	[-]
$d\lambda^s$	Plastic multiplier for shear hardening (HS)	[-]
μ	Parameter controlling rotation of yield locus (S-CLAY1)	[-]
υ	Poisson's ratio	[-]
υ_{ur}	Poisson's ratio for unloading	[-]
σ_1'	Major principal effective stress	[kPa]
σ_2'	Intermediate principal effective stress	[kPa]
σ_3'	Minor principal effective stress	[kPa]
σ^{ref}	Reference stress	[kPa]
φ	Friction angle	[$^\circ$]
φ'	Effective friction angle	[$^\circ$]
Ψ	Dilatancy angle	[$^\circ$]

1 INTRODUCTION

In 2011, during the reconstruction and expansion of the railway stretch between Gothenburg and Trollhättan, the existing road E45 was preliminarily diverted, at Lärjeholm, before being redrawn with a new alignment, under a pair of newly constructed railway bridges. For this reason, excavations were conducted in the area (Kvick, 2012). The unloading brought about by this intervention lead to unpredicted horizontal movement in the soil, causing minor dislocations in the foundation supporting the new bridges, and subsequently to stresses in the bridge structure. The behavior of soil resulting from extensive excavation processes may be challenging to predict, and can be a concern in large infrastructure projects. Consequently, there is a need for the use of advanced soil models and approaches of analysis, to enable reliable predictions of soil deformations.

As part of the geotechnical survey for the project E13, *Ismail & Teshome* performed an investigation on behalf of Norconsult, included in their MSc degree, regarding the predicted horizontal soil deformations due to the excavation for the preliminary road, constructed for the diversion of traffic. The investigation focused on finding an appropriate unloading modulus, and the simulations, executed in Plaxis 2D, showed fairly good correlation with the measured horizontal movement in the upper parts of the soil profile, whilst the deformations at depths exceeding 15 meters were noticeably over-estimated. In a subsequent degree project, completed in 2012, *Kvick* investigated the suppressive effect that the bridge's foundation had on the development of horizontal deformations in the vicinity of two of the project's excavated areas. In the report, results from simulations in Plaxis 3D indicated that the impact of the foundation was particularly apparent close to the ground surface, while at larger depths, the deformations were not dramatically altered by the inclusion of a foundation in the finite element model.

In this MSc thesis, measurements documented during the previous projects, as well as results from laboratory investigations, have been used, along with four soil models, in a series of numerical analyses in the software Plaxis 2D. The soil models which were selected for the study are Hardening Soil, HS Small, modified Cam clay and S-CLAY1. The goal of the investigation has been to find which soil model, and set of input parameters, is best in capturing the observed soil behavior, for the two excavations assessed in the previous two MSc-projects.

1.1 Purpose & Objectives

The purpose of this MSc thesis is to investigate whether it is possible to improve the simulation results from the previously performed 2D analyses, to more accurately represent the measured horizontal deformations observed at the site of the project E13, by using additional soil models together with a more detailed soil division. Special attention has been given to the choice of the unloading-reloading stiffness, as well as to the effect of fabric anisotropy and soil behavior at small strains.

The stages of the investigation can be condensed into a number of objectives as follow:

- To establish a basis for understanding of the selected soil models, including the basics of, and some of the advantages associated with, their formulation.

- To assess results from laboratory soil tests and field measurements, with focus put on the evaluation of soil layer division and soil characteristics, as well as on input parameters required for the selected soil models, and to subsequently create revised conceptual models of the soil profiles of interest.

- To specify the procedure for two different methods used in the evaluation of stiffness parameters required for each of the four soil models.

- To perform simulations with the four soil models on the cross-section of the excavation assessed in the MSc-thesis by *Ismail and Teshome* (2011), and to subsequently execute additional simulations, using the best evaluation method for soil stiffness, on a section of the excavation made for the new alignment of the road, previously investigated by *Kvick* (2012).

- To evaluate the deformation curves from each simulation and to also perform sensitivity analyses on the most essential input parameters of the soil models.

- To make a judgment regarding the performance of the four soil models, in order to give an account for the role of fabric anisotropy and small strain soil behavior in the prediction of deformations in this geotechnical task.

- To perform stability analyses using GEO-SLOPE from Geostudio, on the sides of each section where inclinometers were installed.

- To discuss the plausibility of the results and the credibility of chosen parameters and soil layers, as well as to draw conclusions and present some recommendations regarding future investigations.

1.2 Methodology

The methodology of this MSc thesis has included literary studies of previous master degree projects and technical reports in the field of geotechnics, as well as analyses of geotechnical data retrieved at the site of the project E13. Among authors of the literary compositions which have been addressed over the work process are *Benz, Bonnier, Craig, Karstunen, Muir Wood, Schanz, Sällfors, Vermeer* and *Wheeler*, as

well as the former MSc-students at Norconsult, *Ismail & Teshome* (Chalmers University of Technology) and *Kvick* (Luleå University of Technology).

The material from the geotechnical survey, used in this project, consisted of routine investigations, CRS- and DSS-tests, CPT, fall-cone tests and measurements of soil movement from inclinometers and surface points. The software used for the compilation of data and the projection of inclinometer readings were predominantly Microsoft Excel, In-Site and Grapher. Although most analytical work has been executed using finite element numerical analyses, some simple stress calculations were performed in Microsoft Excel. These were then used as plausibility references against the stresses generated in the finite element software Plaxis 2D. After the finalization of the soil profiles, the geometries of the two excavations were specified based on the models used in the previous MSc- degree projects, by *Ismail & Teshome* (2011) and *Kvick* (2012).

For the specification of stiffness parameters, governing the deformation behavior of the soil, two methods were used. One was based on empirical approaches for evaluating unloading- and reloading moduli, with essential parts taken from well-established Swedish geotechnics, and one in which consolidation theory was used to specify the compression- and swelling behavior of the soil, in terms of stress vs. void ratio, rather than stress vs. strain.

The deformation analyses were performed with Plaxis 2D, with available commercial models Hardening Soil and HS-Small, as well as user-defined versions of modified Cam clay and S-CLAY1, developed by a group of geotechnical researchers, led by Professor Minna Karstunen. Slope-stability analyses were performed using the Morgenstern-Price method in GEO-SLOPE, by Geostudio.

2 PROBLEM BACKGROUND

2.1 The expansion of the Norway-Vänern rail route

The object assessed in this report was part of an extensive infrastructure project, *Bana Väg i Väst*, initiated in 2004 on request from the Swedish Road Administration (2013). The purpose of the incentive was to increase the capacity of the railway between Gothenburg and Trollhättan, by replacing the old railway with a double track solution, and to also enhance the road connection E45 by an expansion from two to four lanes. See figure 2.1 for an overview of the extent of the project, and the concepts applied for the new infrastructure solution.

Figure 2.1. Left: Map showing the alignment of the railway (red) and the new road (yellow) (Trafikverket 2013). Right: Design solution for the expansion of the two transport modes (Sjögren Arkitekter AB).

2.2 Relocation of the road E45 and diversion of traffic

At Lärjeholm, located in the northern part of Gothenburg municipality, the project included a double bridge being constructed for the railway, to allow for a relocated stretch of the road E45 to intersect its alignment (Kvick, 2012). The contracting process for the bridges and the four lane road was accomplished in stages, with measures for traffic diversion adapted throughout the process.

During a major part of the process, a preliminary two lane road passed under the newly built bridges, ensuring the flow of traffic at the site of the construction. This preliminary road intersected the railway slightly north of the crossing for the final relocation of the road E45, and as a consequence, the railway had to pass over two connecting bridge sections, under which the underlying embankment had been excavated. See figure 2.2.

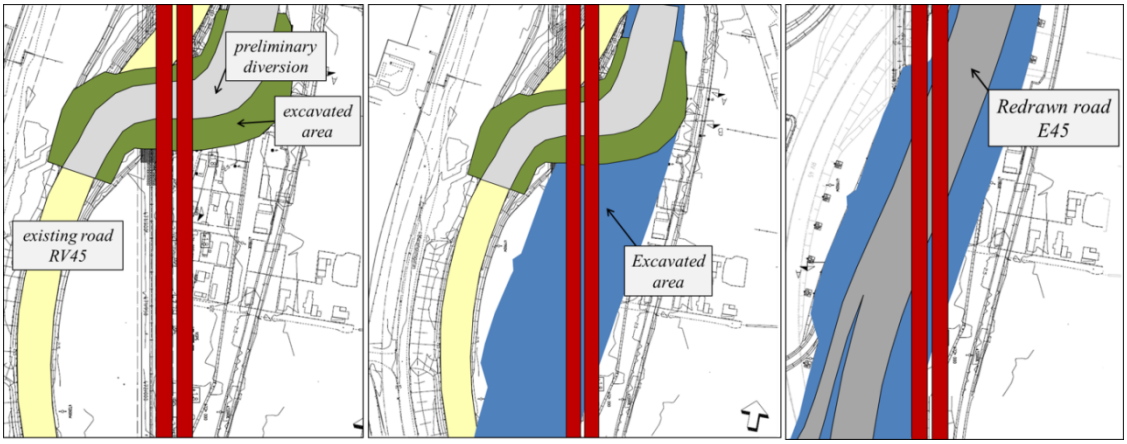

Figure 2.2. The diversion of traffic during the project, as well as the position of the final drawing of the road E45, relative to the double railway bridge.

2.3 Design issue and problem formulation

The excavation for the preliminary road was analyzed by *Ismail and Teshome* (2011), at the section shown in figure 2.3, with the purpose of finding an appropriate soil model and soil stiffness, to be used in the design of the excavation for the new road E45. The simulations, made as part of an MSc-degree project, were done in Plaxis 2D with the soil models Mohr-Coulomb and Hardening Soil, and the deformations predicted in the simulations correlated fairly well with the inclinometer readings, although the deformations at shallow depths were underestimated, while at larger depths, overestimated.

The findings of the assessment, including soil profile, choice of soil model, as well as input parameters, were applied in later simulations on the excavation for the final redrawing, with the analyzed section shown in figure 2.4. The planning for the contracting process, of this more extensive phase of the project, was then based on the predictions generated by these simulations.

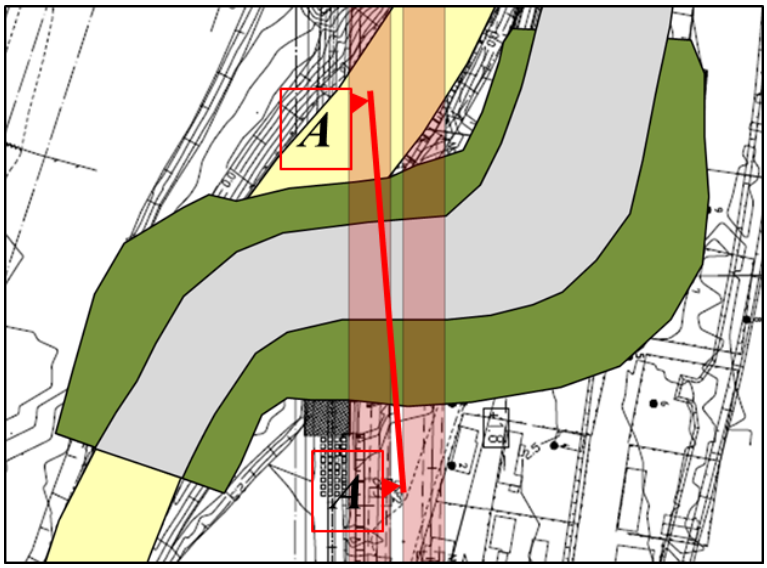

Figure 2.3. The section analyzed in the thesis by Ismail and Teshome (2011), included in the geotechnical pre-investigation, on which the planning for the final redrawing of the road was based.

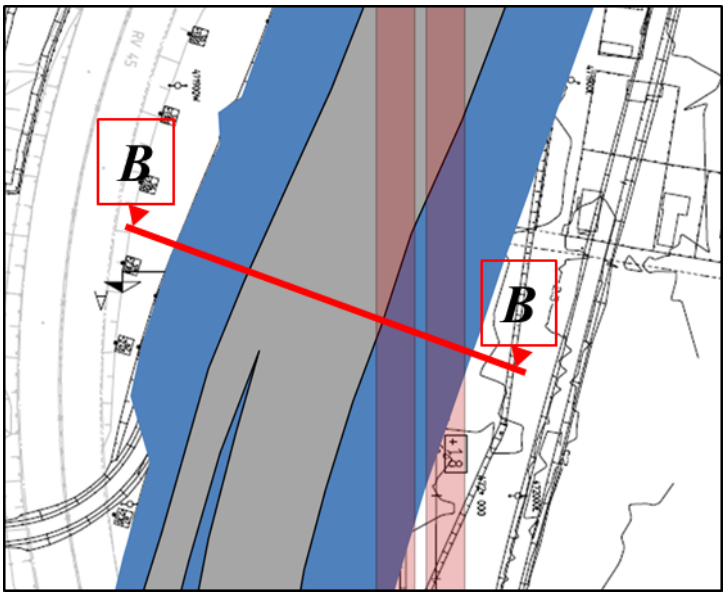

Figure 2.4. The section assessed for the deformation predictions in the excavation conducted for the redrawing of the road E45.

After the contracting of the bridges and the excavation for the new road was accomplished, a few issues did arise. The unloading caused as a result of the excavated sections induced larger than predicted horizontal soil deformations transversal to the slopes, in which the foundations of the bridges had been installed. Due to the bridges' diagonal direction, relative to the relocated stretch of the road E45, rotational movement of the bridge structures was initiated. See figure 2.5.

Figure 2.5. Conceptual figure showing the rotation of the bridge, as a result of the movement in the slopes.

The inconvenience of the matter shed light on issues which may be caused by conservative deformation predictions, and thus motivated a deeper investigation regarding the choices of soil models and soil stiffness parameters, in order to be able to more accurately predict the behavior of soil in problems involving excavation and unloading. *Kvick* (2012) investigated the effect of the bridge foundations on the development on horizontal deformations at the site. There has so far, however, been no further investigation regarding the interpretation of soil behavior at the site, and it was on these premises that the initiative to this MSc thesis was made.

2.4 Location of the site and its geological conditions

The double track railway and the road E45 intersect at a location situated 250 meters east from the shore of Göta River, see figure 2.6. The Gothenburg area, in which Lärjeholm is situated, is located in the southern part of the river valley. The geology in this region is dominated by extensive layers of post-glacial marine clay, deposited posterior to the previous ice age, at a time when the sea level was approximately 125 meters above the current (Arvidsson et al., 2006). There is an occurrence of quick clay in the area, but the general composition is represented by homogeneous soft clay with occasional thin layers of fine friction material.

The routine investigations retrieved from the five bore holes at the site, accounted for later in this report, indicate a similar material setup. From the ground surface and to a depth of approximately 32 meters, the profile is represented by soft clay, with occasional specks of sulphide, as well as traces of shell and organic material. In the soil layers below the most northern part of the excavated site, silty clay dominates below a depth of 20 meters. Below is an extensive layer of frictional material, the upper part of which can be found at a depth of between 32 and approximately 40 meters. Through seismic investigations in the area, the underlying bedrock has been

located at depths ranging from 70 to 80 meters (Kvick, 2012). The ground surface of the two investigated sites is on a level between +2.5 and +3.5 meters, with ground water located at +1.5 meters. Pore pressures have been found to be hydrostatic.

Figure 2.6. The location of the section in which the double track railway intersects the new road, E45 (maps.google, 2013).

3 THEORY - PARAMETERS & SOIL MODELS

3.1 Selection of soil models

The selection of soil models in this thesis was motivated based on a number of arguments. The first regards the Hardening-Soil model. It was suspected that a more detailed evaluation regarding the division of soil layers and a different selection of soil parameters might have resulted in more accurate deformation predictions than those anticipated in previous investigations, considering that the soil profiles analyzed in these reports were created in fairly coarse detail. The use of the second model, HS-Small, was motivated since small-strain stiffness, which was considered likely to impact on the deformation predictions deeper in the soil, is not accounted for in Mohr-Coulomb and Hardening-Soil, the models which were previously utilized. Even though the design issue in this case primarily represents an unloading problem, while S-CLAY1S, being the third model, is best suited for loading of normal consolidated or lightly over-consolidated clays, measurements indicate the occurrence of plastic deformations at certain depths in the soil profile. These deformations motivated the use of a model with the ability to account for the effect of changes in fabric anisotropy, as irreversible deformations develop throughout the soil profile. Yet another reason for choosing this model was that it had not yet been applied on a problem involving unloading of a soil mass, and that it was therefore of interest to investigate its performance in this context. In addition, the critical state model modified Cam clay was included, to be used for comparison with S-CLAY-1, in the assessment regarding the role of anisotropy in the soil.

3.2 Stress invariants and stiffness parameters

This sub-chapter is included with the purpose of introducing some general parameters which are commonly used in the formulation of numerical soil models. In visualizations of the results from triaxial tests, stresses and stress paths are often expressed in terms of mean effective stresses, p', and deviatoric stresses, q. In axi-symmetric compression or extension, where the radial stress is constant over the soil

sample, these invariants can be written as in equations (3.1) and (3.2), while in plane strain, stresses are given by (3.3) and (3.4) (Muir Wood, 1990). Also see figure 3.1.

Axi-symmetric conditions

$$p' = \frac{1}{3}(\sigma_1' + 2\sigma_3') \qquad (\sigma_2' = \sigma_3') \tag{3.1}$$

$$q = \sigma_1 - \sigma_3 = \sigma_1' - \sigma_3' \tag{3.2}$$

Plain strain

$$s' = \frac{1}{2}(\sigma_1' + \sigma_3') \tag{3.3}$$

$$t = \frac{1}{2}(\sigma_1' - \sigma_3') \tag{3.4}$$

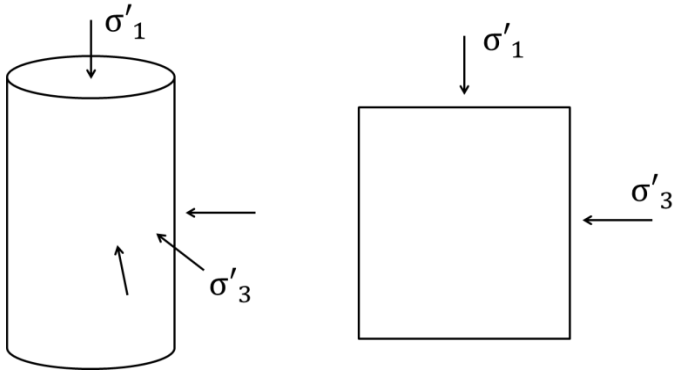

Figure 3.1. Principal effective stresses during Axi-symmetric (left) and plain-strain (right) conditions.

where σ_1' and σ_3' are the major and minor principal effective stresses in a soil element, commonly representing vertical and horizontal stresses in geotechnical applications (Muir Wood, 1990). Following the formulation, the parameter p' can be regarded as a volumetric stress, since positive values would imply mean stresses directed inwards the sample, while negative values indicate the opposite. Note that, in geotechnics, the sign convention is generally reversed, with positive stresses meaning compression (Sällfors, 2009). Analogously, the formulation indicates that q represents shear stresses in the sample.

The strains associated with the above stress invariants are commonly denoted ε_p, for volumetric strain, and ε_q, for deviatoric strain (Muir Wood, 1990). In order to establish a general stress-strain relationship for $p': \varepsilon_p$ and $q: \varepsilon_q$, it is necessary to formulate the elastic response of a soil in terms of purely volumetric stiffness, or bulk modulus, K, and purely distortional stiffness, or shear modulus, G. Most materials have Poisson´s ratios lower than 0.5, which means that, as they are compressed or extended vertically, the lateral deformation is smaller than the vertical. This brings that the volume of the deformed sample changes. The bulk modulus, K, is a way of

expressing the stiffness related to this volumetric deformation, and can be written in terms of Young's modulus and Poisson's ratio, in accordance with equation (3.5).

$$K = \frac{E}{3(1-2\nu)} \tag{3.5}$$

The perhaps more widely recognized shear modulus, G, is given by equation (3.6):

$$G = \frac{E}{2(1+\nu)} \tag{3.6}$$

Yet another parameter central in the descriptions of some soil models is the specific volume, ν, which is the ratio between the total volume of a sample and the volume of its solid particles (Muir Wood, 2009). Rewritten, the specific volume may be expressed according to equation (3.7).

$$v = 1 + e \tag{3.7}$$

Where e is the void ratio, being the ratio of volume of voids, V_V, and the volume of solids, V_S, or the product of the water content, w, and the specific gravity, G_s, of a soil sample, defined by equation (3.8).

$$e = \frac{V_V}{V_S} = wG_s \tag{3.8}$$

The relation between mean effective stress and specific volume during loading is, if plotted on a semi-logarithmic scale, reasonably well represented by straight lines (Muir Wood, 2009). This is displayed in figure 3.2 below, where λ is the inclination of the curve for isotropic normal compression (iso-ncl), and κ is the slope for unloading-reloading (url).

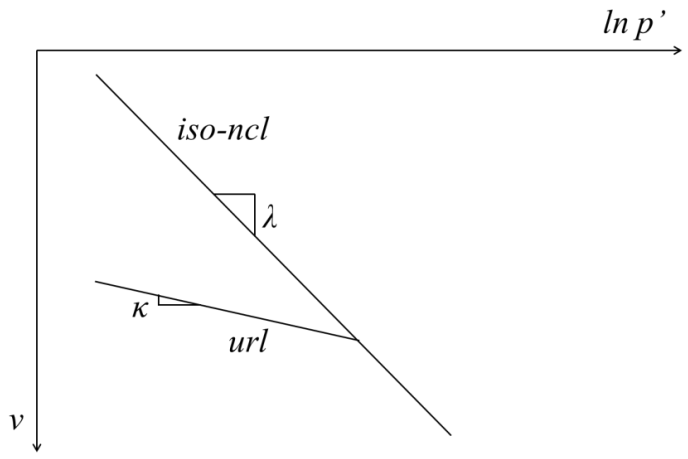

Figure 3.2. Curves for isotropic normal compression and unloading-reloading plotted on a semi-logarithmic scale.

The parameters λ and κ are used for the formulation of some critical state models, in this report represented by modified Cam Clay and S-CLAY1S.

In lack of triaxial test data, the parameters may also be derived from an oedometer or CRS test. This is achieved by calculating the variation of void ratio with changes in volumetric strain, and subsequently plotting $\log \sigma'$ against void ratio, e. For details, see Craig (2004). λ and κ may then be retrieved from equations (3.9) to (3.12), with swelling indices C_c and C_s from figure 3.3 (Plaxis 2012a).

$$\lambda^* = \frac{C_C}{2.3(1+e)} \qquad \kappa^* \approx \frac{2C_S}{2.3(1+e)} \qquad (3.9, 3.10)$$

$$\lambda = \lambda^*(1+e) \qquad \kappa = \kappa^*(1+e) \qquad (3.11, 3.12)$$

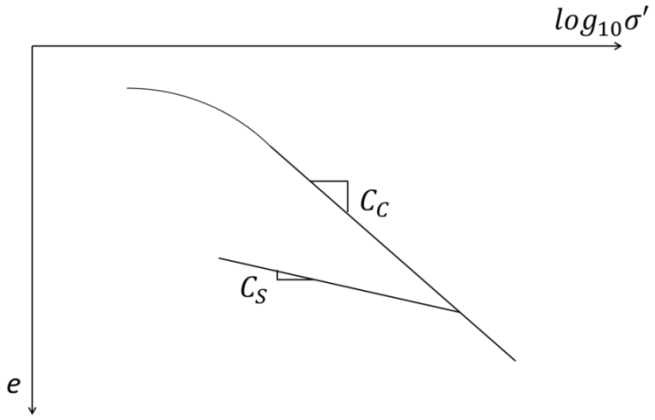

Figure 3.3. Swelling and compression index from an oedometer or CRS test.

3.3 The Hardening Soil model

The Hardening Soil model was developed by *Schanz, Vermeer and Bonnier* (1999) to overcome the inconsistency in interpreting loading and unloading from the earlier Duncan-Chang model developed by *Duncan & Chang* (1970). The model was first accepted among engineers in the geotechnical field due to its simplicity in only needing two stiffness parameters to capture the soil behavior in a reasonably good way (Schanz et al., 1999).

The Hardening Soil model is used to model the nonlinear behavior of soils, which is why it uses a hyperbola, instead of a linear elastic – perfect plastic relationship between stresses and strains, to describe the soil stiffness. See figure 3.4 for a comparison between the approaches.

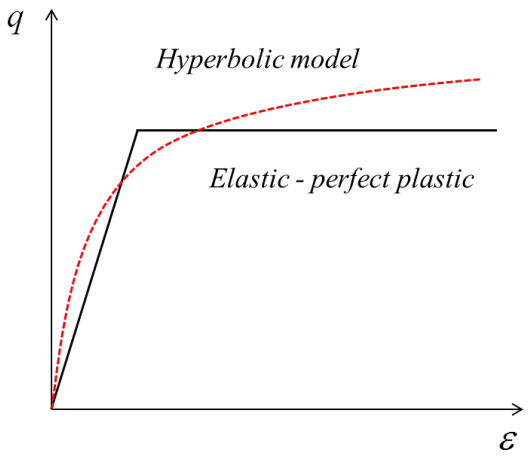

Figure 3.4. The difference between the hyperbolic Hardening Soil model and Mohr-Coulomb.

Hardening Soil is a double hardening soil model, governed by two hardening rules, controlling the size and shape of the yield envelope in the $p' : q$ plane. This is one of the features separating it from the simpler Mohr-Coulomb model, which has a linear elastic response below the fixed failure surface, see figure 3.5. The hardening soil model assumes isotropic elasticity in the region below the deviatoric yield surface and to left of the yield cap (Karstunen HS lecture, 2012). In primary shearing, the model utilizes decreasing stiffness the more the soil is subjected to deviatoric stress, and as the stiffness of the soil decreases, irretrievable plastic strains build up (Schanz et al., 1999).

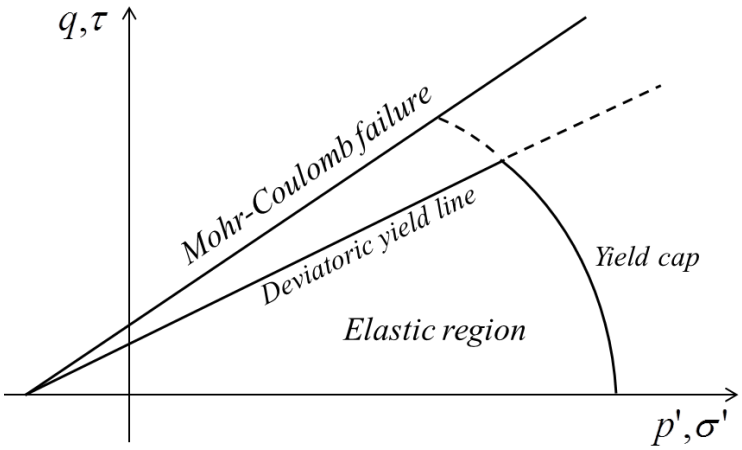

Figure 3.5. The Hardening Soil yield envelope together with the Mohr-Coulomb failure line.

The deviatoric yield function of the hardening soil model in the $p' : q$ plane can be described according to equation (3.13) (Schanz et al., 1999).

$$f_s = \frac{q_a}{E_{50}} \frac{q}{q_a - q} - \frac{2q}{E_{ur}} - \gamma^{ps} \qquad (3.13)$$

In this formulation, γ^{ps} is a hardening parameter which represents the accumulated plastic shear strain, defined by equation (3.14) (Schanz et al, 1999). q_a is the asymptotic value of the shear strength, shown in figure 3.6.

$$\gamma^{ps} = 2\varepsilon_1^p - \varepsilon_v^p \approx 2\varepsilon_1^p \tag{3.14}$$

The function of the yield cap surface is defined as in equation (3.15):

$$f_c = \frac{q^2}{M^2} + (p' + a)^2 - p_c + a^2 \tag{3.15}$$

where p' is the mean effective stress which the sample is subjected to. M is a model parameter related to K_0^{NC}.

In the Hardening Soil model, deformations are governed by three stress dependent stiffness parameters, namely the triaxial loading secant stiffness modulus, E_{50}, the unloading-reloading stiffness, E_{ur}, and the oedometric stiffness, E_{oed}. The principle for how the former two are defined can be seen in figure 3.6 (Obrzud, Numerics in geotechnics, 2010).

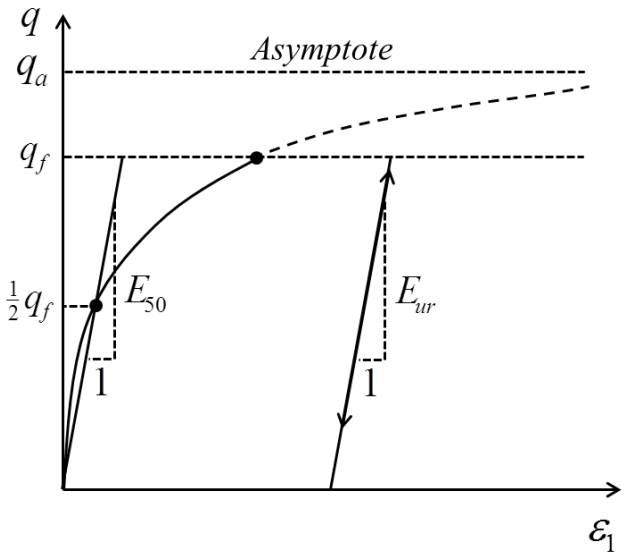

Figure 3.6. Unloading-reloading modulus, E_{ur}, and secant modulus, E_{50}, defined at 50 % of the shear strength.

The three stiffness moduli are formulated as in equations (3.16) to (3.18) (Schanz et al 1999).

$$E_{50} = E_{50}^{ref}\left(\frac{\sigma'_3 + c'\cot\varphi'}{\sigma^{ref} + c'\cot\varphi'}\right)^m \tag{3.16}$$

$$E_{ur} = E_{ur}^{ref}\left(\frac{\sigma'_3 + c'\cot\varphi'}{\sigma^{ref} + c'\cot\varphi'}\right)^m \tag{3.17}$$

$$E_{oed} = E_{oed}^{ref} \left(\frac{\sigma'_1 + c' \cot \varphi'}{\sigma^{ref} + c' \cot \varphi'} \right)^{m} \quad (3.18)$$

In a simulation, the instantaneous stiffness is determined based on how the stress state in the soil relate to the reference pressure, σ^{ref}, for which the reference moduli are specified. The exponent m affects the stress dependency of this relation, and also the curvature of the deviatoric yield line. If $m = 1$, the line is straight. If $m < 1$, the line is curved (Schanz et al., 1999).

The volumetric hardening, represented by an expansion of the yield cap, is determined by the first hardening law, shown in equation (3.19), also called compression hardening or cap hardening (Schanz et al., 1999). The increment dp_p is the increase in size of the yield cap, while H is a stress dependent hardening modulus and $d\lambda^c$ is a plastic multiplier determining the magnitude of the stress increment. The principle can be seen in figure 3.7, where the old cap expands and pushes to the right (Karstunen, HS lecture, 2012). For the cap, an associated flow rule is assumed, which means that the direction of the plastic strain increment is orthogonal to the cap. The volumetric hardening is used to model irretrievable plastic strains due to mainly isotropic compression (Schanz et al., 1999).

$$dp_p = d\lambda^c h_{p_p} \; h_{p_p} = 2H \left(\frac{\sigma'_3 + c \cot \varphi'}{p^{ref} + c \cot \varphi'} \right)^{m} \quad (3.19)$$

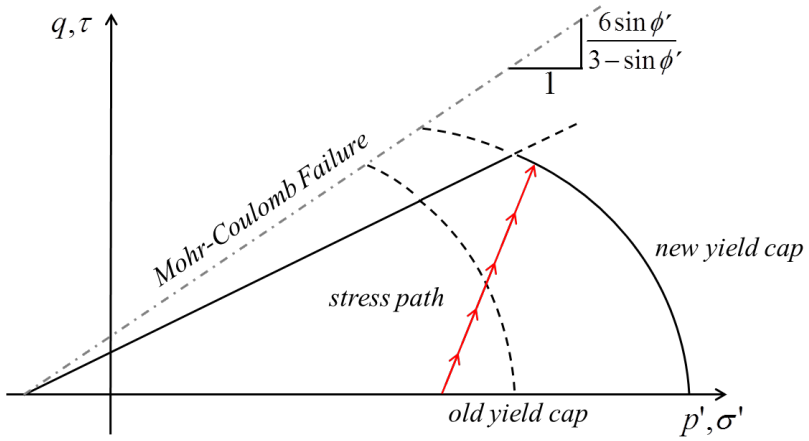

Figure 3.7. Showing how a new yield cap is introduced when the soil is subjected to the red stress path, as it passes the border of the yield envelope on the compressive side.

The deviatoric hardening is determined by the second hardening rule, described by equation (3.20) below, also called shear hardening or frictional hardening. The formulation implies that the gradient of the yield criterion increases when the soil is subjected to stresses representing points located on the deviatoric yield line. See the example in figure 3.8. For these yield lines, a non-associated flow rule is assumed, meaning that the plastic strain increment has a direction which is non-orthogonal to the yield criterion, and is instead governed by the mobilized dilatancy angle (Karstunen, 2012). The shear hardening rule is used to model irretrievable strains due to loading that is characterized by shearing (Schanz et al., 1999).

$$d\gamma^{ps} = d\lambda^{s} h_{\gamma^{ps}} \tag{3.20}$$

where

$$h_{\gamma^{ps}} = \left(\frac{\partial g}{\partial \sigma_1} - \frac{\partial g}{\partial \sigma_2} - \frac{\partial g}{\partial \sigma_3}\right) = 1 \tag{3.21}$$

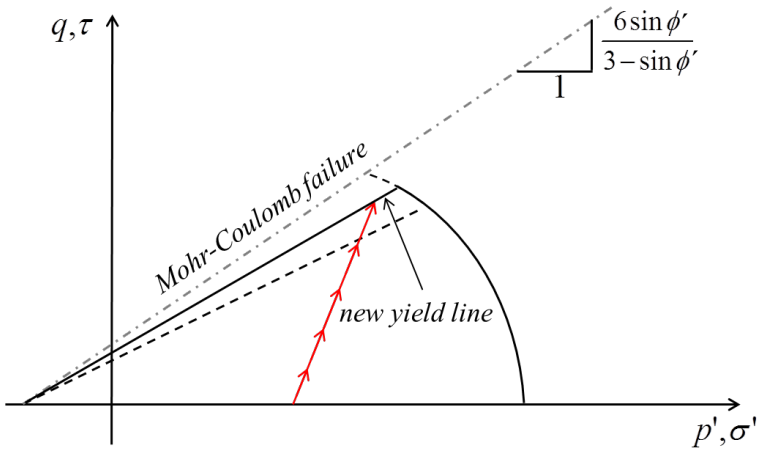

Figure 3.8. Showing how the gradient of the initial deviatoric yield line is increased as the red stress path reaches the border of the elastic region, on the deviatoric side.

The two hardening laws may also be utilized simultaneously. This is called combined hardening. An example of this is shown in figure 3.9.

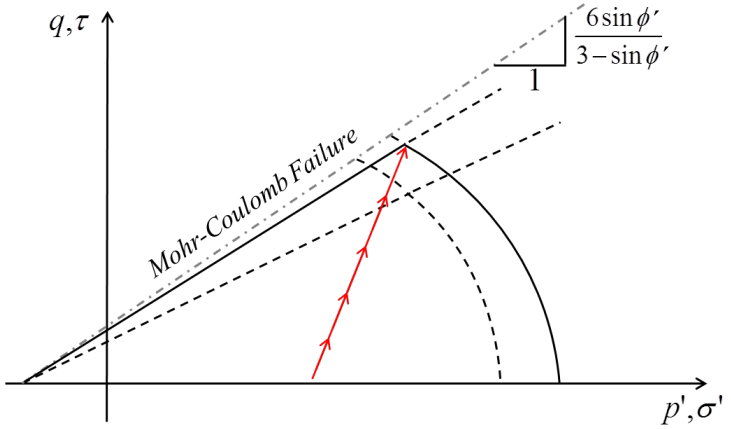

Figure 3.9. Showing how combined hardening can occur if the red stress path starting from inside the elastic region passes both the deviatoric yield line and the yield cap.

3.4 HS-Small

HS-Small is an extension of Hardening Soil, and was developed to account for the stiff deformation behavior, which has been observed in soil subjected to very small strains. The model introduced some features which were new to Hardening Soil, such as an implementation of the Small-strain Overlay model as well as some modifications to the existing failure criteria and flow rules (Benz, 2007).

In the Small-strain Overlay model, the isotropic stiffness is dependent on the magnitude and history of strain (Benz, PhD-thesis, 2007). It has long been known that for very small strains, the soil has a much stiffer response to loading, than what is accounted for in for example the Hardening Soil model. The Small-Strain Overlay model, which has been implemented in HS Small, represents this small strain stiffness by utilizing the modified Hardin-Drnevich relationship, in which the shear modulus of the soil is related to the magnitude of strain. See figure 3.10 and equation (3.22).

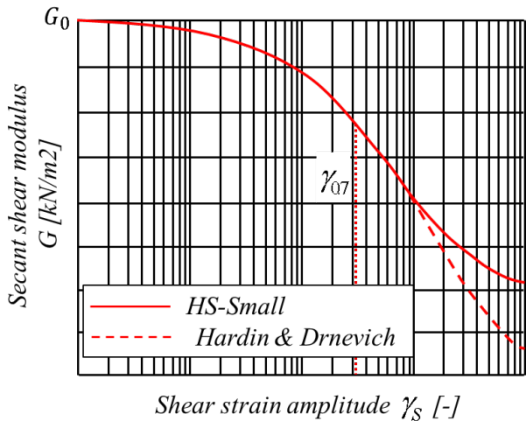

Figure 3.10. Reduction curve for the secant shear modulus, depending on strain amplitude.

$$G = \frac{G_0}{1+0.385\frac{\gamma}{\gamma_{0.7}}} \tag{3.22}$$

During the initiation of loading, the model reduces the plastic strains to preserve the soil stiffness during small strains. By setting the Poisson's ratio to be constant in the HS-Small model, Young´s modulus and the bulk modulus during small strains can be calculated as in equations (3.23) and (3.24).

$$K' = G\frac{2(1+\nu\prime)}{3(1-2\nu\prime)} \tag{3.23}$$

$$E' = 2(1+\nu')G \tag{3.24}$$

In the HS-Small model, the two parameters controlling the stress- and strain-history dependent soil stiffness are the small-strain-, or dynamic, shear modulus, G_0, and the threshold shear strain, $\gamma_{0.7}$, which is the strain amplitude at which the modified Hardin-Drnevich relationship has reduced the secant shear modulus to 70 percent of its initial value (Benz, 2007). The instantaneous value on G_0 is, similarly to the three

moduli in Hardening Soil, dependent on the stress state in the soil, and is specified for a certain reference pressure, as in equation (3.25).

$$G_0 = G_0^{ref}\left(\frac{\sigma_{\prime 3}+c\prime\cot\varphi\prime}{p^{ref}+c\prime\cot\varphi\prime}\right)^m \quad (3.25)$$

For large strain sequences in the hyperbolic reduction curve of the small strain stiffness, a cutoff is introduced at the shear strain γ_c. At this level of strain, the model switches from the tangent modulus defined by the modified Hardin-Drnevich relationship, to the unloading-reloading shear modulus, G_{ur}, which is defined according to equation (3.26) (Benz, 2007). See figure 3.11.

$$G_{ur} = \frac{E_{ur}}{2(1+\upsilon_{ur})} \quad (3.26)$$

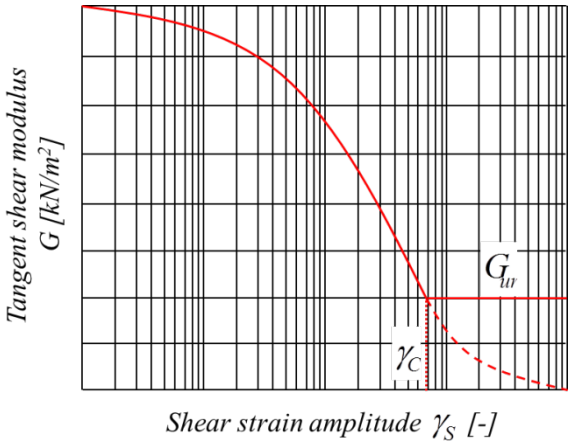

Figure 3.11. Representation of how the tangent shear modulus is reduced to the unloading-reloading modulus during large strain sequences.

Figure 3.12 contains an example of how the small strain stiffness is utilized in cyclic unloading and reloading. The example shows that HS Small employs a higher stiffness, E_0, in the initial phases of the unloading-/reloading sequences UR1 and UR2, than does Hardening Soil, which uses E_{ur} throughout the whole unloading and reloading cycles. Thus, the HS Small model has means for taking hysteresis into account, being the lag between the unloading and reloading curves in UR2. The figure also shows that the use of a soil model unable to account for this effect may result in an over-estimation of strains in an unloading problem (Benz, 2007).

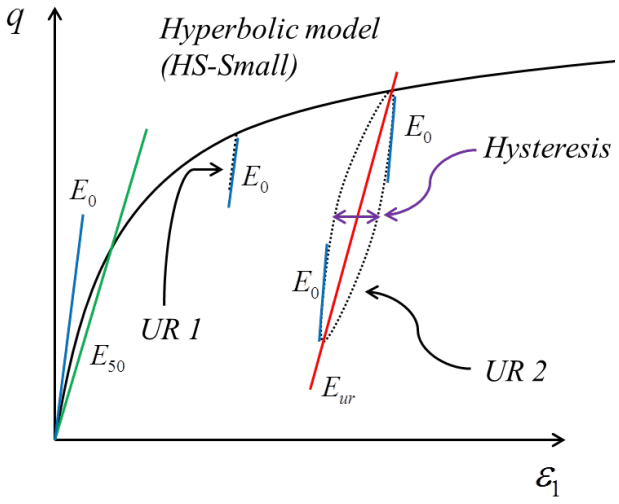

Figure 3.12. The initial high HS-Small modulus E_0 during the initiation of each loading and unloading, where it can be seen that hysteresis is introduced during larger unloading-reloading cycles.

In addition to the Mohr-Coulomb failure and yield criterion, the Matsuoka-Nakai failure, along with Drucker-Prager based deviatoric plastic flow, was introduced to the HS-Small model. This additional feature is optional and can be turned on or off depending on preference (Benz, 2007). This feature has not been used in this report.

The hardening laws of the HS-Small model, which can be seen in equations (3.27) and (3.28), are similar to those of Hardening Soil. Added is an approximation of plastic hardening during initial loading, h_i (Benz, 2007).

$$d\gamma^{ps} = d\lambda^{s} h_i h_{\gamma^{ps}} \tag{3.27}$$

$$dp_p = d\lambda^{c} h_i h_{p_p} \tag{3.28}$$

3.5 S-CLAY1S

In this chapter, the main features of the anisotropic soil model S-CLAY1S is described. S-CLAY1S is founded on the critical state soil model modified Cam clay, originally published by Roscoe and Burland in 1968. Modified Cam clay, in turn, descends from development of the original Cam clay model, formulated by Roscoe and Schofield in 1963 (Muir Wood, 1990). In the following sub-chapter the basic features of modified Cam clay are described, after which an account is given for how anisotropy and bonding have been represented in the formulation of S-CLAY1S.

3.5.1 Modified Cam clay

The main feature of modified Cam clay is the formulation of a yield criterion, dependent on the stress invariants mean effective stress, p', and deviatoric stress, q, for when a soil mass subjected to triaxial compression or extension can be expected to turn from elastic behavior to plastic hardening, or eventually reach shear failure (Muir Wood, 1990). Data collected from triaxial tests indicate a rather different shape of the true yield criterion for natural soils. However, for reasons such as computation simplicity, a symmetric shape was chosen for the model formulation. The criterion is expressed through the formulation of a yield function, see equation (3.29), and can be visualized as an ellipse, or yield locus, symmetric around the mean effective stress axis and with a fixed shape but with size changing with the stresses the soil is experiencing, see figure 3.13 (Muir Wood, 1990).

$$f = q^2 - M^2[p'(p'_0 - p')] = 0 \tag{3.29}$$

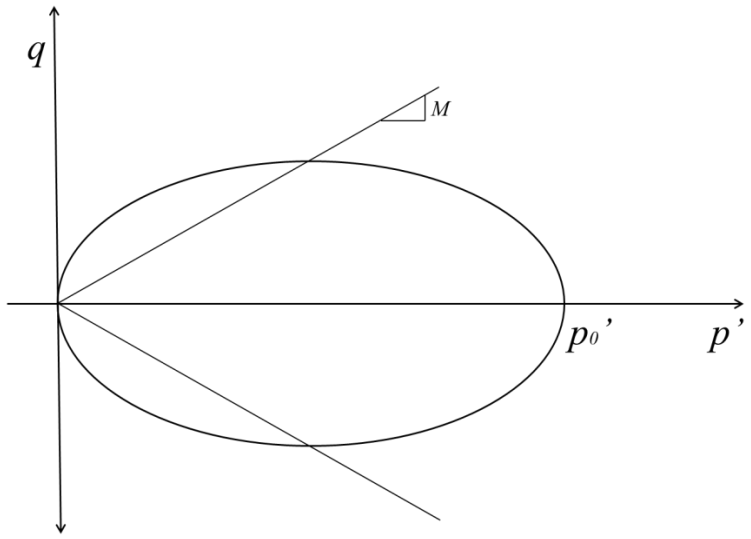

Figure 3.13. Yield locus in modified Cam clay.

The area enclosed within the ellipse represents stress states associated with elastic response in the soil, while stresses located on the border of the envelope results in plastic deformations, with subsequent expansion or contraction of the yield locus. As the locus expands, the soil undergoes hardening, while contraction of the locus results in the opposite. Elastic volumetric strains, $\delta\varepsilon_p^e$, are dependent on the soil´s unloading-reloading stiffness and changes in mean effective stress, p', while elastic shear strains,

$\delta\varepsilon_q^e$, are determined by increments in deviatoric stress, q, as well as the soil´s shear modulus, G′. The expressions for these two elastic strain increments are described in equations 3.30 and 3.31, in which the parameters λ and κ can be recognized from figure 3.2 in chapter 3.2 (Muir Wood, 1990).

$$\delta\varepsilon_p^e = \frac{\delta p'}{K'} = \kappa\frac{\delta p'}{v p'} \tag{3.30}$$

$$\delta\varepsilon_q^e = \frac{\delta q}{3G'} \tag{3.31}$$

Following the v: ln p′ relationship, it can be shown that the plastic volumetric strains in modified Cam clay are governed by equation (3.32). The plastic shear strains can, through observation of stress ratios in drained triaxial shear tests combined with the stress-strain relation for elasto-plastic hardening and the definition of the modified Cam clay yield locus, be expressed according to equation (3.33).

$$\delta\varepsilon_p^p = \left[\frac{(\lambda-\kappa)}{v}\right]\frac{\delta p_0'}{p_0'} \tag{3.32}$$

$$\delta\varepsilon_q^p = (\lambda-\kappa)\frac{2\eta(M^2-\eta^2)+12\eta^2}{3vp'(M^2+\eta^2)(M^2-\eta^2)}\delta q \tag{3.33}$$

Where M is the inclination of the critical state line, see figure 3.13, and the parameter η is the stress ratio $\left(\eta = \frac{q}{p'}\right)$.

The dimensions of the ellipse is determined by the size parameter p_0', which is the isotropic mean effective pre-consolidation stress, and thus the magnitude of the expansion is governed by the incremental value $\delta p_0'$, see figure 3.14. The size of the increment $\delta p_0'$ is retrieved from a hardening law, displayed in equation (3.34), in which the change in size of the yield locus is related to increments of plastic volumetric strain (Muir Wood, 1990).

$$\frac{\delta p_0'}{\delta\varepsilon_p^p} = \frac{v p_0'}{(\lambda-\kappa)} \tag{3.34}$$

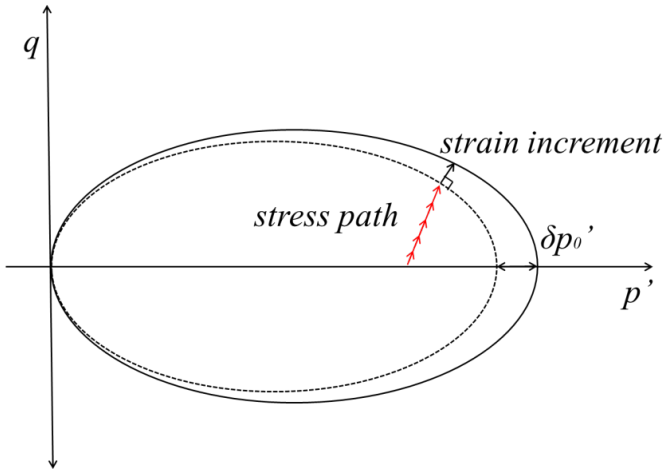

Figure 3.14. Yield locus expanding due to plastic deformations.

The direction of plastic strains, resulting from stresses located on the yield envelope, is governed by a flow rule. In the case of modified Cam clay, an assumption of associated, or normalized, flow is incorporated in the model, meaning that the strain increment has a direction normal to the yield locus (Muir Wood, 1990). The flow rule is not truly determined by the tangent of the yield locus, but rather by a function called plastic potential. However, an assumption of associated flow brings that the plastic potential, denoted g, is equal to the yield function $[f(p', q, p_0') = g(p', q, \xi)]$. An example of a strain increment following the associated flow rule can be seen in figure 3.15, which displays the strain direction at failure, while the mathematical expression for the direction of strain is shown in equation (3.35). Note that this relation is valid only if associated flow is assumed.

$$\frac{\delta\varepsilon_p^p}{\delta\varepsilon_q^p} = \frac{\frac{\partial g}{\partial p'}}{\frac{\partial g}{\partial q}} = \frac{\frac{\partial f}{\partial p'}}{\frac{\partial f}{\partial q}} \tag{3.35}$$

States of failure are interconnected with the critical state lines, starting from the origin and with inclinations denoted M. These lines can be regarded as visualizations of all stress states located at the crest (for triaxial compression), or the trough (triaxial extension), of every achievable yield locus, the principle of which can be seen in figure 3.15. Such states are, due to the choice of flow rule, associated with purely deviatoric strains, meaning that plastic shear strains will develop indefinitely, without any further increment in mean effective stress, leading to failure of the soil. The inclination, M, is defined according to equations (3.36) to (3.38). A soil mass modeled in modified Cam clay will, at shear failure, satisfy the conditions in (3.39) (Muir Wood, 1990).

$$M_{compression} = \frac{6\sin\varphi'}{3-\sin\varphi'} \tag{3.36}$$

$$M_{extension} = \frac{6\sin\varphi'}{3+\sin\varphi'} \tag{3.37}$$

$$M_{plane-strain} = \sqrt{3}\sin\varphi' \tag{3.38}$$

$$\left\{\begin{matrix} M = \eta \\ p' = \frac{p_0'}{2} \end{matrix}\right\} \tag{3.39}$$

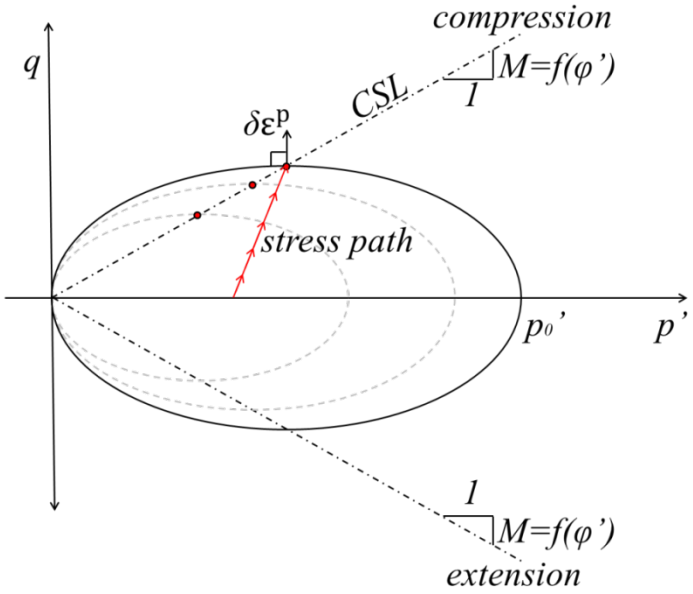

Figure 3.15. The critical state line in compression and extension along with the direction of plastic strain at failure.

For a more thorough deduction of the modified Cam clay model, see Muir Wood (1990). In the following sub-chapters the progression into S-CLAY1S will be accounted for, with focus put on the components of the formulation which represents the interpretation of soil anisotropy and degradation of bonding.

3.5.2 Principles of the model S-CLAY1S

In the formulation of S-CLAY1S, a set of tools have been employed in addition to the principles of hardening plasticity and critical state failure from modified Cam clay. The model has incorporated means for taking into account the anisotropic plastic behavior in natural soft clays, documented through observations of stress paths from triaxial tests, as well as the effect of degradation of bonds in the soil structure. The rotational hardening law in the current version of the model was developed by Näätänen et al. in 1999, based on work by Wheeler (1997). This initial anisotropic model was called S-CLAY1. The law describing the degradation of bonds between soil particles were added in 2002 by Koskinen et al., thus forming the latest revision of the model, called S-CLAY1S (Wheeler et al., 2003; Karstunen et al., 2005).

The model represents anisotropy through an inclination of the yield locus, governed by a rotation parameter, used for describing the changes in anisotropy which may occur due to plastic volumetric or deviatoric strains in a soil specimen. The law describing the degradation of bonds and the effect of destructuration includes the formulation of two yield loci; one describing the yield criterion for the in-situ sample of the soil, accounting for bonds between particles, and one representing the intrinsic yield locus, describing the theoretical properties of the soil, in absence of bonds. One measurement of the effect of bonding in a particular soil is therefore the difference between these two loci. Both these new features, the rotating yield loci and the intrinsic yield surface, may be switched off. Deactivation of both functions leaves a model identical to modified Cam clay (Karstunen et al., 2005).

S-CLAY1, and thus consequently S-CLAY1S, is intended to be used in simulations on soft normal consolidated or lightly over-consolidated clays, in which the plastic strains are expected to be considerably greater than the elastic. For this reason, and for the sake of avoiding unnecessarily cumbersome calculation processes, an isotropic stiffness has been assumed to be a sufficient and reasonable compromise for the elastic response in the model. Therefore, elastic strains are defined by the same expressions, being equations (3.30) and (3.31) above, in S-CLAY1S as in modified Cam clay (Karstunen et al., 2005).

3.5.3 Model formulation

In S-CLAY1S, the principle for the yield loci can be seen in figure 3.16, where the intrinsic yield surface has the same shape as the one for the natural clay, with the difference in size representing the strength contribution by bonds between soil particles. The inclination of the two ellipses represents the anisotropy in the soil. The expression for the yield surface can be seen in equation (3.40) (Karstunen et al., 2004).

$$f = (q - \alpha p')^2 - (M^2 - \alpha^2)([1 + x]p'_{mi} - p')p' = 0 \qquad (3.40)$$

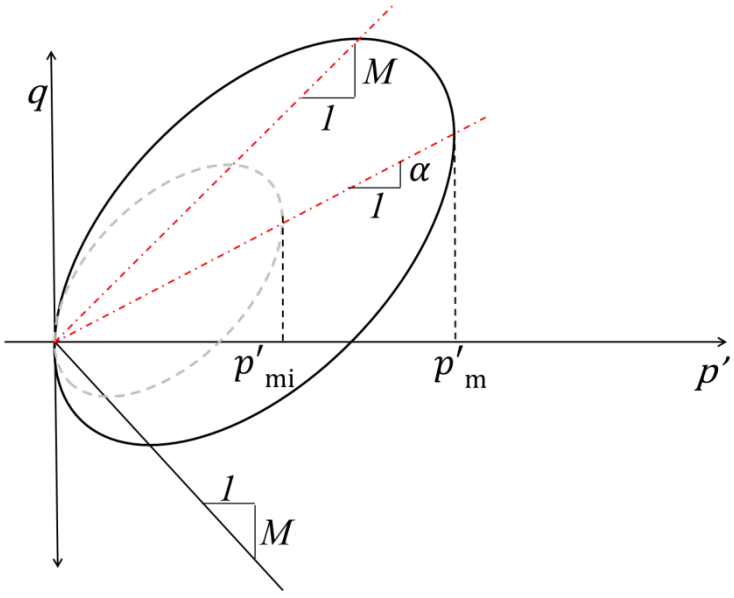

Figure 3.16. Visualisation of yield loci in the triaxial stress plane.

The model incorporates three hardening laws, representing expansion or contraction of the yield surfaces, creation or erasure of anisotropy as well as degradation of bonds. The relation between the real and intrinsic yield surface is given by equation (3.41), where the parameter x represents the amount of bonding (Karstunen et al., 2004).

$$p'_m = (1 + x)p'_{mi} \qquad (3.41)$$

The size, p'_{mi}, of the intrinsic yield surface is, as in modified Cam clay, dependent on changes in plastic volumetric strain. Changes in size of the intrinsic yield surface

represent the hardening or softening that a reconstituted sample of the soil specimen, which in this case would be a disturbed soil sample consolidated to in-situ conditions, would undergo due to for example compression or extension, exceeding the value of p'_m. See equation (3.42) (Karstunen et al., 2005).

$$dp'_{mi} = \frac{vp'_{mi}}{\lambda_i - \kappa} d\varepsilon_p^p \tag{3.42}$$

The second hardening law regards the anisotropy in the soil, and is represented by the parameter α in the yield function. This law, showing the relation between rotational increment and strain, can be seen in equation (2.43) (Karstunen et al., 2004).

$$d\alpha = \mu \left(\left[\frac{3\eta}{4} - \alpha \right] \langle d\varepsilon_p^p \rangle + \beta \left[\frac{\eta}{3} - \alpha \right] d\varepsilon_q^p \right) \tag{3.43}$$

The parameters μ and β relate to the rotation of the yield surface, determining the degree to which volumetric and deviatoric plastic strains, respectively, contribute to the rotation of the yield loci (Karstunen et al., 2004).

The third hardening law describes the changes in the amount of bonding, with governing parameter x, which can be identified in (3.41) (Karstunen et al., 2004). See equation (3.44).

$$dx = -ax\left(d\varepsilon_p^p + b\left| d\varepsilon_q^p \right| \right) \tag{3.44}$$

In this equation, the parameters a and b has a similar function as μ and β in (3.43), since they govern the effectiveness of volumetric and deviatoric strains respectively, in erasing the effect of bonding in the soil (Karstunen et al., 2004).

S-CLAY1S incorporates an assumption of associated flow, leading to the expressions for plastic strain increments given by equations (3.45) and (3.46). Note that in this context, λ is not a stiffness parameter, but a plastic multiplier determining the magnitude of the plastic deformation.

$$\delta\varepsilon_p^p = d\lambda \frac{\partial g}{\partial p'} = d\lambda \frac{\partial f}{\partial p'} \tag{3.45}$$

$$\delta\varepsilon_q^p = d\lambda \frac{\partial g}{\partial q} = d\lambda \frac{\partial f}{\partial q} \tag{3.46}$$

The option of deactivating the functions for anisotropy and bonding is achieved by the following measures (Karstunen et al., 2005). In order to exclude the effect of bonding from the analysis, the parameter x is set to zero, while the intrinsic value, λ_i, is replaced by the true value of λ, which can be retrieved from an oedometer test performed on a natural clay sample. This action would reduce S-CLAY1S into S-CLAY1. The effect of anisotropy is switched off by setting α and μ to zero, which results in a reversion from S-CLAY1 to modified Cam clay.

In this report, the effect of bonding has been deactivated, since there were no data available regarding the bonding effects in the soil at the site of the investigation. Consequently, the anisotropic model used in the simulations of this project is S-CLAY1.

4 DATA EVALUATION

4.1 Specifying input parameters

In this chapter, a description is given regarding the methods used for finding parameters needed to model the two sections. Data was gathered from a total of 39 piston samples, from different levels at five different locations at the site, on which CRS tests and routine investigations, as well as some direct shear tests, had been performed in laboratory. In addition, data from cone penetration tests were available from field investigations. For Excavation 1 – section A, boreholes FB41, 71003 and 71007 were used to collect data, while for Excavation 2 – section B, 71007, 71008 and 72001 were the most relevant. See figure 4.1. Input values for the soil models were specified by plotting each parameter against level for each set of boreholes, after which the parameters were evaluated using adapted trend lines. See *Appendices* for tables containing the input parameters used for each soil model.

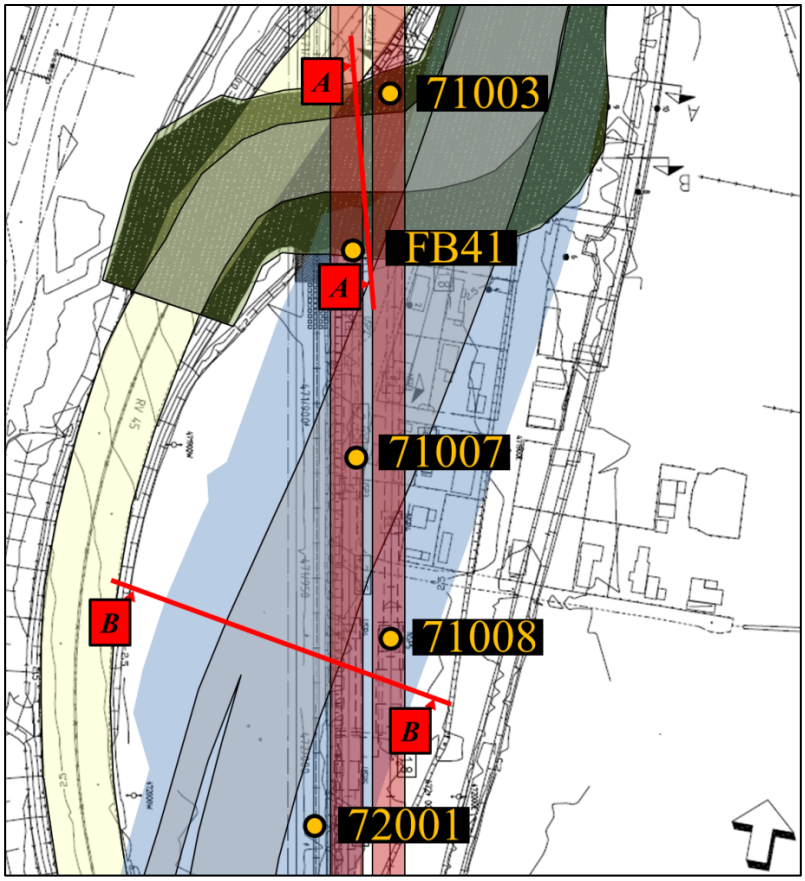

Figure 4.1. Road sections A and B as well as the five bore holes used for the investigation.

Except for the stiffness parameter evaluation method used in *Ismail and Teshome* (2011) an additional one, for which parts have been taken from the Plaxis materials manual, was tested, with the desire of achieving results which better describe the real incurred deformations. The new procedure is in this report referred to as *method 1*, while the one used in *Ismail and Teshome* (2011) will be called *method 2*, both of which will be described in this chapter. The application of the two methods is somewhat different depending on the soil model used, but the governing parameters in each method are the same for all four models. From here on, the appellations *Method 1* and *Method 2* will always be used for separating the two different sets of stiffness parameters procured through the application of the two different procedures. Note that all other input parameters, such as for example friction angle, density, permeability etc., are the same regardless of method.

4.2 General soil parameters

In this section, a brief description is given of how the general input parameters, shared between all combinations of soil models and stiffness evaluation methods, were specified for the modeling of the two investigated excavations.

Permeability - k_x and k_y

The vertical permeability, k_y, measured in meters per day, was exported from the CRS tests by choosing the value corresponding to pre-consolidation pressure. There were no measurements on horizontal permeability, k_x. This value was therefore approximated, and it was decided that $1.5k_y$ was a reasonable assumption, since the clay in the area, even though homogeneous, has a history of non-isotropic loading. Below, in figure 4.2, is an example of how vertical permeability, from bore holes 71007, 71008 and 72001, was plotted against level together with an adapted trend line, for the selection of input data going into the modeled materials.

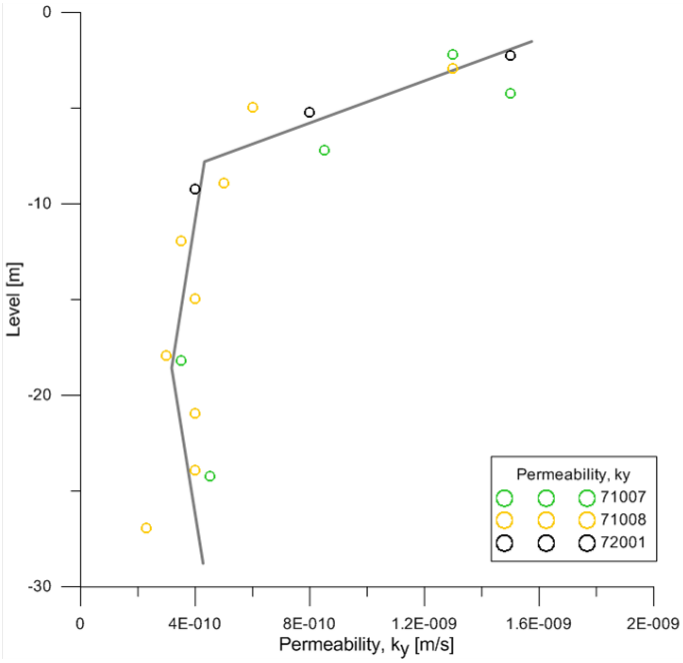

Figure 4.2. Diagram with vertical permeability of the clay layers at Excavation 2 – section B, plotted against level.

Unit weight - γ

The unit weight was taken from the routine investigations, as the mean density for each level of depth. The information was then plotted, following the same principle as in figure 4.2, and then evaluated at the levels corresponding to the center of each soil layer in the modeled soil profiles.

Over-consolidation ratio – OCR

The OCR of each soil layer was evaluated using an approximation on in-situ effective stresses, calculated based on soil density and ground water level, as well as pre-consolidation pressures extracted from the CRS tests. See figure (4.3).

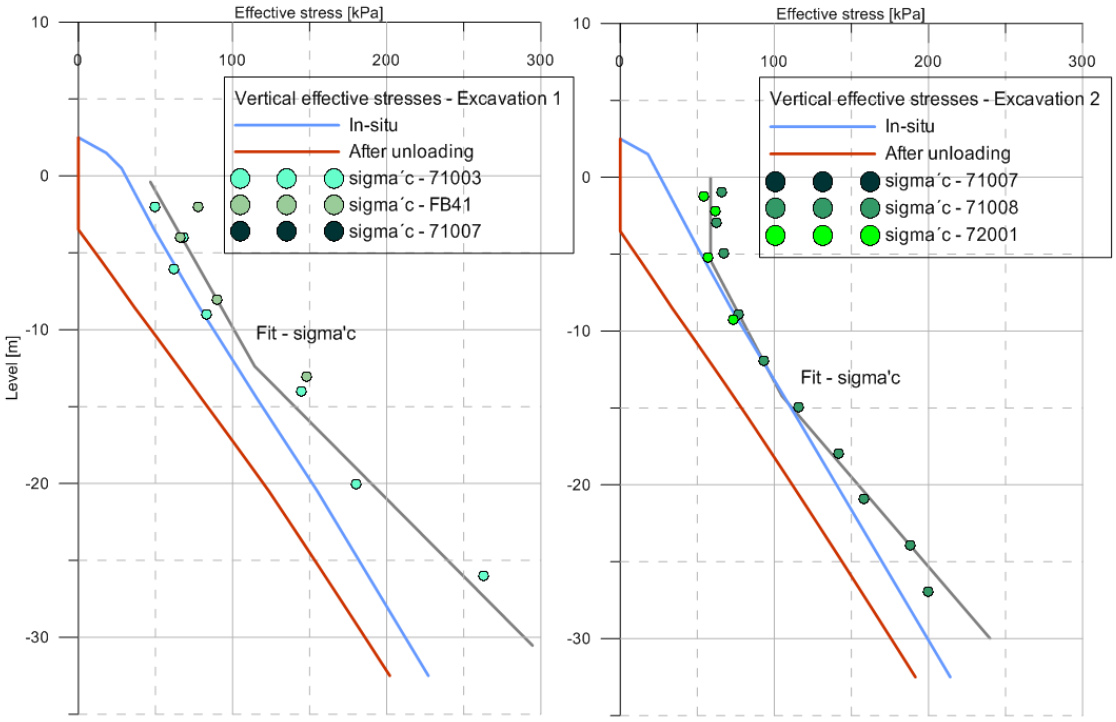

Figure 4.3. Calculated in-situ effective stresses and evaluated pre-consolidation pressures, plotted against level in the soil profile.

Initial void ratio – e_0

The initial void ratio was calculated using equation 4.1, described in *Muir Wood* (1990), for which the water content, w, was evaluated from routine investigations, while the specific gravity, G_S, was set to 2.71, on recommendation by Karstunen (2013).

$$e_0 = w_0 G_s \qquad (4.1)$$

Poisson's ratio – ν

Poisson's ratio, ν, was assumed to be 0.15 in the clay layers, while set to 0.20 in the sand and the frictional material. The former chosen on recommendation by Karstunen (2013), and the latter taken from the investigation by *Ismail and Teshome* (2011).

Friction angle - ϕ'
The friction angle of the clay was assumed to be 30˚, on recommendation by Karstunen (2013), while for the sand and the friction material, the parameter was set to 36˚ and 38˚ respectively (Ismail & Teshome, 2011).

Dilatancy angle - Ψ
This parameter was calculated using the formula in equation (4.2).

$$\Psi = \phi' - 30 \tag{4.2}$$

Earth pressure coefficients - K_0^{nc} and K_{0x}
The earth pressure coefficient for normal consolidated soil, K_0^{nc}, was calculated using Jaky's formula, given by equation (4.3).

$$K_0^{nc} = 1 - \sin\phi' \tag{4.3}$$

For over-consolidated clay, equation (4.4) was used to determine the coefficient, $K_{0,x}$.

$$K_{0,x} = K_0^{nc}\sqrt{OCR} \tag{4.4}$$

Reference pressure - p_{ref}
The reference pressures were evaluated using the initial phase in Plaxis 2D, as the initial horizontal stress in the middle of each soil layer, as to ensure that the reference moduli are defined for the center of each layer. See table 4.1.

Excavation 1 - section A		Excavation 2 - section B	
Soil layer	Pref	Soil layer	Pref
Sand	7	Sand	7
Clay 1	26	Clay 1	25
Clay 2	40	Clay 2	34
Clay 3	56	Clay 3	49
Clay 4	80	Clay 4	91
Clay 5	116		
Fr. mat.	185	Fr. mat.	172

Table 4.1. Reference pressures for each soil layer in the two modeled sections.

Undrained shear strength - c_u
The undrained shear strength was evaluated from data, put together from fall cone tests, direct shear tests and cone penetration tests, and plotted against level in the two soil profiles. The undrained shear strength for each layer was then retrieved from trendlines. See figure 4.4.

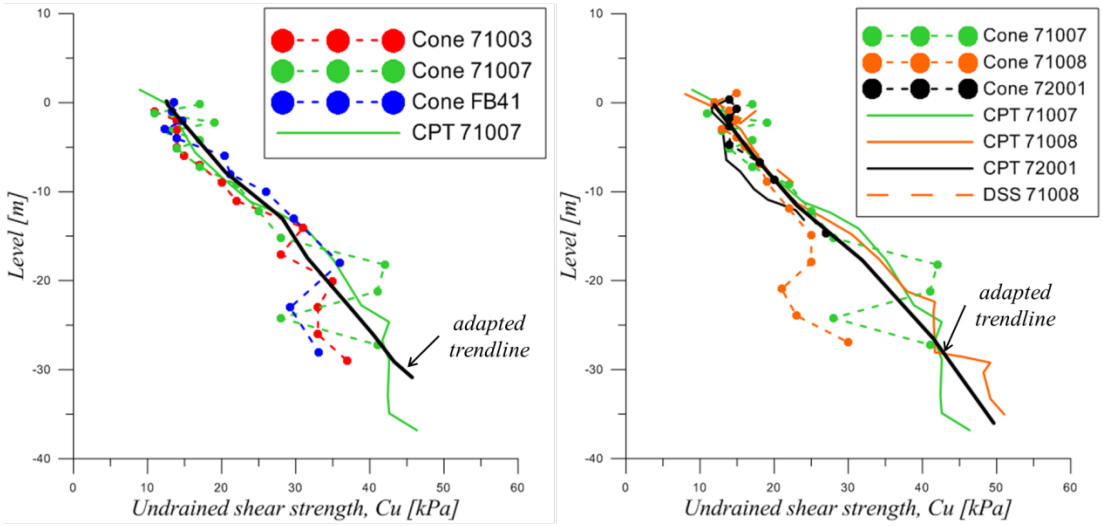

Figure 4.4. Undrained shear strength plotted against level in the two soil profiles. Left: Excavation 1 – section A. Right: Excavation 2 – section B.

4.3 Stiffness evaluation Method 1

In this method, data from CRS tests, in the form of effective stresses and strains, along with the initial void ratio, e_0, of each soil sample, was utilized in order to transform increments of strain into increments of void ratio, by using consolidation theory described in *Craig* (2004). This way, the deformation behavior of the soil was described in terms of how stresses correlate to compression of the voids in the samples, rather than to the samples' volume. See equation (4.5).

$$\frac{\Delta e}{\Delta H} = \frac{1+e_0}{H_0} \tag{4.5}$$

Where

e_0 is the void ratio at the start of the CRS test

Δe is the increment of void ratio

$\frac{\Delta H}{H_0} = \Delta\varepsilon$ is the increment of strain

The void ratios, $e = e(\varepsilon)$, were incrementally calculated over the stress intervals in the CRS tests, using initial void ratio as a starting point, and continuously adding the increment given by equation (4.5). The data provided from the calculations was plotted as the base 10 logarithm, log, of effective stresses, against void ratio. The resulting curves were then used to extract the compression index, C_c, and the swelling index, C_s, which were used as governing stiffness parameters for Method 1. For the principle, see figure 3.3. No unloading cycles had been performed in the CRS tests, for which reason the swelling index, C_s, was evaluated from the part of the curve, prior to the pre-consolidation pressure, σ'_c. Figure (4.5) shows an example on how curves were plotted for the samples collected from bore hole 71008. The black lines in the diagram represent the intervals in which the two parameters were evaluated.

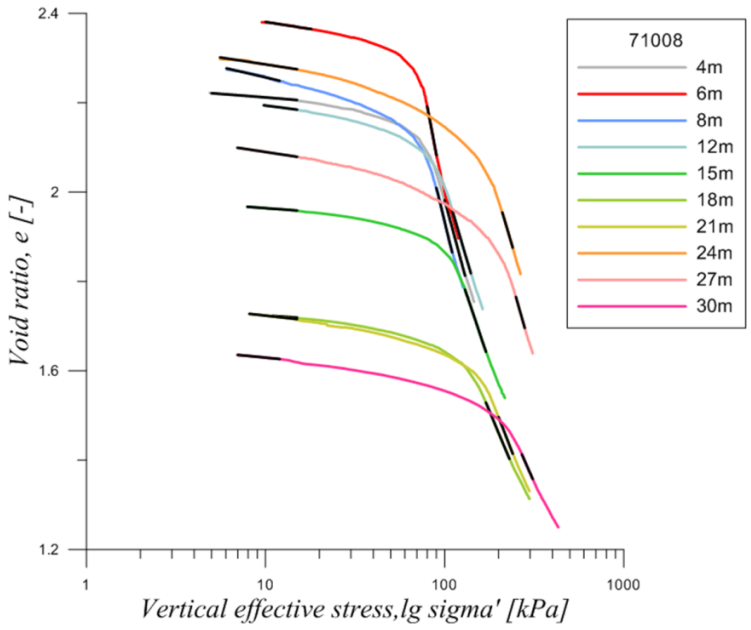

Figure 4.5. The relation of stress: void ratio, plotted for the samples collected from bore hole 71008.

Of the five boreholes considered, there were a number of samples which were suspected of being disturbed. These were excluded from the evaluation. Figure (4.6) contains an example with two curves, from depths 24 and 27 meters of bore hole 71008, with the typical observed characteristics for disturbance, with an indistinctively marked transition from C_s to C_c.

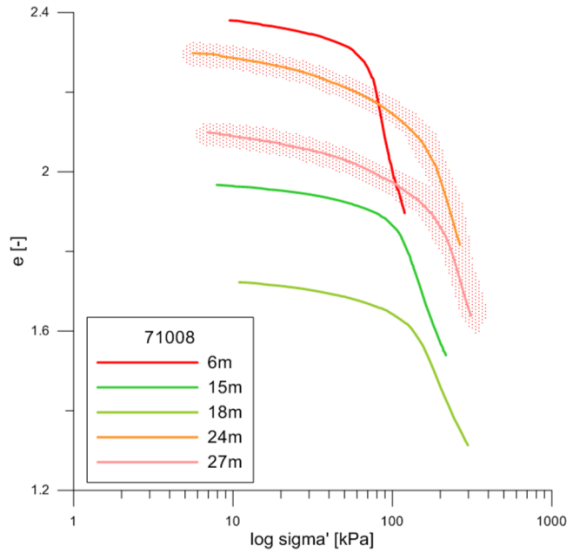

Figure 4.6. Disturbed samples from bore hole 71008.

4.4 Stiffness evaluation Method 2

The procedure referred to as Method 2 was the one used in *Ismail and Teshome* (2011). The main difference, compared to Method 1, is that Method 2 uses the moduli M_0 and M_L, taken from a CRS test, to evaluate stiffness parameters. The reasoning behind the procedure utilized by *Ismail and Teshome* were based on the assumption that, if the Poisson ratios of the materials in the modeled soil profiles are small, discrepancies between the moduli, E_{50} and E_{oed}, used in Hardening Soil, and the moduli M_0 and M_L, retrieved from a CRS test, should not be significant if converted to the same reference pressures (Kullingsjö 2013). The unloading-reloading modulus, E_{ur}, was formulated according to *Sällfors* (2009), who states that documentation from full scale field investigations has indicated that the unloading modulus in-situ is 3 to 5 times the value of M_0, retrieved from an oedometer. *Ismail and Teshome* concluded that 5 times M_0 gave the most realistic result, in their investigation.

It is important to note that the procedure referred to as Method 2, in this report, only regards the derivation of stiffness parameters. Other soil parameters, such as friction angle, Poisson ratio, cohesion and the over consolidation ratio, OCR, as well as the division of soil layers, are in this thesis revised, compared to the ones in *Ismail and Teshome* (2011), in which a friction angle of 20˚was used as input in Plaxis 2D.

4.5 Parameters for the Hardening Soil model

Except for the general parameters, described in the initial section of this chapter, two sets of stiffness parameters, corresponding to *Methods 1 and 2*, were defined as input for the simulations with the Hardening Soil model and HS Small.

4.5.1 Stiffness parameters for Hardening Soil, using Method 1

By using the alternative stiffness parameters option in Plaxis 2D Input, the three reference moduli in the Hardening Soil model were calculated using the compression index, C_c and the swelling index, C_s, according to equations (4.6) and (4.7) (Plaxis 2012a).

$$E_{oed}^{ref} = \frac{2.3(1+e_0)p_{ref}}{C_c} \tag{4.6}$$

$$E_{ur}^{ref} \approx \frac{2.3(1+e_0)(1+\nu)(1-2\nu)p_{ref}}{(1-\nu)C_s K_0} \tag{4.7}$$

Where

K_0 is the soil pressure coefficient during unloading, which in Plaxis 2D is approximated to an average K_0=1, throughout an unloading path.

p_{ref} was taken from table 4.1 above.

E_{50}^{ref} is, in Plaxis 2D, calculated with equation (4.8), as a default (Plaxis 2012a).

$$E_{50}^{ref} = 1.25E_{oed}^{ref} \quad (4.8)$$

However, the use of the relation described in equation (4.8) resulted in some cases of unacceptable ratio between the three moduli, due to a restriction in Plaxis 2D, stating: $E_{50}^{ref} > \frac{1}{20} E_{ur}^{ref}$. For this reason, E_{50}^{ref} had to be increased, as to satisfy this condition, resulting in values ranging from $1.31E_{oed}^{ref}$ to $2.22E_{oed}^{ref}$ within the soil profiles. Values exceeding $2E_{oed}^{ref}$ brings certain limitations to the modeling of a problem (Plaxis 2012a). This issue was, however, addressed through analyses of stress paths, presented in Chapter 8.1.

For the sand- and the frictional material layer, the same reference moduli were used as in *Ismail and Teshome* (2011), since there were no investigations performed on these layers.

4.5.2 Stiffness parameters for Hardening Soil, using Method 2

In Method 2, the reference moduli for Hardening Soil are based on M_0 and M_L, and are also, in accordance with Plaxis 2D default, related to the reference pressure, $p_{ref} = 100$ kPa. For this reason, the three reference moduli were defined as transformed values of M_L, M_0 and $5M_0$, respectively, according to equations (4.9) to (4.11) (Ismail & Teshome, 2011).

$$E_{oed}^{ref} = \frac{M_L}{\left(\frac{p^{ref}}{K_{0*}p_{ref=100\,kPa}}\right)^m} \quad (4.9)$$

$$E_{50}^{ref} = \frac{M_0}{\left(\frac{p^{ref}}{p_{ref=100\,kPa}}\right)^m} \quad (4.10)$$

$$E_{ur}^{ref} = \frac{5M_0}{\left(\frac{p^{ref}}{p_{ref=100\,kPa}}\right)^m} \quad (4.11)$$

Where

p^{ref} was taken from table 4.1.

m=1 for clay.

4.6 Input parameters for HS Small

The HS Small model uses the same input as Hardening Soil, with the addition of two parameters, describing the small-strain response of the soil (Benz, 2007). Although there are numerous relationships describing this phenomenon, three different approaches have been used in this report. Due to the absence of laboratory and field

in-situ tests, regarding the value on the small-strain modulus G_0 and the threshold strain amplitude $\gamma_{0.7}$, the relations utilized in this report are based on approximations and simple empirical formulas. From here on, the sets of small-strain parameters will be referred to as the *Approximate* and the *Empirical approaches A and B*.

4.6.1 The Approximate approach

The approximate approach was included in the investigation due to the lack, or scarcity, of information on soil parameters, required for the use of available empirical relations, in order to ensure that the initial shear stiffness of the soil was defined within the right order of magnitude. The approach is based on a relation stating that the magnitude of the small-strain modulus, G_0, is correlated to the unloading-reloading shear modulus, G_{ur}, of a material. Thus, the formula only provides a rough estimate, given by equations (4.12) and (4.13) (Karstunen, 2012).

$$G_0^{ref} = (2.5 \text{ to } 10)G_{ur}^{ref} \tag{4.12}$$

$$G_{ur}^{ref} = \frac{E_{ur}^{ref}}{2(1+\nu)} \tag{4.13}$$

For the threshold shear strain $\gamma_{0.7}$, a similarly simple relation was used (Karstunen, 2012). See equation (4.14).

$$\gamma_{0.7} = (1 \text{ to } 2)10^{-4} \tag{4.14}$$

The values chosen as input in the simulations with the approximate small-strain approach were then defined as averages of equations (4.12) and (4.14). See equations (4.15) and (4.16).

$$G_0^{ref} = 6.25 * G_{ur}^{ref} \tag{4.15}$$

$$\gamma_{0.7} = 1.5 * 10^{-4} \tag{4.16}$$

4.6.2 Empirical approaches A and B

In the empirical approaches A and B, the small-strain response of the soil has been specified using empirical relations. In *Empirical Approach A*, the small-strain modulus G_0 was calculated with equation (4.17), in which the plasticity index I_P was specified using equation (4.18), since the plastic limit of the clay was unknown (Bråten et al. (2010); Hansbo, 1975). In *Empirical Approach B*, the value of the small-strain modulus was specified using equation (4.19), presented in *Larsson & Mulabdic* (1991), using the same I_P. Due to the small amount of information from DSS tests, the undrained shear strength in (4.17) was based on the trend lines in figure 4.4, possibly yielding more conservative values, and thus a slightly lower small strain stiffness.

Empirical Approach A

$$G_0 = {c_u}^{DSS}\left(325 + \frac{55}{\left(\frac{I_P}{100}\right)^2}\right) \quad (4.17)$$

$$I_P = 0.75(w_L - 26) \quad (4.18)$$

Empirical Approach B

$$G_0 = c_u\left(\frac{208}{I_P} + 250\right) \quad (4.19)$$

The threshold shear strain $\gamma_{0.7}$, for both *Empirical A and B*, was retrieved using a procedure described in the PhD thesis by *Benz* (2007), based on work by Stokoe et al. (2004), in which linear interpolation of $\gamma_{0.7}$, against plasticity index, between the values given in (4.20) and (4.21), was proposed.

$$I_P = 0 \rightarrow \gamma_{0.7} \approx 1 * 10^{-4} \quad (4.20)$$

$$I_P = 100 \rightarrow \gamma_{0.7} \approx 6 * 10^{-4} \quad (4.21)$$

4.7 Input parameters for S-CLAY1

Since no step-wise oedometer tests had been performed on the piston samples taken at the site, the effects of interparticle bonding in the soil had not been investigated. For this reason, there was little use in analyzing the problem with S-CLAY1S, since that would have incorporated even greater uncertainties regarding the predicted horizontal deformations in the soil. S-CLAY1 was therefore considered a sufficient option, taking anisotropy into account, but leaving out the effect of interparticle bonding. In this section, the derivation of key parameters, required for S-CLAY1, is described.

Ratio of deviatoric strains to volumetric strains – η_{K0}
This parameter describes the ratio between deviatoric stresses, q, and volumetric stresses, p′, during triaxial K_0-compression, and was calculated according to equation (4.22) (Muir Wood, 1990).

$$\eta_{K0} = \frac{q}{p'} = \frac{\sigma_1' - \sigma_3'}{\frac{1}{3}(\sigma_1' + 2\sigma_3')} = \frac{\sigma_1' - K_0\sigma_1'}{\frac{1}{3}(\sigma_1' + 2K_0\sigma_1')} \quad (4.22)$$

Critical state line for triaxial compression
The slope of the Critical state line for triaxial compression, M, was calculated according to equation (4.23) below (Muir Wood, 1990).

$$M = \frac{q}{p' + c'\cot\phi'} = \frac{6\sin\phi'}{3 - \sin\phi'} \quad (4.23)$$

Yield curve inclination, 1D Consolidation - α_{K0}
The initial inclination of the yield locus was defined by equation (4.24) (Karstunen et al. 2005).

$$\alpha_{K0} = \frac{\eta_{K0}^2 + 3\eta_{K0} - M^2}{3} \quad (4.24)$$

Soil parameter – μ
The soil parameter μ controls the rate at which the yield curve inclination α_{K0} is able to reach its present target value. There is no easy way of finding the value of μ for a certain soil, but according to *Karstunen* (2013), most soils will have a value of μ ranging from $10/\lambda$ to $20/\lambda$. For this reason, μ was calculated according to the formula in equation (4.25).

$$\mu = \frac{15}{\lambda} \quad (4.25)$$

Soil parameter – β

This parameter describes the effectiveness in rotating the yield curve and was calculated with equation (4.26) (Karstunen et al. 2005).

$$\beta = \frac{3(4M^2 - 4\eta_{K0}^2 - 3\eta_{K0})}{8(\eta_{K0}^2 - M^2 + 2\eta_{K0})} \quad (4.26)$$

4.7.1 Stiffness parameters for S-CLAY1, using Method 1

As was described in Chapter 3.2, the two stiffness parameters λ and κ can be derived from C_C and C_S, according to equation (4.27) to (4.30) below.

$$\lambda^* = \frac{C_c}{2.3(1+e_0)} \qquad \lambda = \lambda^*(1 + e_0) \quad (4.27, 4.28)$$

$$\kappa^* \approx \frac{2C_s}{2.3(1+e_0)} \qquad \kappa = \kappa^*(1 + e_0) \quad (4.29, 4.30)$$

4.7.2 Stiffness parameters for S-CLAY1, using Method 2

This second set of λ and κ was derived from the reference moduli for Hardening Soil, specified according to Method 2, using M_0 and M_L as direct input parameters. The relations are described by equation (4.31) and (4.32) below (Plaxis 2012a).

$$\lambda^* = \frac{p^{ref}}{E_{oed}^{ref}} \qquad \lambda = \lambda^*(1 + e_0) \quad (4.31)$$

$$\kappa^* \approx \frac{2p^{ref}}{E_{ur}^{ref}} \qquad \kappa = \kappa^*(1 + e_0) \quad (4.32)$$

Where

p^{ref} is the reference pressure, taken from table 4.1, above.

E_{oed}^{ref} and E_{ur}^{ref} are the reference moduli defined in Chapter 4.5.2.

4.8 Input parameters for modified Cam clay

This model utilizes the same sets of parameters as the model S-CLAY1, but with the soil constants describing fabric anisotropy, α_{K0} and μ, set to zero (Wheeler et al., 2003).

5 MODELING

5.1 Soil profiles for the modeled sections

Starting from routine investigations and CPT´s, two coarse initial soil profiles were made for the analyzed sections. These can be seen in figures 5.1 and 5.2. The soil below the level -32 meters consists of thick layers of frictional material, on which no extensive investigation has been performed (Kvick, 2012).

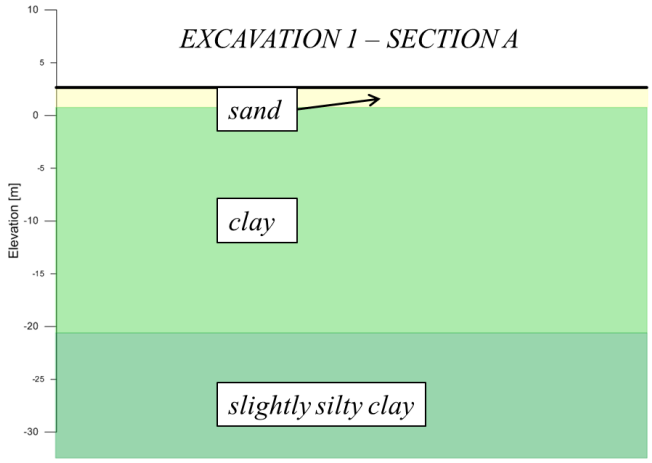

Figure 5.1. Initial soil profile for Excavation 1, for the preliminary road under the railway bridges.

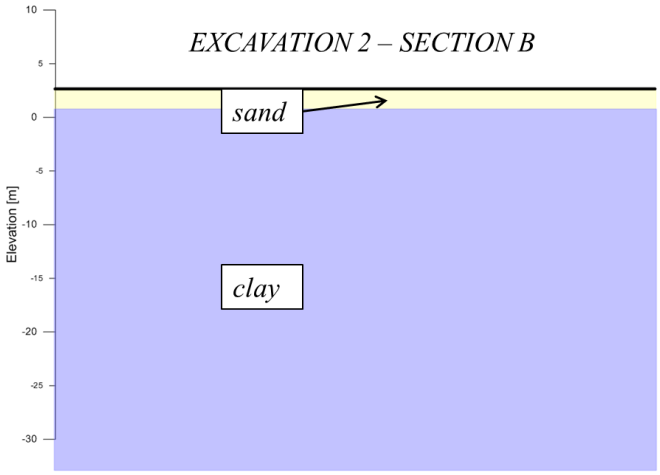

Figure 5.2. Initial soil profile for Excavation 2, for the final redrawing of the road E45.

The soil division above would enable a rough analysis of the soil behavior, and in order to achieve a result as credible as possible, a deeper investigation was made regarding the internal variation of properties in the soil profiles.

The parameters which were chosen as governing for the finer division of layers are the unit weight of soil, or density, water content and the stiffness parameter λ. The unit weight and water content of the soil indicate differences in soil characteristics and the stiffness parameter λ gives information regarding the soil´s response to loading. The unloading stiffness parameter κ would be a more logical choice as governing factor for the soil layer division, but the distribution of κ against depth is more scattered than that of λ, and would thus result in a more difficult and uncertain evaluation of the layer division. Density and water content were retrieved from routine investigations performed on piston samples collected from various depths, ranging from approximately 2 to 40 meters, at five locations along the crossing railway. See figure 4.1, in chapter 4.1, where the five investigated bore holes and analyzed sections A and B, are pointed out. The preliminary road section, excavation 1, is displayed in green while the final redrawing of the road, excavation 2, is shown in blue.

For excavation 1, analyzed in section A, the bore holes 71003, FB41 and 71007 were used for the partitioning of layers, while for excavation 2, analyzed in section B, data from bore holes 71007, 71008 and 72001 have been utilized. For excavation 1, the plotted values on density, water content and stiffness λ, along with trend lines fitted against data points can be seen in figure 5.3. The division of layers, based on the trend lines, can be seen in figure 5.4. For excavation 2, the corresponding plots are shown in figures 5.5 and 5.6.

Due to the proximity of excavation 1, to bore holes 71003 and FB41, greater weight were given to the data retrieved from these two bore holes, than that from 71007. For excavation 2, the relatively small amount of data available from 72001 lead to trend lines being predominately dependent on data from 71007 and 71008. The soil layers were chosen to represent the transitions in inclination of the fitted trend lines, creating five different clay layers in section A, and four in section B. The model input parameters, as well as soil properties, were chosen as the average in respective layer.

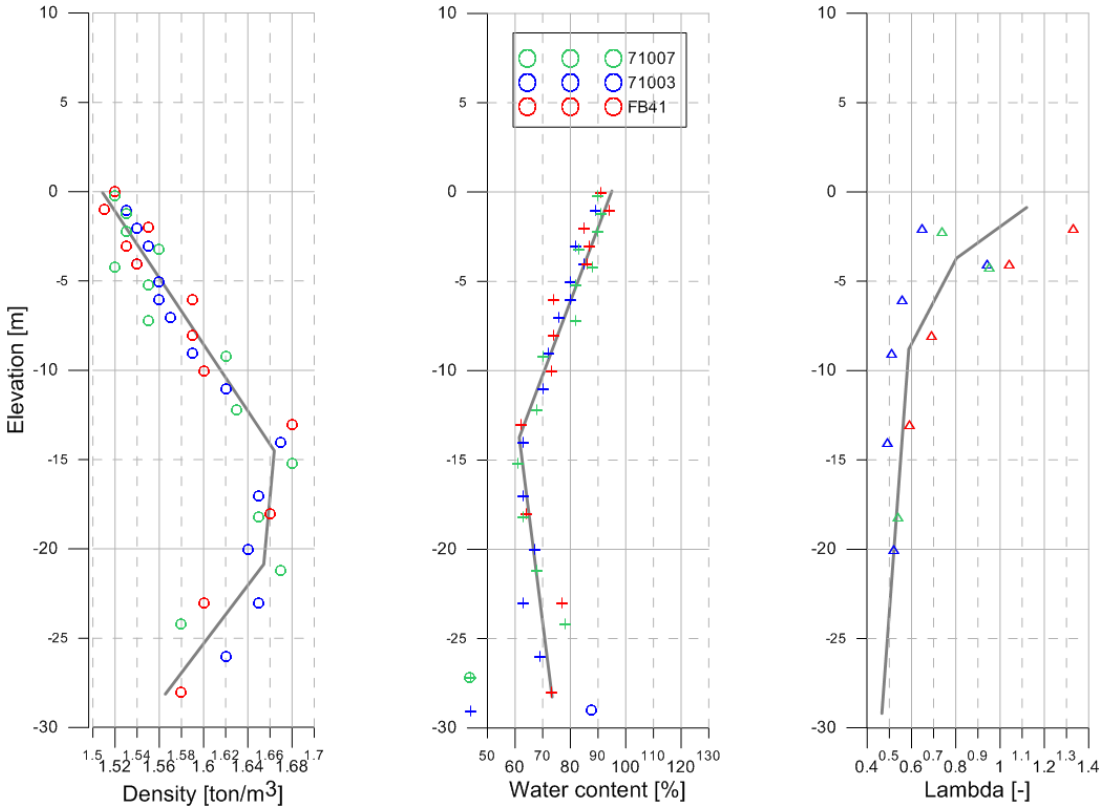

Figure 5.3. Excavation 1 - section A. Density, water content and stiffness λ, plotted against level.

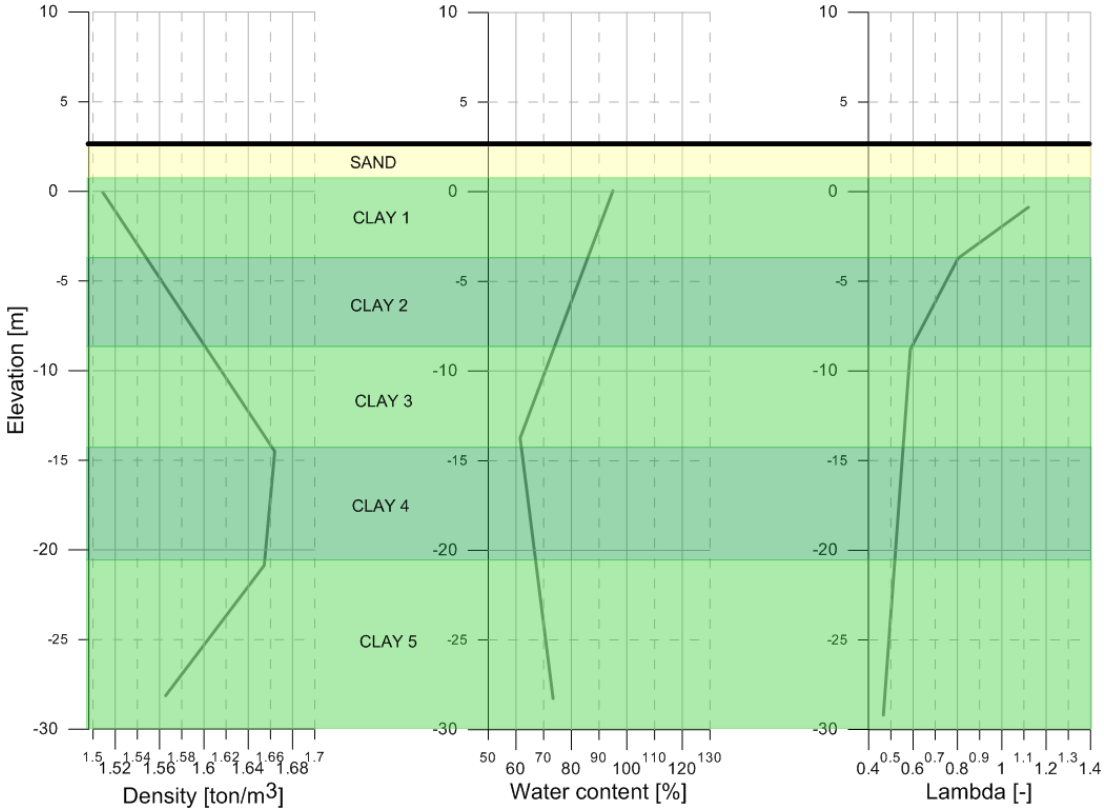

Figure 5.4. Layer division for excavation 1 – section A, resulting from the data shown in figure 5.4.

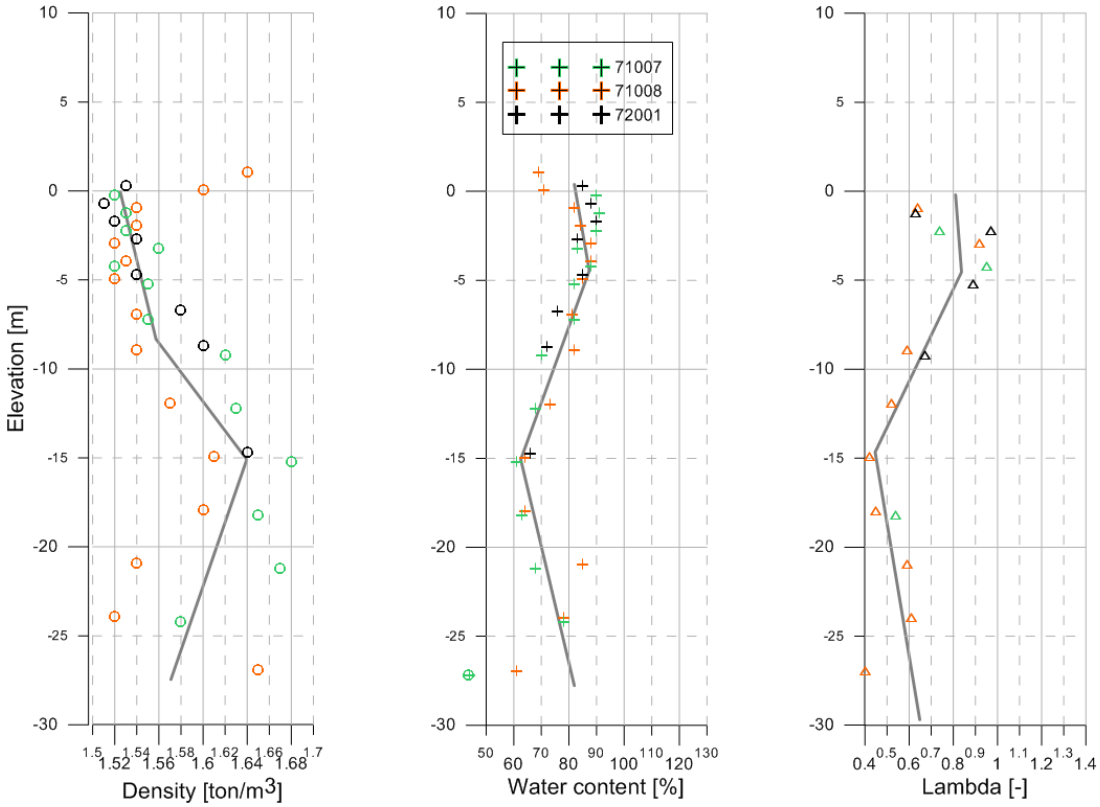

Figure 5.5. Excavation 2 - section B. Density, water content and stiffness λ, plotted against elevation.

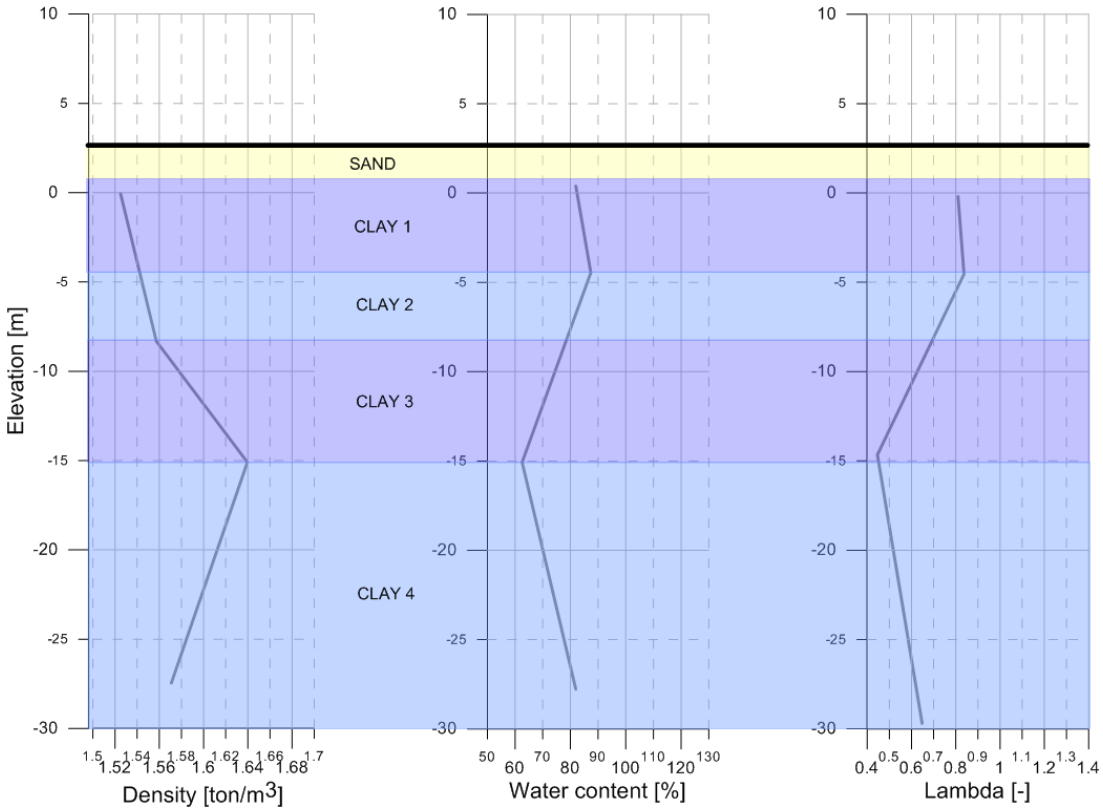

Figure 5.6. Layer division for excavation 2 – section B, resulting from the data shown in figure 5.6.

As can be seen in the soil profiles, all soil layers, as well as the ground surface, were assumed to be horizontal in this investigation. This is a simplification, since there were slight variations in the topography at the site. However, for a more realistic representation of the ground surface and possible inclination of the soil layers, additional work and field investigations would have been needed, and some modeling-related sacrifices, such as the disabling of K_0-consolidation, would have been required.

5.2 Model geometry and stages of the excavation process

The soil masses in the two sections were excavated stepwise, in layers. This has been included in the two models by partitioning the excavated sections into sub-layers, after which a staged construction were simulated in the calculation stages.

In the investigated section A, the existing road RV45 (figure 2.2) intersected the preliminary road, for which excavation 1 was made, and it was thus included in the modeled geometry. Since the ground surface was defined as flat in the representation of the initial site, while the existing road were lowered relative to the ground surface, a representative volume of soil (Cluster 1 in figure 5.7) had to be removed after the K_0-consolidation phase. The deformations resulting from this modification of the initial conditions were then set to zero before the initiation of the remaining excavation stages, to the level of the actual excavation bottom. The three soil clusters, representing the excavation stages for section A can be seen in figure 5.7, and the calculation process can be summarized into bullets according to table 5.1.

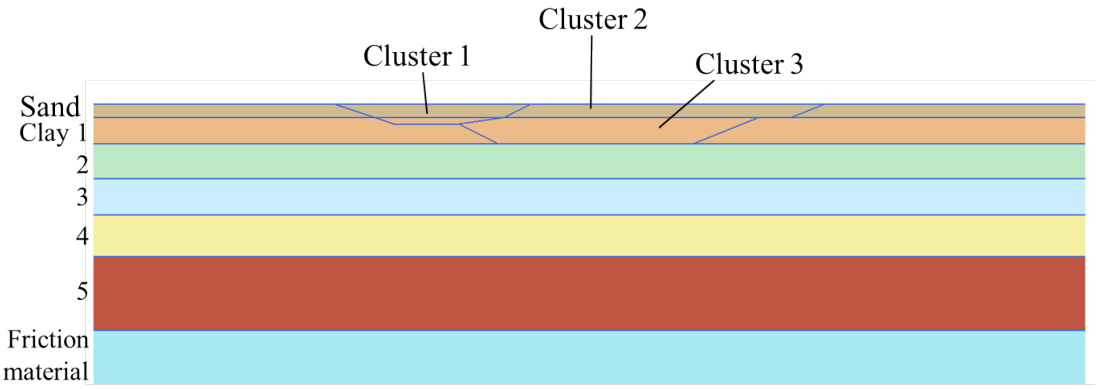

Figure 5.7. Excavation 1 – section A, with the three soil clusters pointed out.

Phase	Description
K0-consolidation	Generation of initial stresses
Staged construction: Cluster 1	Removal of soil representing the existing road. Deformations set to zero.
Staged construction: Cluster 2	Excavation stage 1
Staged construction: Cluster 3	Excavation stage 2

Table 5.1. Calculation phases for the analysis of excavation 1 – section A.

For the analysis of the second excavation, observed in section B, the modeling was more straightforward. Initially, the contractor performed some unloading measures in

the surroundings of the site, through removal of a portion of the sand layer. After this, the remaining clusters, marked in figure 5.8, were excavated sequentially down to design level. The stages of the simulation are listed in table 5.2.

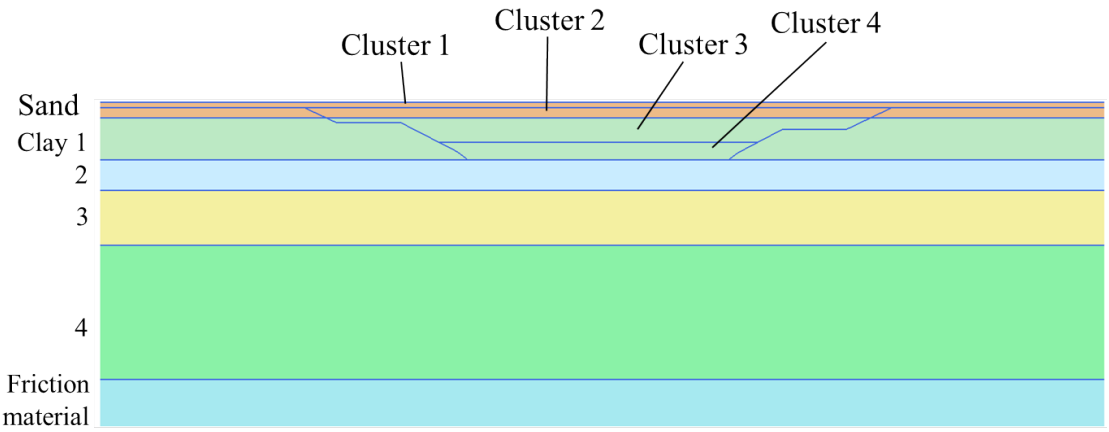

Figure 5.8. Excavation 2 – section B, with the four soil clusters pointed out.

Phase	Description
K0-consolidation	Generation of initial stresses
Staged construction: Cluster 1	Excavation stage 1. Surface unloading. Removal of soil.
Staged construction: Cluster 2	Excavation stage 2
Staged construction: Cluster 3	Excavation stage 3
Staged construction: Cluster 4	Excavation stage 4

Table 5.2. Calculation phases for the analysis of excavation 2 – section B.

5.3 Finite element meshes

The finite element meshes were generated analogously for both excavations, and in the process of creating the geometries, some general rules from finite element analysis were applied. Since the accuracy of an analysis increases with decreasing element size, finer mesh detail was chosen around the perimeters of the excavated sections, as well as in the soil around the positions of the inclinometers (Ottosen & Petersson, 1992). In contrast, as can be seen in figures 5.9 and 5.10, the sides of the excavations opposite to those where inclinometers had been installed were modeled more coarsely, the purpose of which being to avoid unnecessarily cumbersome calculation processes. The local refinements of the mesh were aided by the use of additional geometry points in the model, placed below the slopes in which the inclinometers were installed.

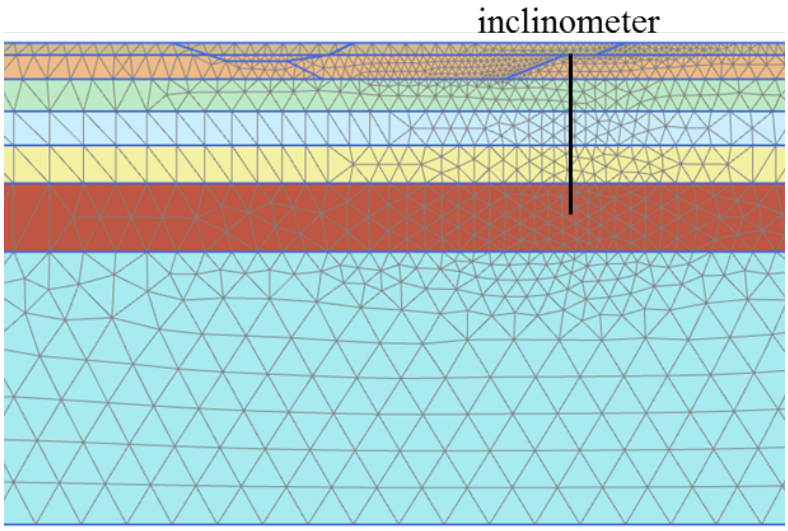

Figure 5.9. Finite element mesh for excavation 1 – section A.

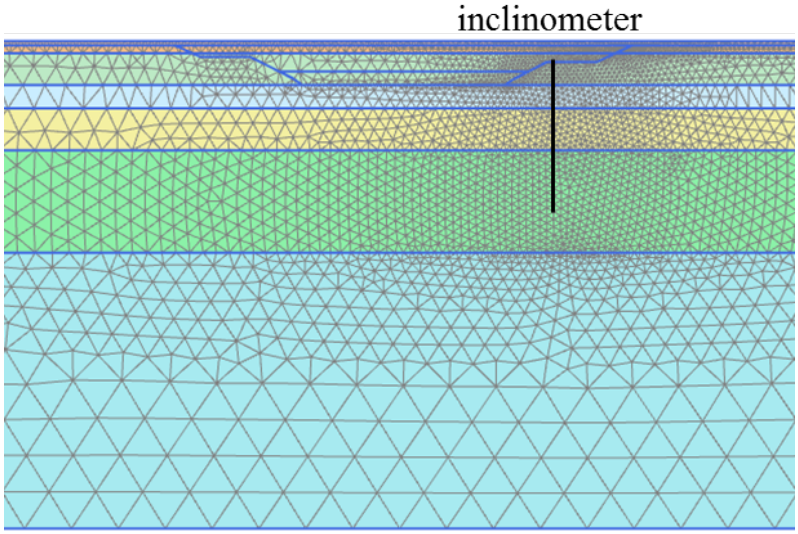

Figure 5.10. Finite element mesh for excavation 2 – section B.

Yet another characteristic, which was given attention in the generation of the meshes, was the aspect ratio of the elements. The aspect ratio can be seen as a quality indicator

for the element shape in a model, and is determined using the smallest and largest distance within an element (Ottosen & Petersson, 1992). Ideally, all elements in a mesh should be in unity, meaning an aspect ratio of 1. This is hardly feasible, but in this report, a number of mesh combinations were tested, after which an adequate aspect ratio was reached. A visualization of the distribution of the parameter in the two meshes can be seen in figure 5.11. As can be seen in the figure, the regions around the positions for the inclinometers are the ones with the most consistent quality. Table 5.3 contains some basic information from the modeled sections.

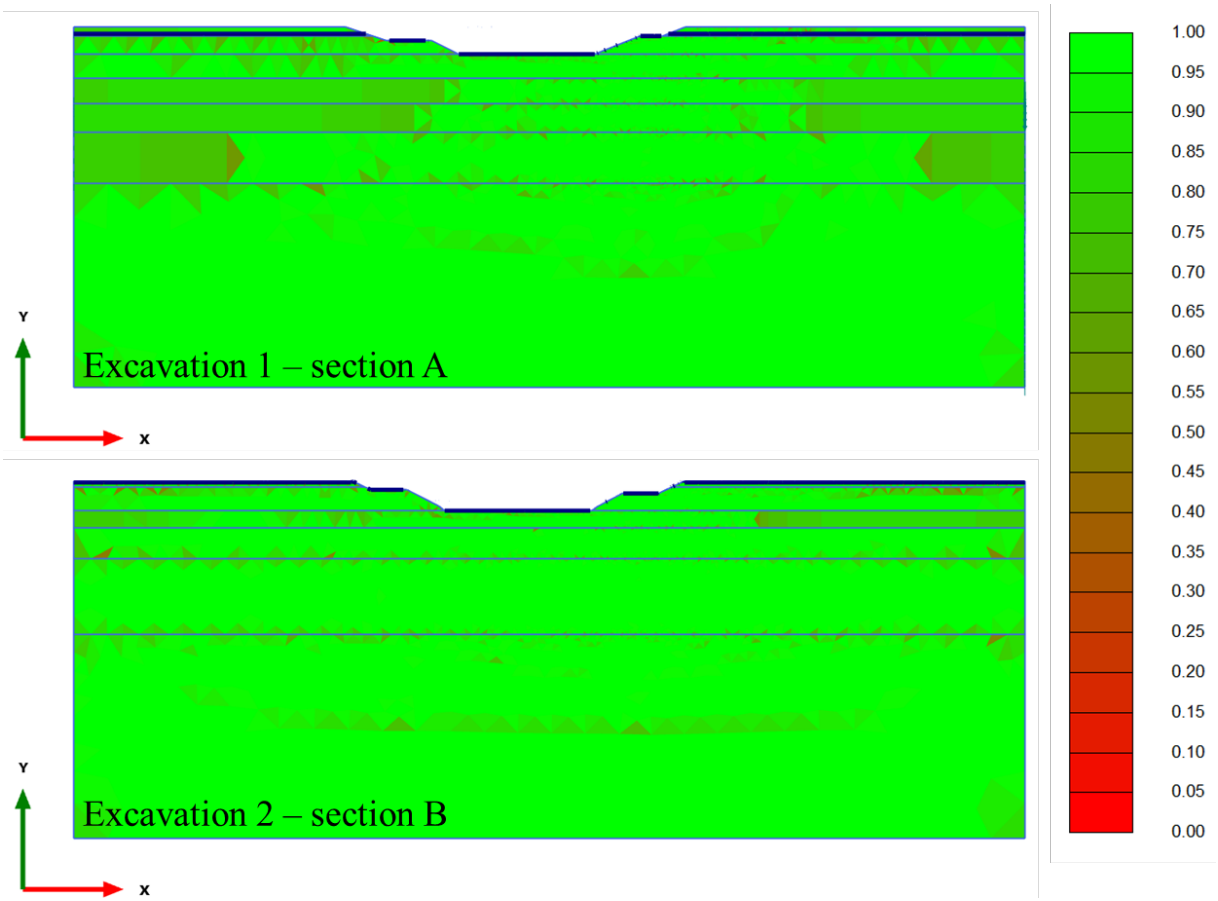

Figure 5.11. Quality of the two generated meshes, presented as aspect ratio.

	Excavation 1- section A	Excavation 2 – section B
Elements (15-noded)	2396	7890
Nodes	19489	63645
Average element area	2.64	1.455
Aspect ratio – mean	0.940	0.954
Aspect ratio – standard deviation	0.084	0.077

Table 5.3. Elements and nodes in the meshes of the two modeled sections.

6 MEASUREMENTS

6.1 Inclinometer readings

The results from the simulations for Excavation 1 were compared to the inclinometer at USP1, installed at the terrace in the slope between the two bridge supports south of the excavation. The A-axis of the inclinometer is aligned with the railway, meaning it has a direction perpendicular to the investigated excavation. Thus, the modeled deformations were directly compared to the displacements recorded in the A-axis of the inclinometer. See figure 6.1 for the location and direction of the inclinometer relative to the excavation.

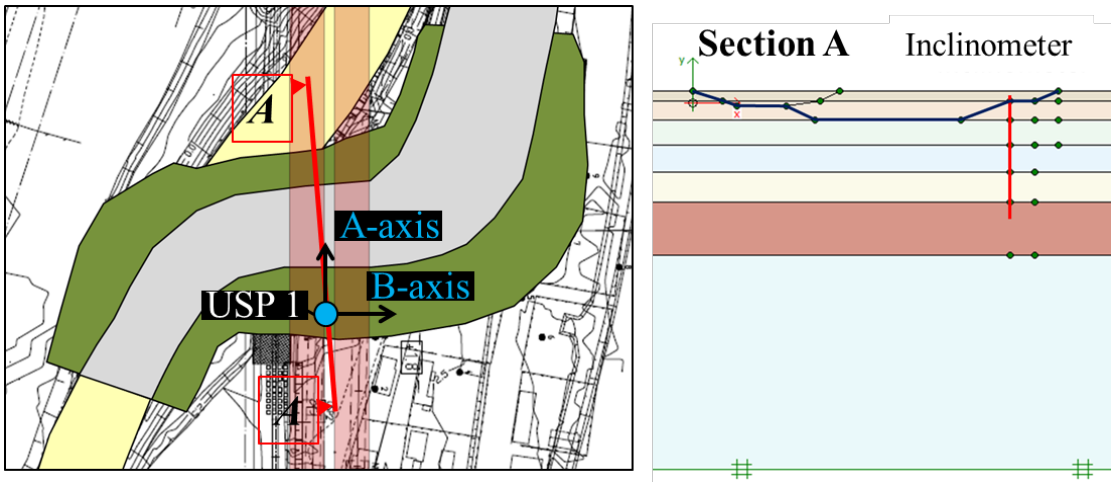

Figure 6.1. Position of inclinometer USP1 relative to the analyzed section A, Excavation 1. Left: Plane view. Right: Section view.

For the second excavation, the inclinometer´s coordinate system was rotated 20˚ relative to the direction of the excavation, see figure 6.2. For this reason, the documented displacements from the inclinometer at USP4 were transformed, from being expressed in terms of A and B, relative to the inclinometer, to A* and B* relative to the excavation, see figure 6.3. This was accomplished through a projection of measuring points onto the B*-axis, being normal to the direction of the excavation.

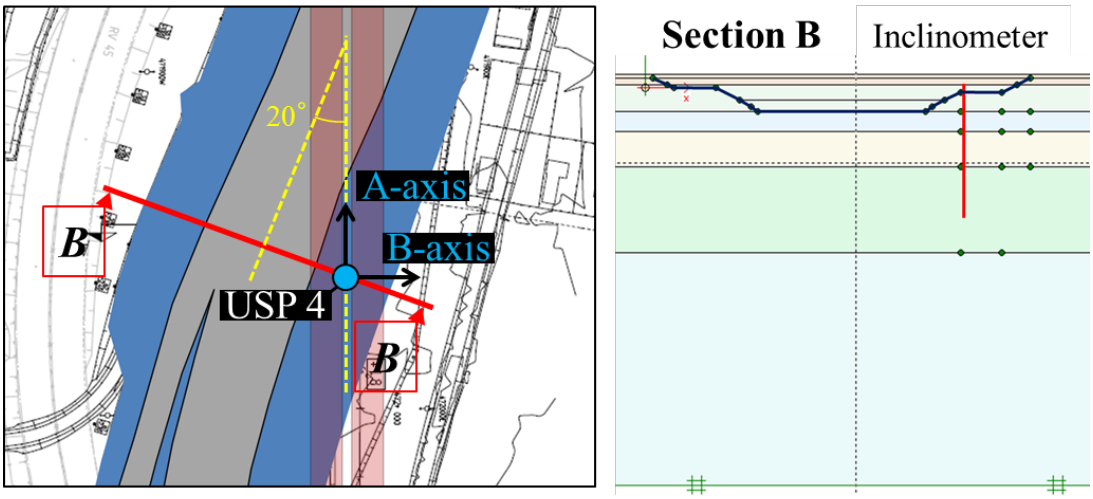

Figure 6.2. Position and orientation of inclinometer USP4 relative to section B, in Excavation 2. Left: Plane view. Right: Section view.

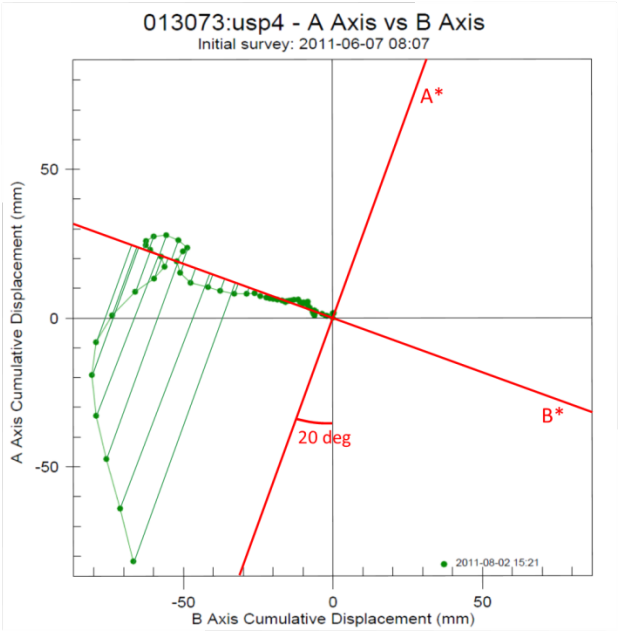

Figure 6.3. Schematic figure showing the relative rotation of the A- and B*-axes and the projection of data points.*

Since the analyses were performed with undrained conditions in the clay, the inclinometer readings were chosen to represent the dates of finalization for the two excavations. Below, in figure 6.4, the displacement curve for each excavation can be seen. For excavation 1, displacements from the 26th of January are given by the A-axis, while for excavation 2, the resultant of the A- and B-axes, from the 2nd of August, are shown in plane view.

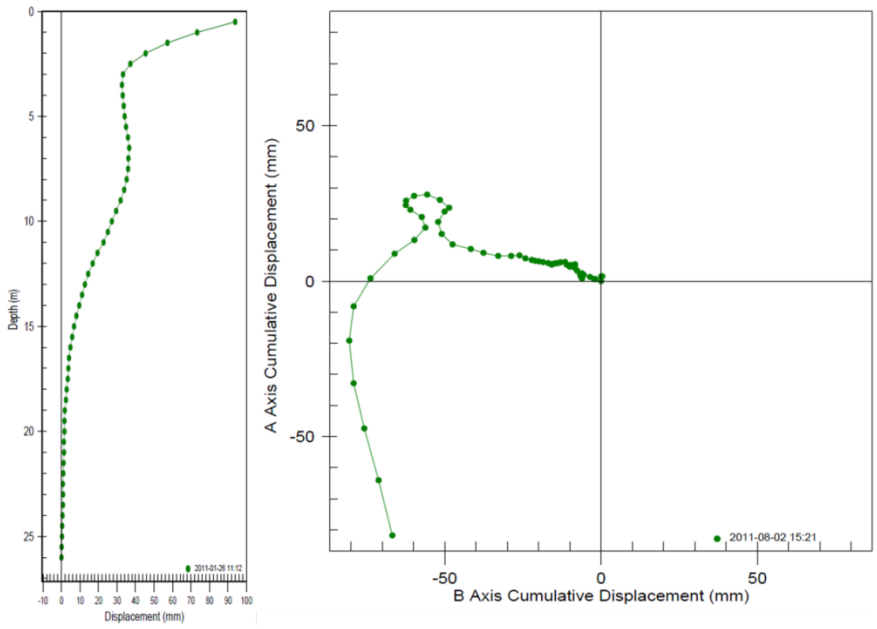

Figure 6.4. Left: Displacement curves for Excavation 1 – section A, 26th of January. Right: Displacement curves for Excavation 2 – section B, 2nd of August.

By expressing the data points in terms of level, rather than against depth, and by projecting the readings from USP4 onto the B*-axis, the displacement curves shown in figure 6.5 were achieved. The curves were then used for comparison with the results from the simulations. The curve to the left, for Excavation 1 – section A, was known to have been disturbed close to the ground surface, which resulted in the large deformation above the level -3 m (dashed ellipse). Furthermore, the shape of the curve section located between the levels -3 and -7 meters (solid ellipse) is assumed to have been altered by the suppressive effect of the bridges foundation. Regarding the curve to the right, for Excavation 2 – section B, it has been assumed that the drastic decrease in deformation close to the ground surface may also be attributed to the proximity of the bridge foundation. Remaining fluctuations might be due to the formation of slip surfaces, but may also be a result of local disturbances from the installment of the instrument, or from minor measurement errors.

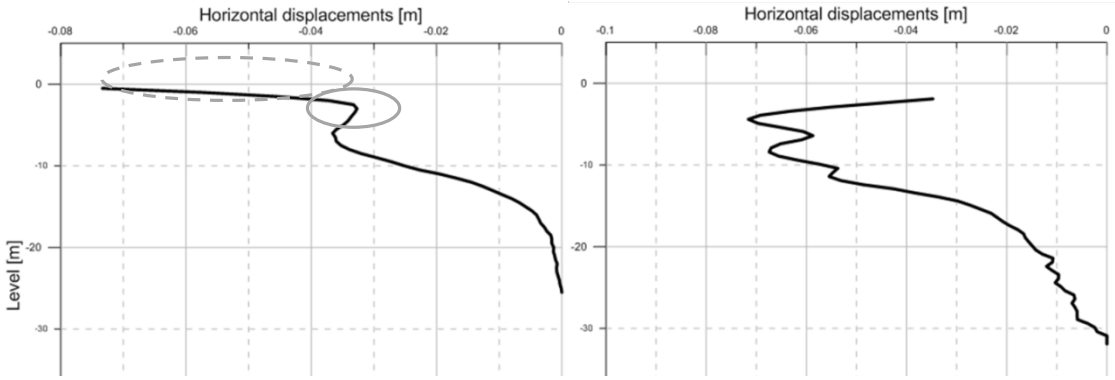

Figure 6.5. Left: Inclinometer readings of horizontal displacements in the direction transversal to Excavation 1. Right: Inclinometer readings of horizontal displacements in the direction transversal to Excavation 2.

6.2 Surface gauges

An additional assessment was made regarding how well the models are able to simulate the movement at the ground surface. For this, a number of gauges, which were used for measuring horizontal deformations throughout the contracting process, were selected, in the area around the two excavations. The positions of the points can be seen in figure 6.6.

The control peg measurements for Excavation 1 were taken from the 31st January 2011, five days after finalization of the digging for the preliminary road. For Excavation 2, the measurements for points 11 and 12 represent the 1st August 2011, while points 13 and 14 represent the 26th July of the same year. Thus, the measurements are not from the actual dates of completion, since the two excavations were finalized on the 26th January and 2nd August, respectively. The reason being, that measurements were not available for all dates.

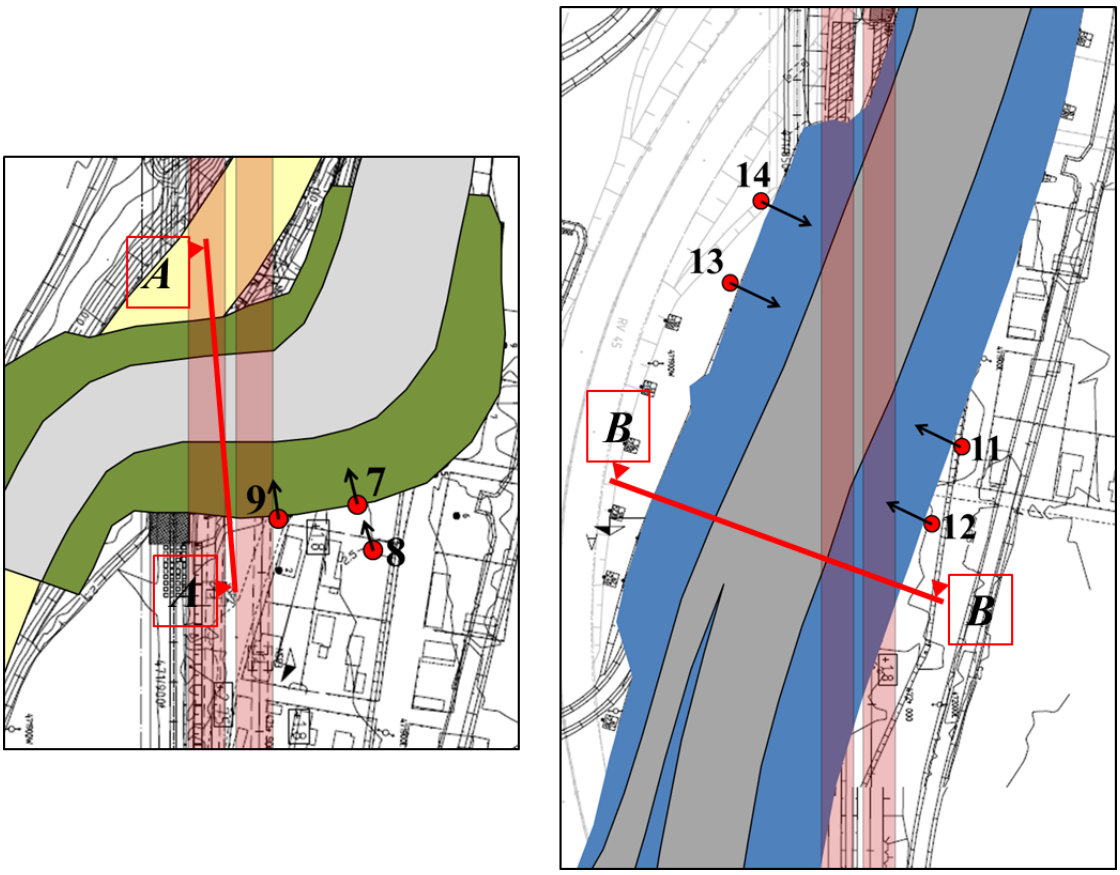

Figure 6.6 Position of control pegs at the sites of the two excavations.

7 RESULTS

7.1 Horizontal displacements - Excavation 1 – section A

The simulations for Excavation 1 – section A were performed with all three soil models, combined with sets of stiffness parameters retrieved from both methods 1 and 2. In the simulations with HS Small, all three approaches regarding the specification of the small strain response, the approximate and empirical approaches, were included. In addition, a simulation was made with the implementation of modified Cam clay, available through deactivation of the rotational hardening law in S-CLAY1. This simulation was made as a reference against the anisotropic model, since it would indicate whether or not plastic deformations occurred in the soil profile, and thus, if the inclusion of anisotropy provides any advantages in the modeling of the two excavations. See table 7.1. S-CLAY1 and modified Cam clay was, however, only used for modeling the clay in the two excavations. For the sand and for the layer of frictional material, HS Small – Approximate approach was used instead, due to the lack of laboratory tests on these materials. It was decided that the results regarding the deformations in the clay would be more easily compared if the modeling of the materials with unknown properties was identical in the simulations. It was also noted that the choice of soil model in the sand layer was of minor importance for the magnitude of the simulated horizontal deformations, probably because the sand above the position of the inclinometer was removed is removed in the simulation. The displacement curves for Excavation 1 – section A, can be seen in figures 7.1 and 7.2. The results from the Hardening Soil and the HS Small models are displayed in figure 7.1, while the results from S-CLAY1 and modified Cam clay are presented in figure 7.2. The part of the inclinometer curve, plotted with a black dashed line, is suspected to be disturbed, as was accounted for above. It is assumed that, had it not been affected by the bridge foundation and interference during the contracting process, the upper part of the curve would have been similar in shape to the simulated displacements. For this reason, the simulated deformations have been compared mainly to the solid part of the curve.

Simulations		Stiffness parameters	
Excavation 1 - section A		Method 1	Method 2
Hardening Soil		✓	✓
HS Small	Approximate	✓	✓
	Empirical	✓	✓
S-CLAY 1		✓	✓
MCC		✓	-

Table 7.1. Combinations of soil model and stiffness used in the simulations on Excavation 1.

As can be seen in figure 7.1, the Hardening Soil model shows notably different displacement curves when using stiffness parameters from the two different methods. Method 1 (solid green) produces displacements which significantly over-estimates the actual deformations. The shape of the curve is, however, corresponding fairly well to the inclinometer readings, according to which the deformations are markedly larger a few meters below the ground surface than at greater depths. Method 2 (solid orange) produces deformations which may be closer to the measured displacements, in terms of magnitude of the largest displacement. It only, however, manages to do so above the level -10 meters, below which it fails to capture both the actual deformations and the general trend of the development of deformations as the depth increases.

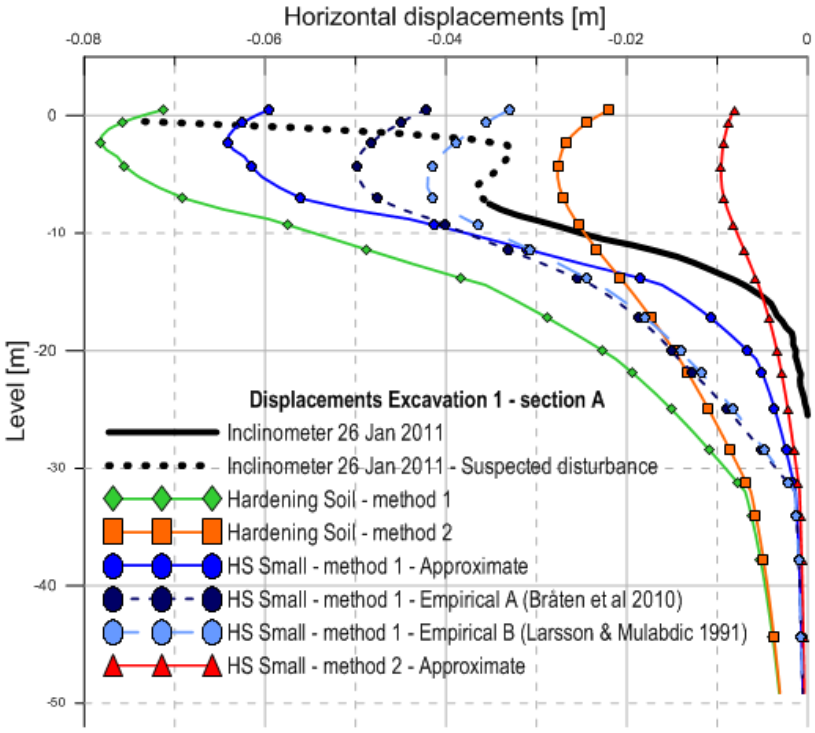

Figure 7.1. Displacement curves for Excavation 1 – section A, retrieved from simulations with the Hardening Soil model and HS Small.

The displacement curve from the HS Small model with approximated small strain response, using stiffness parameters from method 1 (solid blue), has a shape which

best corresponds to the inclinometer reading, of the five curves shown in figure 7.1. The magnitude of the simulated deformations is slightly over-estimated, but the general trend is represented in a satisfactory manner. The HS Small model – method 1, with the empirical approaches for small strain response (dashed light blue and dark blue), has similar shapes. These do, however, seem to predict a softer response in the soil at larger depths, similar to the simulations with Hardening Soil – method 1 (solid green). As for the use of the HS Small model combined with stiffness parameters retrieved with method 2 (solid red), it can be seen that it fails to capture the behavior of the soil, as the deformations are vastly under-estimated.

The model S-CLAY1, with stiffness parameters from method 1 (solid purple), seems to predict the magnitude of the largest displacements fairly accurately, considering it connects well to the part of the inclinometer curve which is assumed to not have been significantly altered or suppressed due to interference closer to the ground surface. At greater depths, however, the deformations are over-estimated, which was anticipated due to the model's inability to account for the small strain response of the soil. The deformation curve from modified Cam clay (solid green) is close to identical to S-CLAY1, which indicates that for this excavation, no substantial plastic deformations are predicted. The small visible difference may, however, indicate that S-CLAY1 predicts stresses on the verge of the elastic envelope, and that additional unloading would possibly mean propagation of plastic strains in the southern slope of the excavation. As with Hardening Soil and HS Small, S-CLAY1, in combination with stiffness parameters from method 2 (solid brown) significantly under-estimates the horizontal deformations and fails to capture the general deformation behavior over depth in the soil profile.

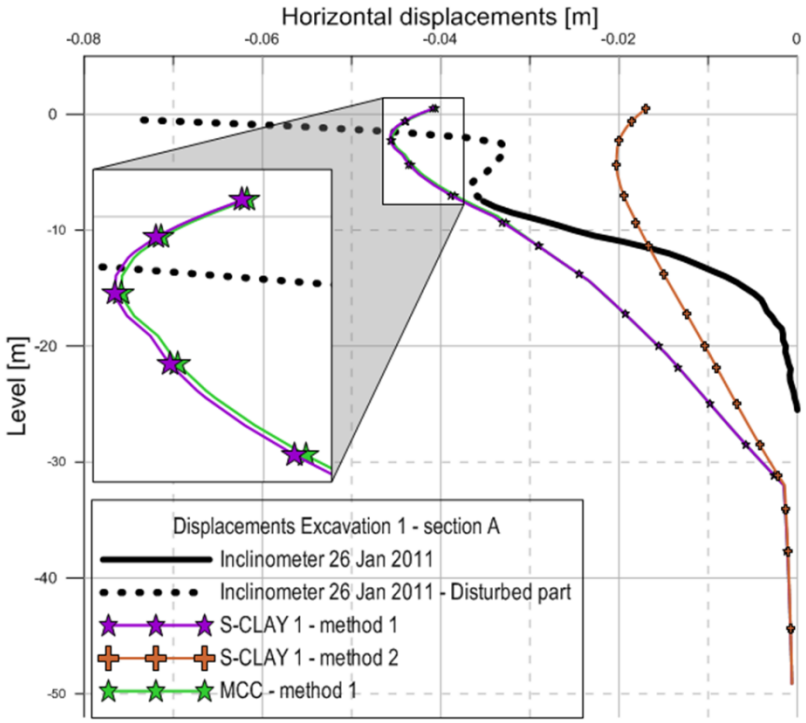

Figure 7.2. Displacement curves for Excavation 1, retrieved from simulations with S-CLAY1 and modified Cam clay.

From the modeling of Excavation 1 it is apparent that HS Small with stiffness parameters procured using method 1 is best representing the general behavior of the soil, in terms of how deformations develop over depth. The approach in which the small strain response is approximated according to the general relation between unloading shear modulus, G_{ur}^{ref}, and the initial shear modulus, or shear modulus at small strains, G_0^{ref}, best predicts the shape of the inclinometer curve, while the approach using empirical equations seems to make a less substantial over-estimation of the largest deformation, even though the shape of the curve show larger deviation from measurements over depth. When it comes to predicting the magnitude of the largest horizontal deformations, S-CLAY1 and modified Cam clay modeled with stiffness parameters from method 1, seem to show the most reasonable results.

7.2 Horizontal displacements - Excavation 2 – section B

For the analysis of Excavation 2, the most interesting combinations in Excavation 1 – section A, being HS Small (both approximate and empirical approaches) and S-CLAY1, with stiffness parameters from method 1, were chosen for the simulations. Hardening Soil and modified Cam clay were also included, since a comparison with the two helps determining the importance of small strain stiffness and anisotropy when modeling the problem. See table 7.2. The corresponding displacement curves for Hardening Soil and HS Small are shown in figure 7.3, while S-CLAY1 and modified Cam clay have been displayed in figure 7.4.

Simulations		Stiffness parameters	
Excavation 2 - section B		Method 1	Method 2
Hardening Soil		✓	-
HS Small	Approximate	✓	-
	Empirical	✓	-
S-CLAY 1		✓	-
MCC		✓	-

Table 7.2. Combinations of soil model and stiffness used in the simulations on Excavation 2.

As was anticipated after the evaluation of the results from excavation 1 – section A, the Hardening Soil model managed to predict the shape of the inclinometer curve in a fairly satisfactory manner. The size of the deformation was, however, significantly over-estimated throughout the whole soil profile. The three simulations with HS Small, on the contrary, all show good correlation to the measured deformations, with the approximate approach, and empirical approach A, performing particularly well. This substantiates the importance of small strain stiffness in the two analyzed problems. As for S-CLAY1 and modified Cam clay, the simulated deformations can be seen in figure 7.4.

S-CLAY1 manages to predict the magnitude of the largest deformations in excavation 2 – section B, in an excellent way. The figure also shows that there are significant differences between S-CLAY1 and modified Cam clay, and since the two models

have identical stress-strain response in the elastic region, this shows that the stress state reaches the elastic envelope of S-CLAY1, resulting in plastic deformations in the upper part of the soil profile. The difference in result produced by the two models can be attributed to the modeling of anisotropy, included in S-CLAY1.

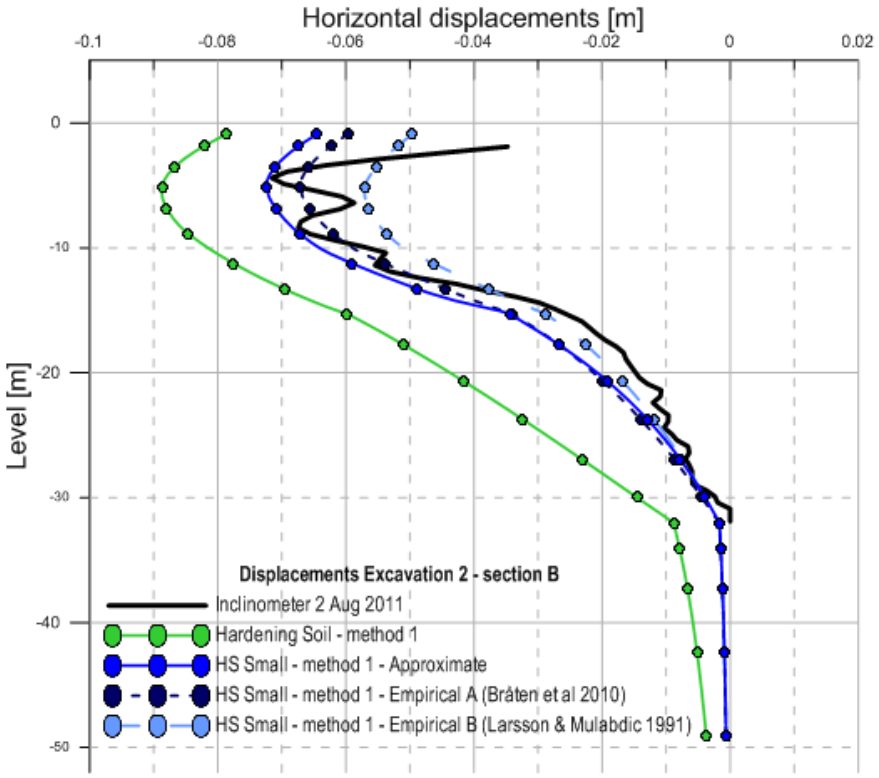

Figure 7.3. Results from the analysis of Excavation 2 – section B, performed with HS Small and Hardening Soil, with stiffness parameters procured using method 1.

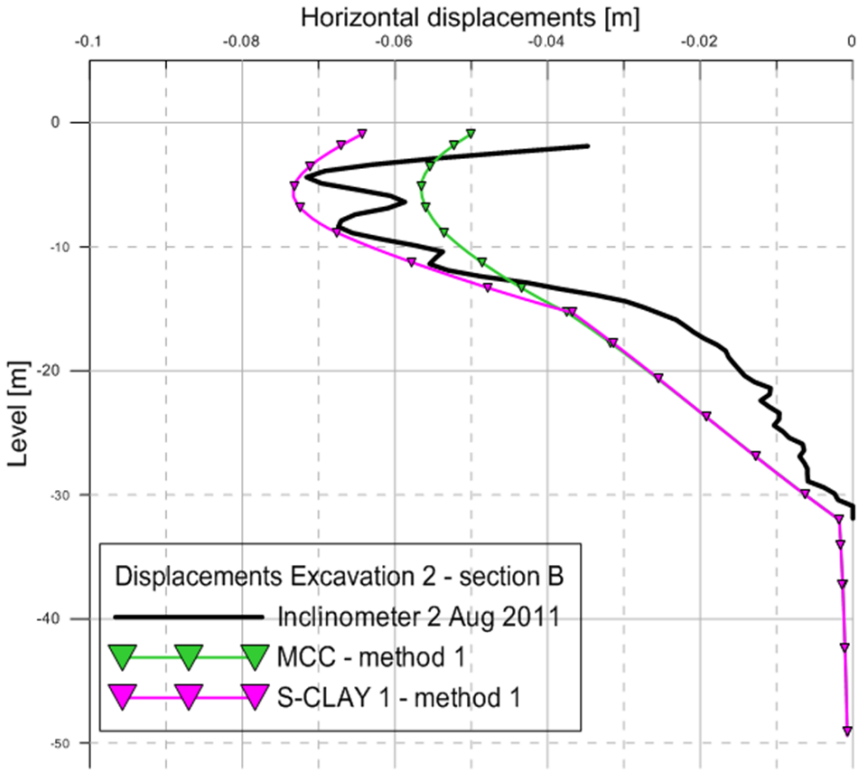

Figure 7.4. Results from the analysis of Excavation 2 – section B, performed with S-CLAY1 and modified Cam clay, with stiffness parameters procured using method 1.

In figures 7.5 and 7.6, the anticipated slip surfaces for the two excavations are shown, along with safety factors, calculated using Geo Slope. The bottoms of the two shear zones are located at levels -8.6 meters and -9.0 meters respectively, for excavation 1 and 2. This reflects the results from S-CLAY1 fairly well, since it too indicates that plastic deformations in the soil are most likely to occur above the level -10 meters.

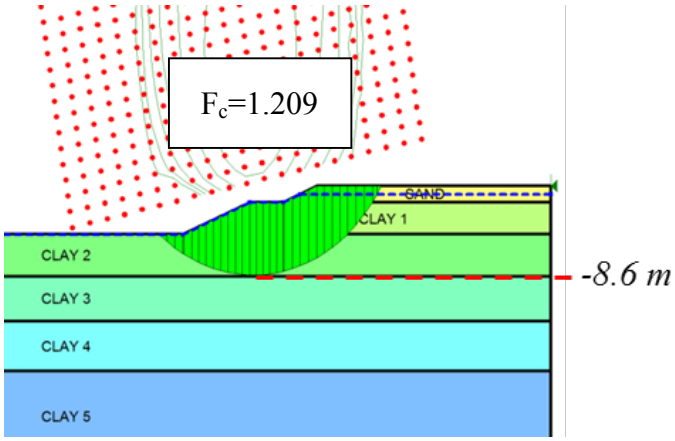

Figure 7.5. Anticipated critical slip surface for the southern slope of excavation 1 – section A, calculated with Geo Slope.

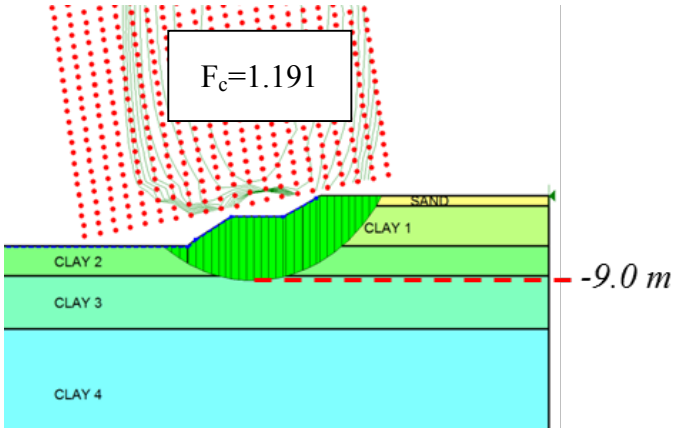

Figure 7.6. Anticipated critical slip surface for the eastern slope of excavation 2 – section B, calculated with Geo Slope.

7.3 Surface measurements

By observing the diagrams in the bottom left and right corner of figure 7.7, showing the simulated surface displacement for Excavation 1 and 2 respectively, at the location of the pegs, it can be seen that none of the soil models manage to represent the measured ground movement at the surface in a satisfactory manner. Around Excavation 1, the deformations are vastly under-estimated, while for excavation two, all models predict about twice the magnitude of deformations in all points except for at control peg 11, in which the simulated results predict half the size of measured displacements.

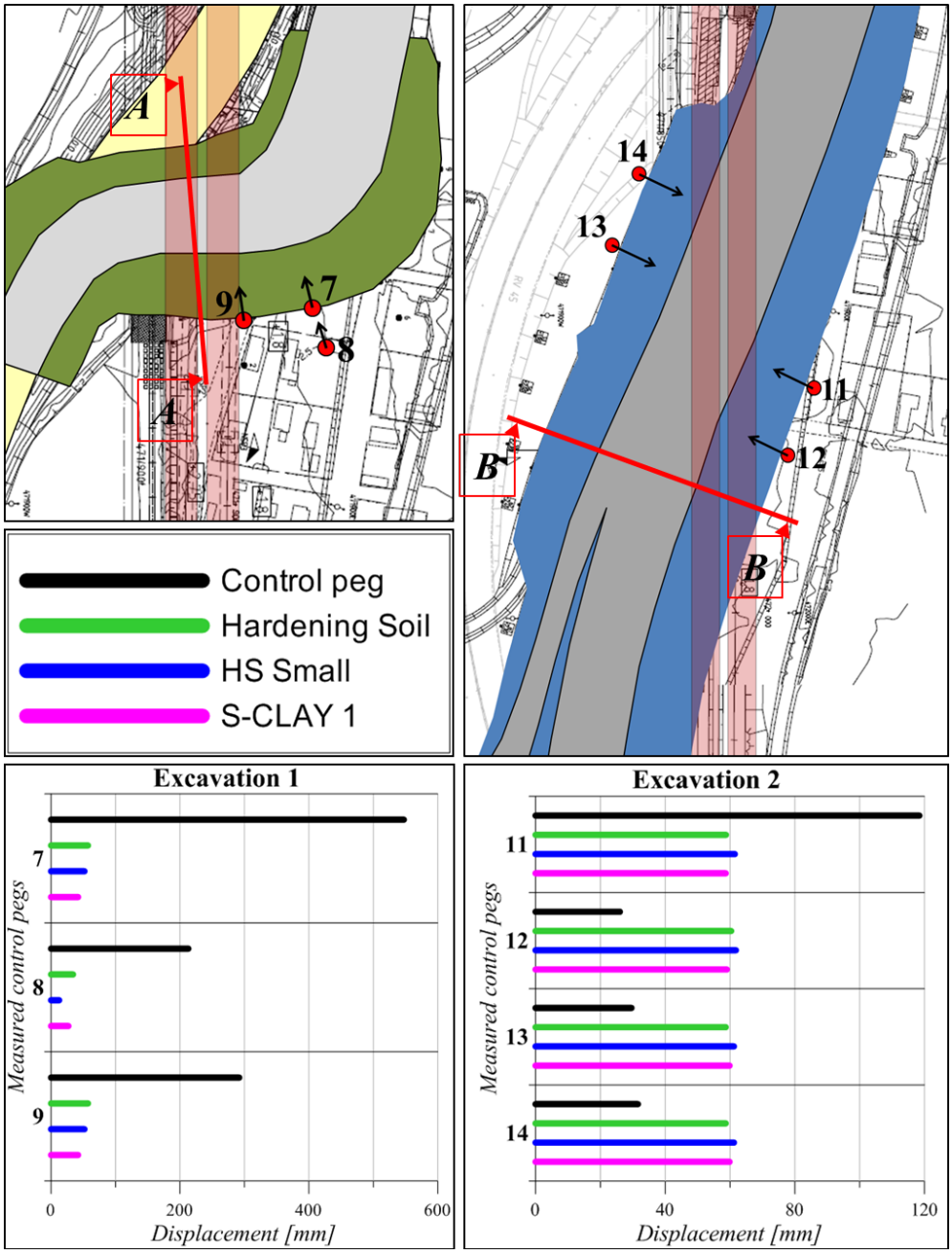

Figure 7.7. Comparison between measured and simulated surface displacements in the vicinity of the two excavations.

7.4 Comparison of calculated and simulated stresses

In order to confirm that the models created for the two excavations provided a reasonable representation of the conditions in the soil, a control procedure was performed, in which the anticipated effective stresses, in-situ and posterior to unloading, were calculated, based on soil density and ground water level. The stresses posterior to the unloading of the soil were approximated using the 2:1-method, for which an account is given in *Sällfors* (2009). See equation 7.1 as well as figure 7.8. The calculated stresses were then used as a reference against those generated in Plaxis 2D. In figure 7.9, a comparison is made between the calculated stresses and the stresses generated in Plaxis 2D. The curves correspond to the center of each excavation.

$$\Delta\sigma = \frac{bq}{b+z} = \frac{b\sum_{m=1}^{m=6}\gamma}{b+z} \qquad (7.1)$$

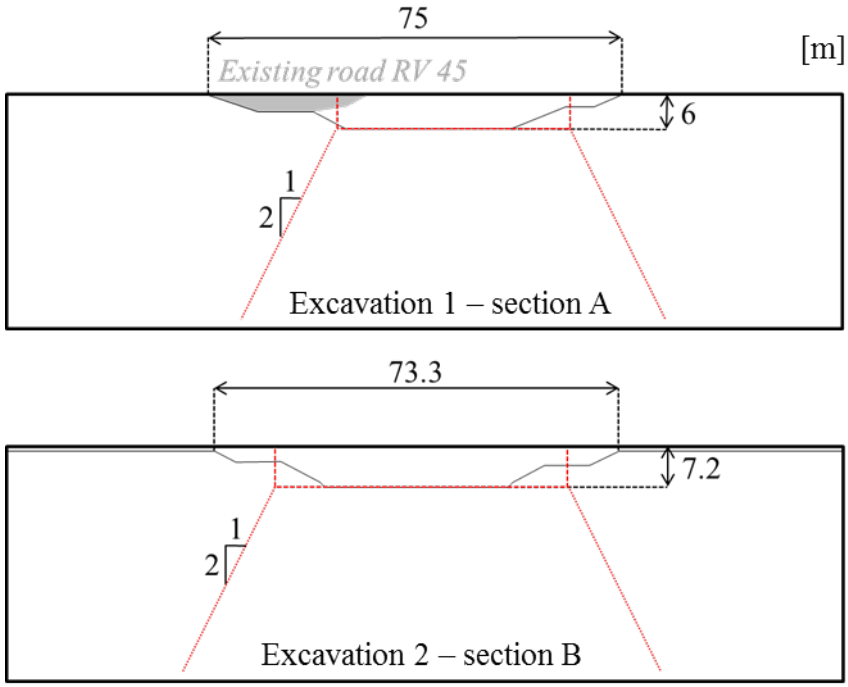

Figure 7.8. Conceptual figure of the two excavations, showing the principle for how negative stress increments were accounted for in the reference calculations.

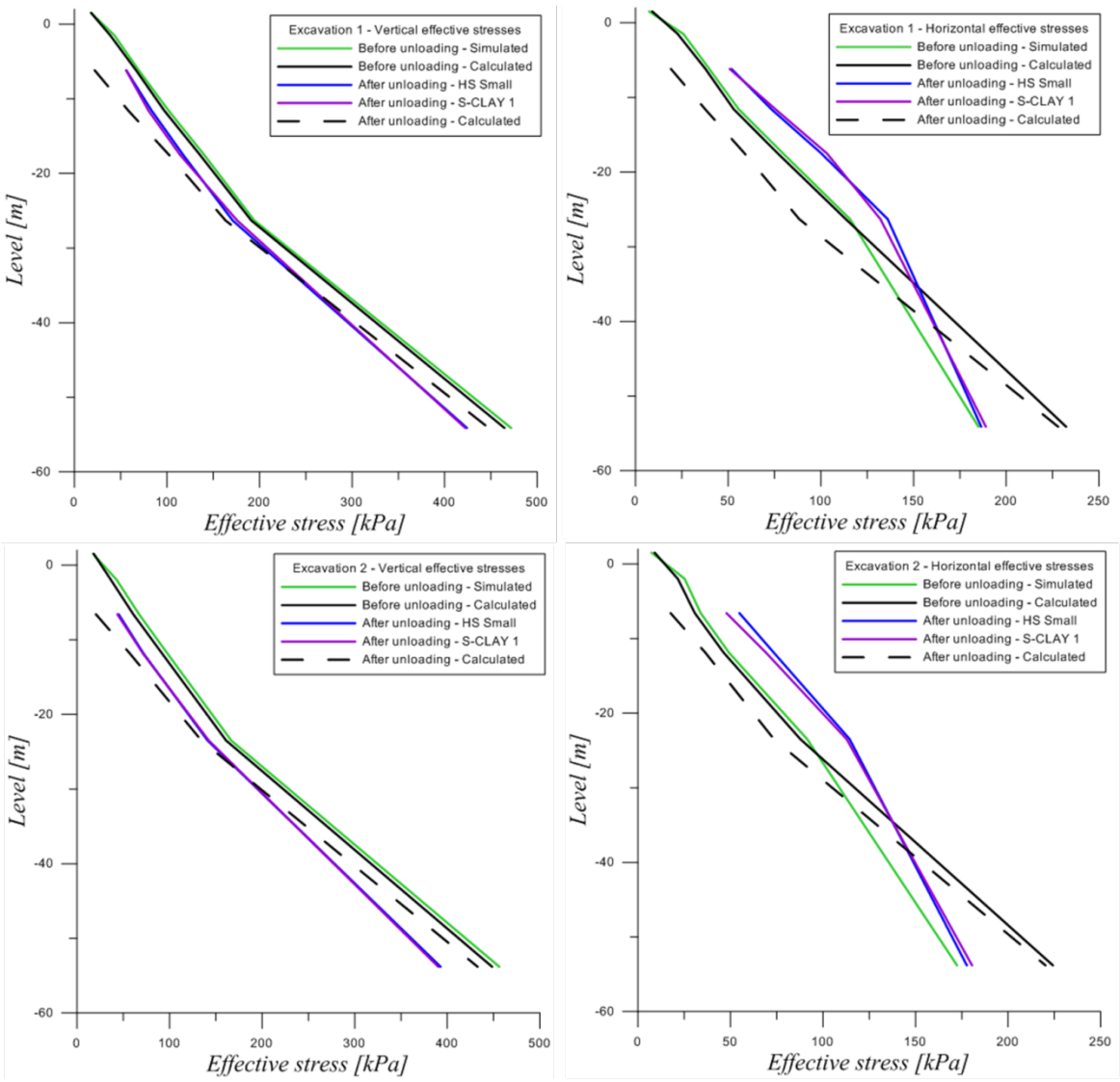

Figure 7.9. Diagrams of calculated and simulated stresses. Top left: Vertical effective stresses for Excavation 1 – section A, before and after unloading. Top right: Horizontal, Excavation 1 –section A. Bottom left: Vertical, Excavation 2 – section B. Bottom right: Horizontal, Excavation 2 – section B.

The diagrams in figure 7.9 show that the calculated initial effective stresses correspond well to the simulated in both excavations. The simulated horizontal stresses posterior to the unloading of the soil, however, follows a rather different pattern than the calculated. In the simulation, the horizontal effective stresses increase as the vertical load on the soil is reduced, while the calculated horizontal effective stresses decrease. However, in the manual calculations, horizontal stresses were determined in relation to the vertical, using K_0-distribution. The vertical unloading, resulting from the removal of soil, thus lead to horizontal effective stress increments, which were proportional to the vertical, and therefore decreasing. In the Plaxis simulations, on the other hand, the deformations developing in the slopes of the excavations resulted in horizontal compression of the excavation bottom, instead generating positive increments of horizontal stresses. See figure 7.10.

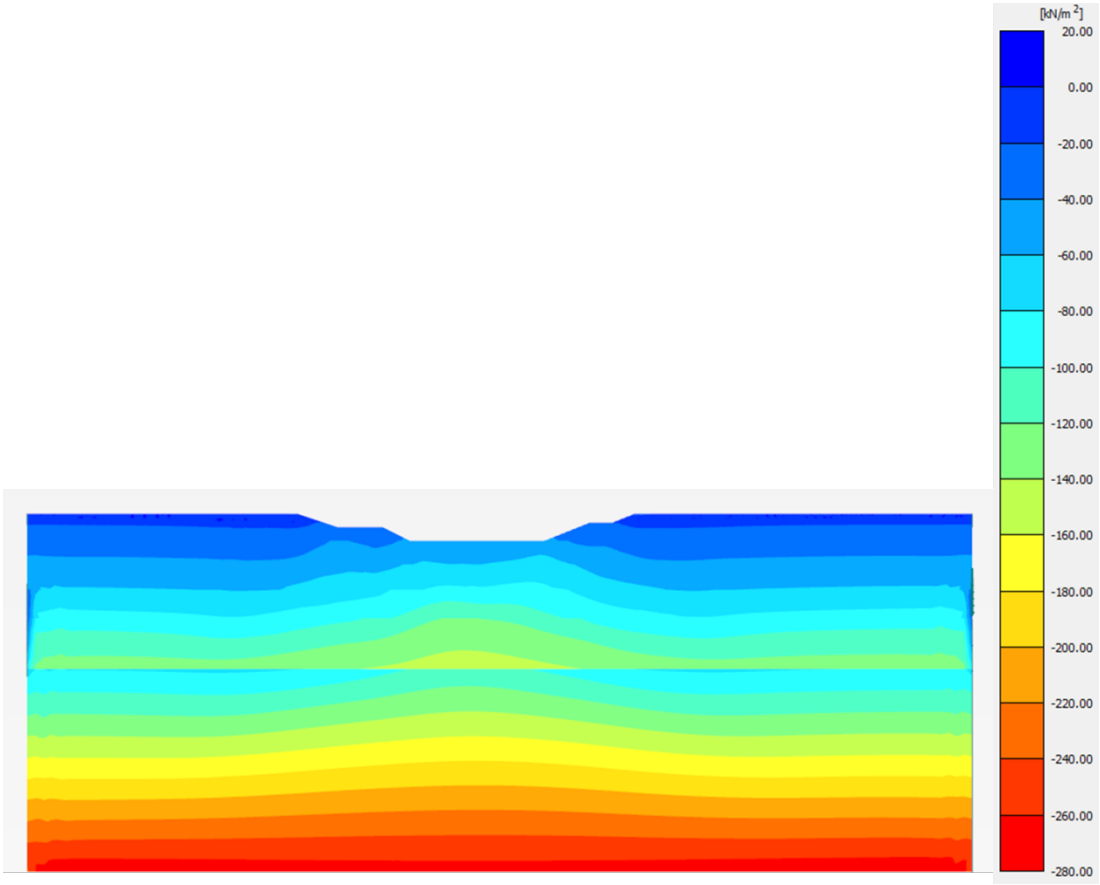

Figure 7.10. Example of how horizontal stresses increases when the soil is unloaded. (Cartesian effective stresses, $\boldsymbol{\sigma'_{xx}}$ procured from HS Small).

8 CREDIBILITY ASSESSMENT

8.1 Stress paths and strain characteristics

As can be seen in figures 8.1 and 8.2, a number of stress points have been selected in each of the two meshes, the purpose of which being to visualize the stress development throughout the modeled sections. The points represent the lateral center of the excavation bottom, two levels of the soil profile along the length of the inclinometer as well as the part of the southern (for Excavation 1 – section A) and eastern (for Excavation 2 – section B) slopes where the largest shear strains occur in the simulations.

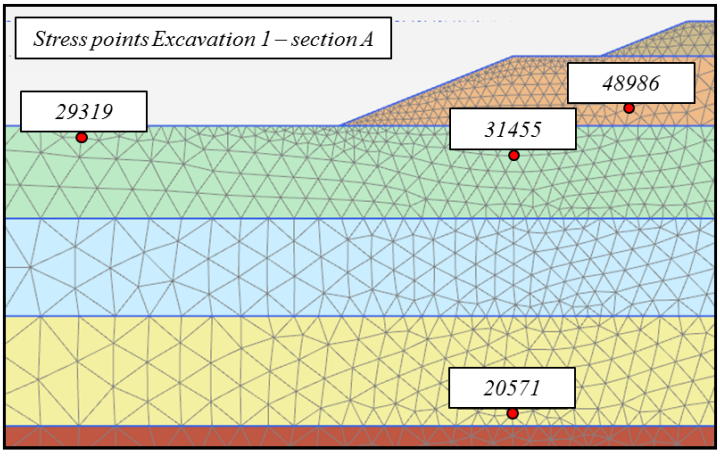

Figure 8.1. Excavation 1 – section A, showing stress points for the plotted stress paths.

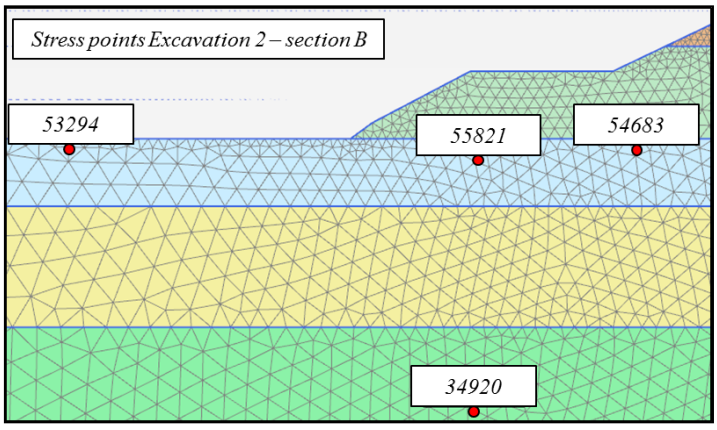

Figure 8.2. Excavation 2 – section B, showing stress points for the plotted stress paths.

In figure 8.3, the corresponding stress paths for Excavation 1 – section A, resulting from the unloading of the soil, have been plotted for HS Small (red dashed) and S-CLAY1 (blue). The diagrams are presented in clockwise order, corresponding to the position of each stress point in the figures above. The same has been done for Excavation 2 – section B, in figure 8.4. Also displayed in the diagrams are Mohr-Coulombs failure line and the stress path for K_0-compression, included for comparison with the stress paths from HS Small.

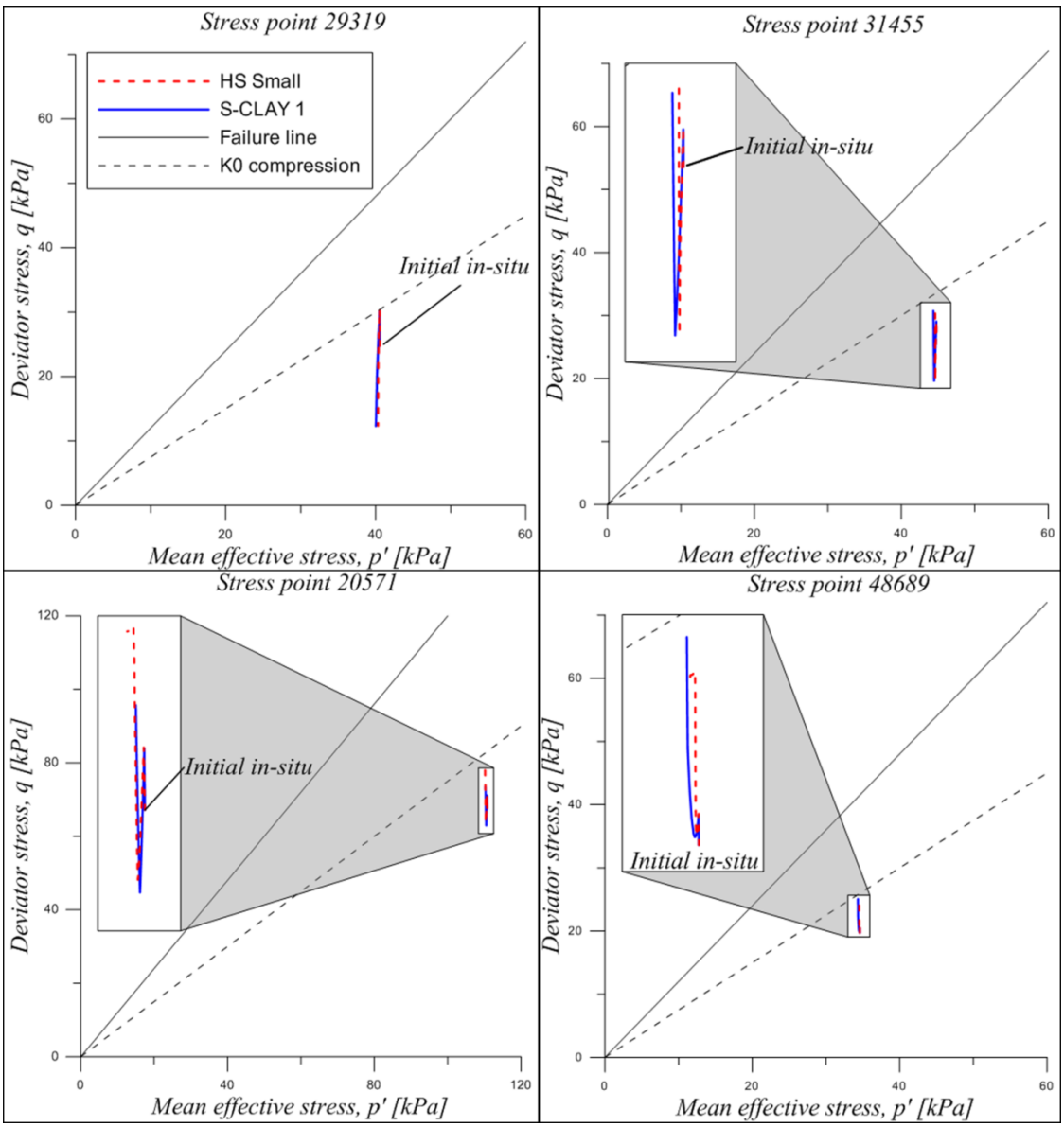

Figure 8.3. Stress paths for selected points in excavation 1 – section A.

The graphs indicate, as was assumed by *Ismail and Teshome* (2011), that for the Hardening Soil model and HS Small the reference stiffness of major interest in all of the selected stress points is the unloading modulus, E_{ur}; deviatoric stresses are lower than K_0-distribution, indicating that the deviatoric yield line is not reached during unloading, except for in stress point 54683, which represents the area with the largest shear strains in Excavation 2 – section B. In this point, it seems that the stress path

reaches the yield cap for isotropic compression, after which it follows the caps curvature until it reaches the deviatoric yield line. In general, however, the plotted stress paths show that for Hardening Soil and HS Small, E_{50} and E_{oed} is of minor relevance in this problem, meaning that the values on E50 which are exceeding 2Eoed, regarding which a comment was made in Chapter 4.5.2, may not have caused any major issues in the simulations.

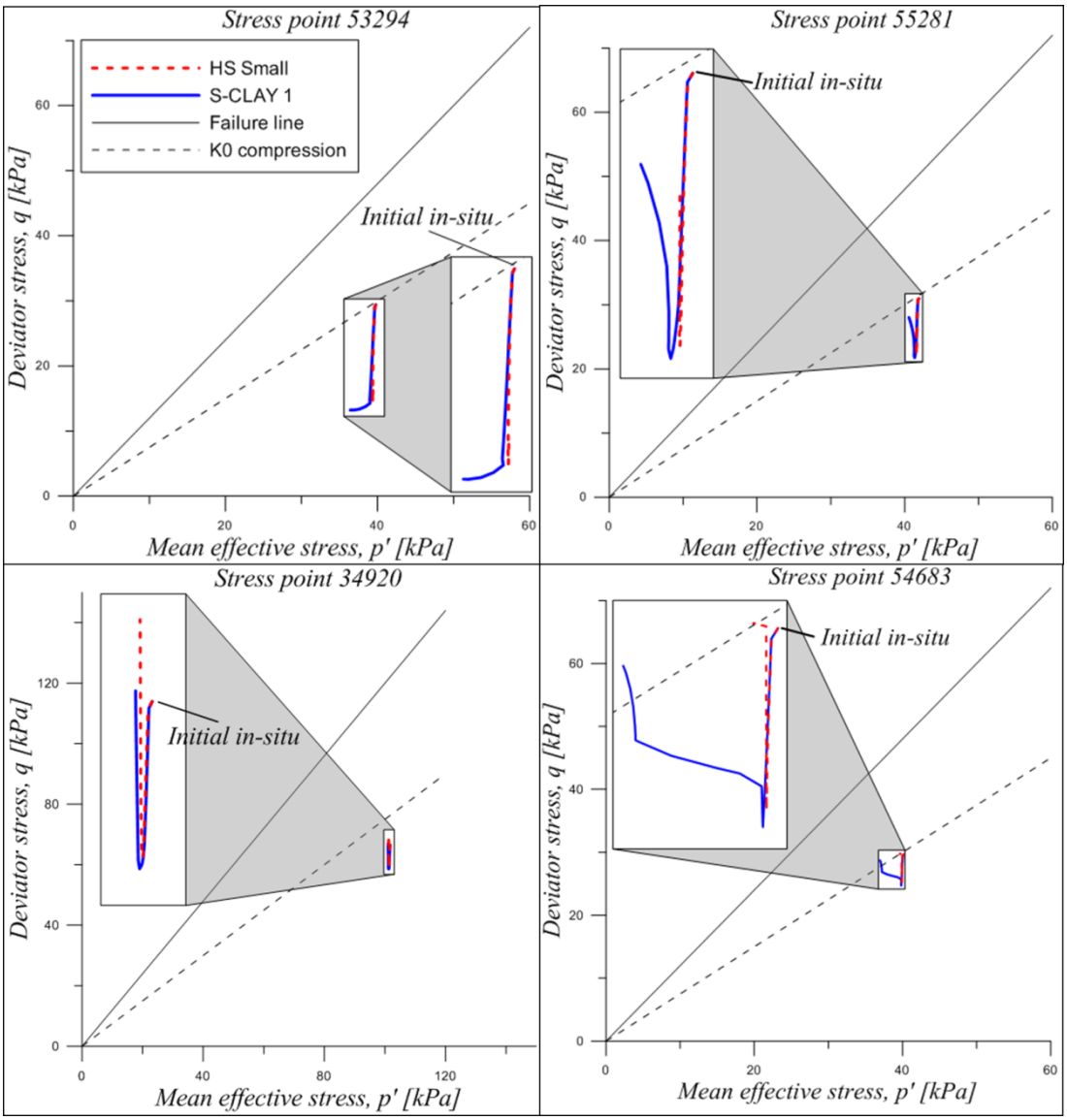

Figure 8.4. Stress paths for selected points in excavation 2 – section B.

Regarding S-CLAY1, some of the stress paths show noticeable differences compared to those produced using HS Small, particularly in Excavation 2 – section B, even though all have been retrieved from the same unloading problem. This effect can most likely be attributed to the models´ differences in stress:strain response and yield criterion throughout the modeled section. Stress paths plotted from simulations with S-CLAY1, expressed as mean effective- and deviatoric stress, are not necessarily undisputable indicators regarding the occurrence of plastic strains in a certain element, since the anisotropic properties the model assumes for the soil results in a

yield surface that is not necessarily centered around the p'-axis, in principal effective stress space. For this reason, plastic strains might occur in a point which does not represent the largest deviatoric stress. For Excavation 2 – section B, however, changes in characteristics of the plotted stress paths seem to occur in the same layers as the plastic deformations, as has been shown below. These changes may be an indication that the yield surface of the rotated ellipse is reached, resulting in strains changing direction to satisfy the flow rule for plastic yielding, incorporated in the model.

In order to find whether the simulations with S-CLAY1 resulted in plastic strains throughout the soil profile, and thus consequently, if the model's tools for anisotropy was utilized, two approaches were used. The first one was comparing S-CLAY1, taking fabric anisotropy during plastic straining into account, with the modified Cam Clay model. The differences between the displacement curves for the two models, displayed in figure 7.4, chapter 7.2, indicate that some of the plotted stress paths are most likely reaching the envelope of the rotated yield locus of S-CLAY1. In case both models would have predicted elastic response throughout the whole soil profile, the displacement curves would have been identical, due to the formulation of elastic stress: strain response in equations 3.30 and 3.31. This was the case for Excavation 1 – section A. In Excavation 2 – section B, however, there was a significant difference between the predicted horizontal deformations in the upper part of the soil profile, generated using S-CLAY1 and modified Cam clay. This is a clear indication that the simulation predicts plastic strains in this portion of the modeled section. In order to find where in the soil profile these plastic deformations occurred, changes in the rotation parameter α were plotted, since rotation of the yield locus requires plastic strains. The distribution of α in the clay layers, for the four calculation phases, can be seen in figures 8.5 and 8.6.

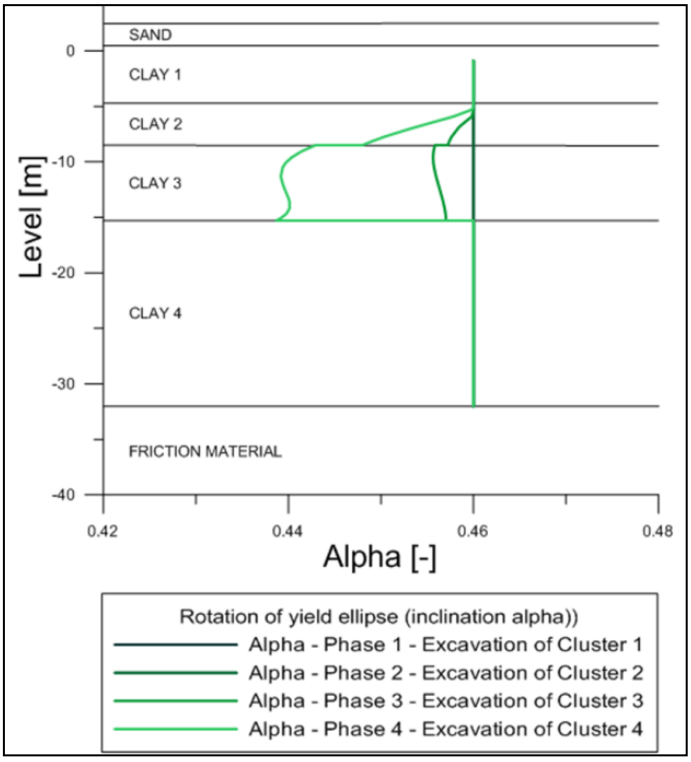

Figure 8.5. The value on α along the length of the inclinometer, by the end of each excavation stage.

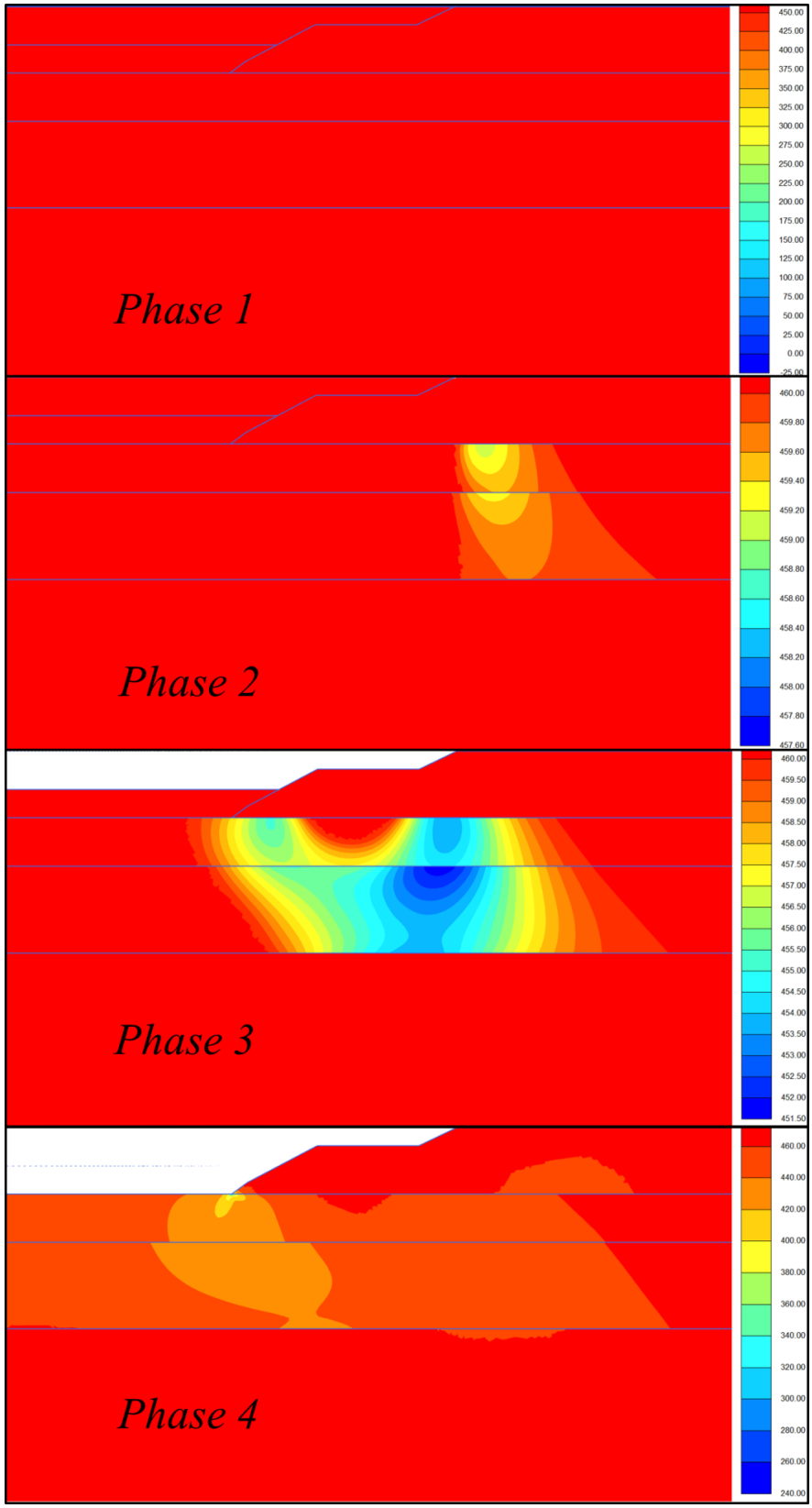

Figure 8.6. Distribution of the rotation parameter α in the clay layers, by the end of each calculation phase, and analogously, the regions of the soil profile where plastic strains occur in the simulation with S-CLAY1.

Observing figure 8.6, it can be seen that in the first phase, which represents the surface unloading at the site, no plastic strains occur, while in the following two phases, plastic deformations are taking place in clay layers 2 and 3. The reason why these two layers are the first to reach a state of plasticity is likely because they have been defined as being close to normal consolidated (OCR 1.02 and 1.01), and that the initial in-situ stresses for that reason represent a state closer to the envelope of the yield locus. In the fourth excavation stage, phase 4, the plastic strains continue to develop into clay layers 1 and 4, which have OCR of 1.39 and 1.19 respectively. Figure 8.5 shows how the values on α change after each calculation phase, over the length of the inclinometer.

8.2 Parameter sensitivity analysis

Due to the uncertainties associated with the procurement of some of the parameters in this investigation, a number of sensitivity analyses have been performed.

The evaluation of the compression- and swelling indices (C_c and C_s respectively), performed in this report, may lack somewhat in precision. Ideally, an oedometer test with stepwise load increments, accompanied by unloading cycles, would have been used for the derivation of the two parameters. However, since only standard CRS tests were available, C_s was specified using the first part of the CRS curve, for stresses lower than pre-consolidation pressure, which does not necessarily represent a true unloading-reloading curve.

Adding to the uncertainty is the use of water content prior, rather than posterior, to the CRS test. The stress: void ratio curve is, according to *Craig* (2004), preferably created using backward increments, starting from the water content at the end of the test. However, for one of the boreholes, FB41, both prior and posterior water content was documented in the CRS test, and by comparing C_c and C_s calculated with each of these water content values, it was noted that the value on the two parameters deviated by an average 5% between the two approaches.

The process of adapting trend lines to the plotted *stress:void ratio* curves also involves some uncertainty, since the inclination of the adapted curves are dependent on the stress intervals for which the curves are created. This has been exemplified in figure 8.7, which shows graphic representations of the differences between different values of C_c and C_s. The figures show that for a small stress interval, it is difficult to tell the lines apart from each other, and that a deviation of 5% from the true curve is not easily recognized visually.

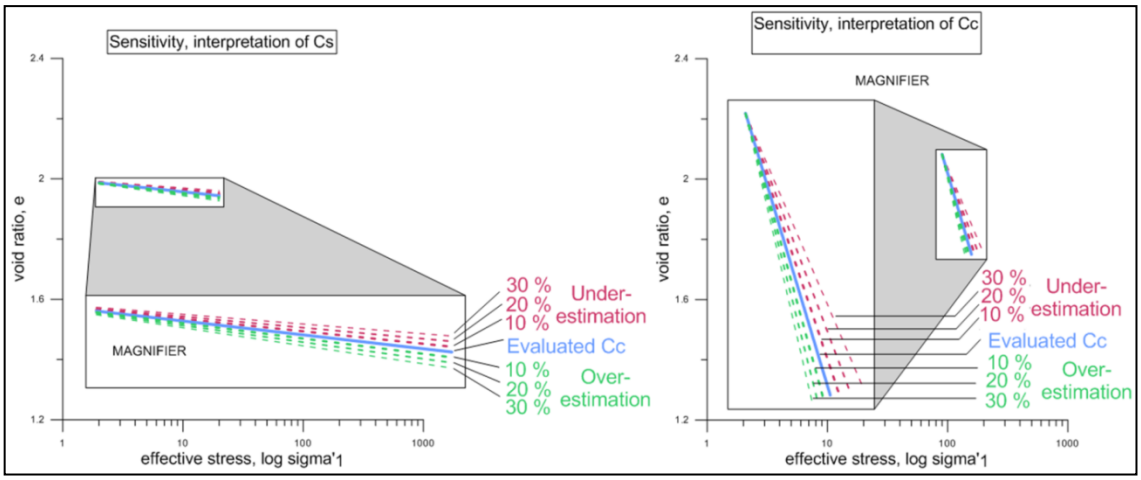

Figure 8.7. Visual representation of the difference in inclination for the semi-logarithmic curves in the stress:void ratio diagrams, resulting from deviating values on C_C and C_S.

In unfortunate cases these uncertainties may add up and cause the evaluated compression- and swelling indices to deviate from the true ones. In this report, however, each of the two parameters was first evaluated for each sample, after which the data was plotted against elevation in the profile. The values chosen as input for each soil layer were then retrieved from trend lines fitted against these points (the principle shown in figure 8.8). Since it is likely that liabilities in the correctness of these values would represent both over- and under-estimations, some of the errors might have evened out in the process of fitting the trend line.

To investigate the effect of variations, a sensitivity check was performed on the two parameters C_c and C_s, in which each of the parameters were decreased and increased, one by one, by 10%, after which additional simulations were performed, on Excavation 2 – section B.

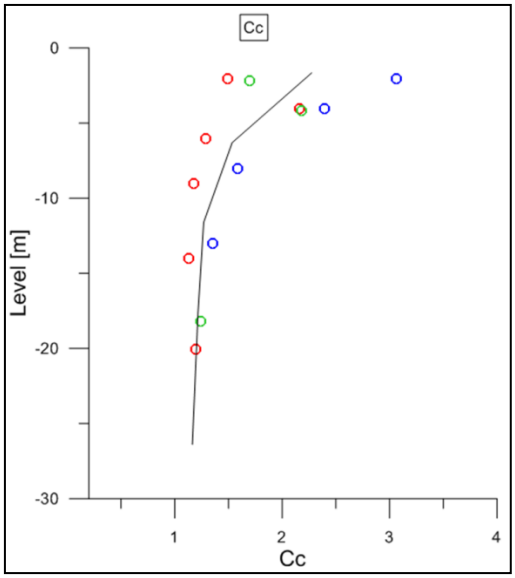

Figure 8.8. Trend line fitted against values on C_C, plotted against level.

The same sensitivity procedure was performed on the parameters G_0^{ref}, $\gamma_{0.7}$ and E_{50}^{ref}, on excavation 2 – section B. The result from the analysis is expressed in terms of average deviation from the initial deformation curves, achieved with the original input parameters, and is shown in table 8.1.

Sensitivity analysis - Average deviation [%] from original deformation curve										
Soil model	C_S		C_C		G_0^{ref}		γ_{07}		E_{50}^{ref}	
	-10%	+10%	-10%	+10%	-10%	+10%	-10%	+10%	-	+10%
S-CLAY 1	- 10.2	9.6	- 0.3	0.2	NA	NA	NA	NA	NA	NA
HS Small (Approximated small-strain response)	- 15.8	16.8	- 0.0	0.5	14.3	- 12.5	6.7	- 5.9	NA	- 0.1
HS Small (Empirical A)	- 1.4	1.1	- 0.5	0.6	11.5	- 10.7	5.9	- 5.3	NA	1.1

Table 8.1. Summarization of the parameter sensitivity analysis.

As can be seen in table 8.1, as well as in figures 8.10a and 8.11a, variations in swelling index, C_S, have a greater impact on the simulation results from HS Small with the approximated small strain response, than on those retrieved using Empirical approach A, or on those from S-CLAY1, shown in figure 8.9a. In Empirical approach A, where the small strain response was specified based on plasticity index, I_P, and undrained shear strength, c_u, a 10% change in C_S does not have as significant an impact on the resulting deformation, again see figure 8.11a. Regarding S-CLAY1, the swelling index affects the unloading-reloading stiffness κ, and changes in the parameter have a large enough effect on the simulation outcome to motivate caution and a critical approach towards the data evaluation process.

Changes in the parameter C_C do not have any significant effect on the simulation results with any of the combinations of models and soil stiffness investigated. This is likely because, as can be seen in the plotted stress paths, virgin compression is not an important mechanisms in this problem. Also see figures 8.9b, 8.10b and 8.11b.

The magnitude of the reference shear modulus at very small strains, G_0^{ref}, has a large effect on the deformation curves simulated with HS Small, which can be seen in figures 8.10c and 8.11c. This is the case regardless of the approach chosen for determining G_0^{ref} and $\gamma_{0.7}$, of which the latter proves to also be a parameter of large significance to the magnitude of the predicted deformations. The deformation curves with variations in $\gamma_{0.7}$ can be seen in figures 8.10d and 8.11d.

The results observed in simulations with an increased modulus E_{50}^{ref}, shown in figures 8.10e and 8.11e, are somewhat unexpected since the deformations in this case increased, rather than decreased, which might have been suspected.

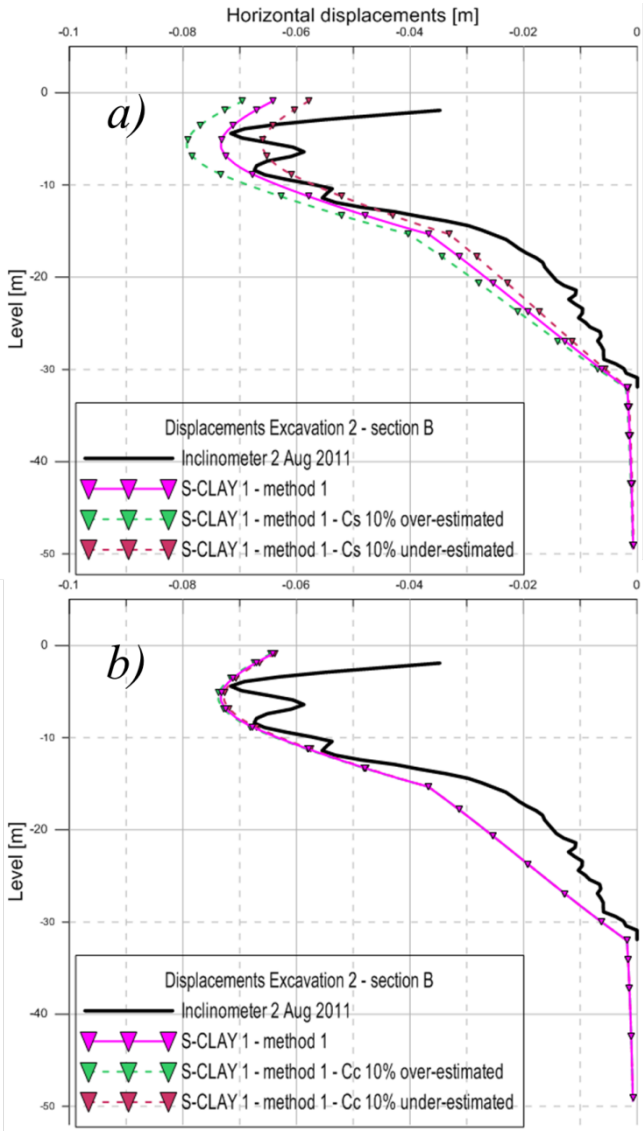

Figure 8.9. Deformation curves from the sensitivity analysis, performed on Excavation 2 - section B, with S-CLAY1.The parameters Cs and Cc increased and decreased respectively, by 10%. ***a)*** *Cs* ***b)*** *Cc*

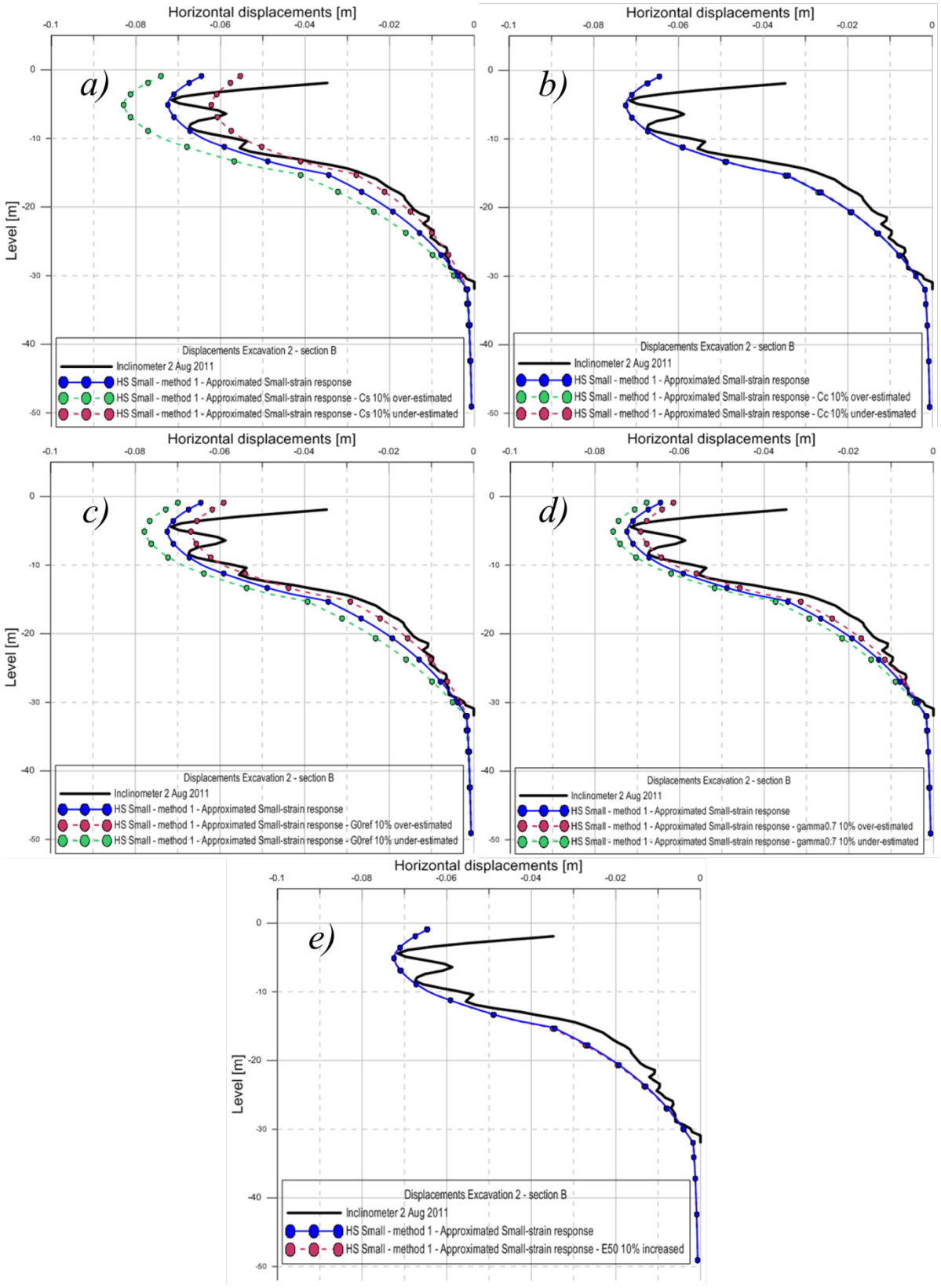

*Figure 8.10. Deformation curves from the sensitivity analysis, performed on Excavation 2 - section B, with HS Small – method 1, and with **approximated** small strain stiffness parameters. Each parameter increased and decreased respectively, by 10%, except for E50, which was only increased, due to model restrictions.* ***a)*** C_S ***b)*** C_C ***c)*** G_0^{ref} ***d)*** $\gamma_{0.7}$ ***e)*** E_{50}^{ref}

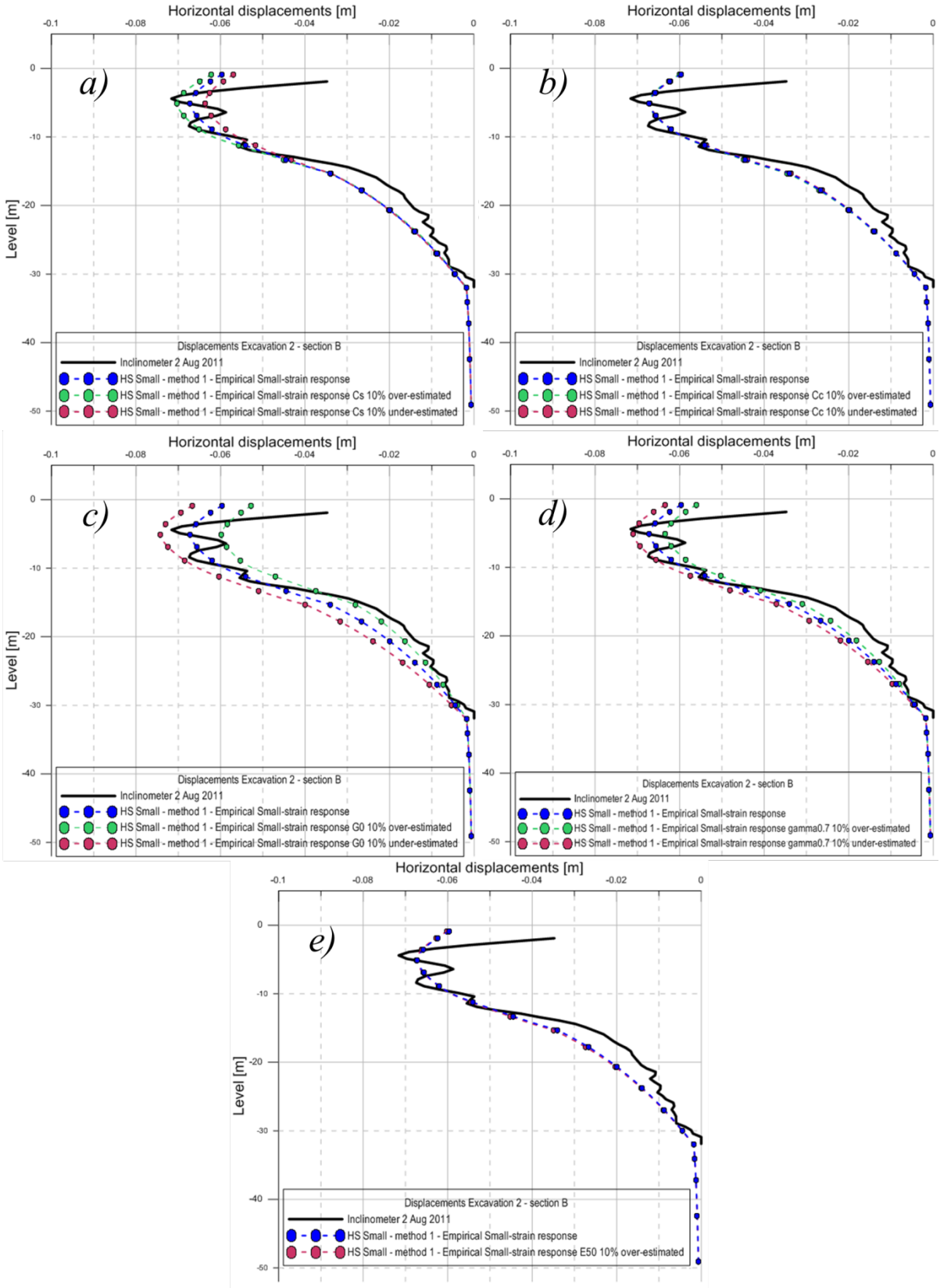

*Figure 8.11. Deformation curves from the sensitivity analysis, performed on Excavation 2 - section B, with HS Small – method 1, and with small strain stiffness parameters specified using the **Empirical approach A**. Each parameter increased and decreased respectively, by 10%, except for E50, which was only increased, due to model restrictions. **a)** C_S **b)** C_C **c)** G_0^{ref} **d)** $\gamma_{0.7}$ **e)** E_{50}^{ref}*

Since several approaches were used for specifying the small strain stiffness parameters of the soil, in the simulations with HS Small, and since all three rendered very similar deformation curves for Excavation 2 – section B, a check was performed regarding which stiffness the model utilizes at different amplitudes of strain. A visualization of this, in which the Approximate approach has been compared to Empirical A, can be seen in figure 8.12. Note that, in the figure, the cut-off γ_c is not included.

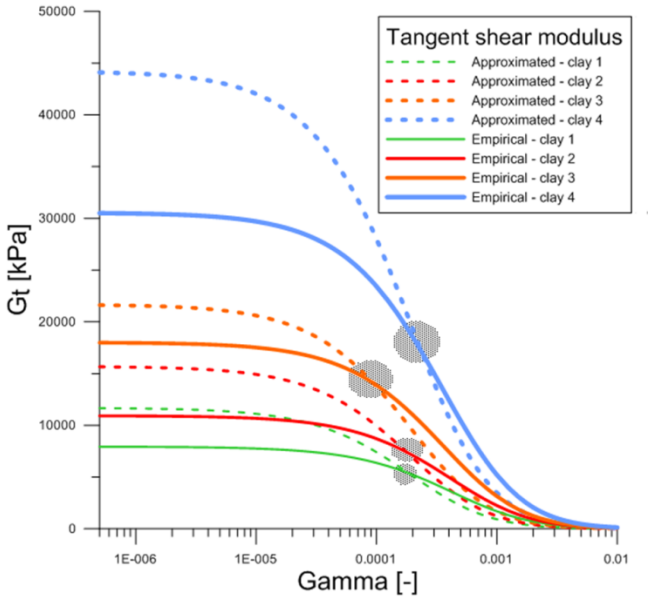

Figure 8.12. Shear modulus at different amplitudes of strain, for the two approaches used in the determination of G_0^{ref} *and* $\gamma_{0.7}$.

9 DISCUSSION

Modeling

As is often the case when attempts are made to represent reality with models, the numerical analyses performed, as part of the investigation for this MSc-thesis, involve a significant amount of simplifications and assumptions. To start with, the modeling of the problem in two dimensions excludes the effects of topographic variations, as well as the impact from the bridge foundation from the analyses, the latter of which has proven to have a noticeable impact on the development of deformations. It may also be questioned whether Excavation 1 – section A, can be sufficiently modeled in two dimensions, due to the S-shaped geometry of the preliminary road, when observed in plane view.

The representations of the two soil profiles are, even though divided into several layers, based on average values retrieved from three bore holes positioned an approximate 50 meters apart, and can for this reason not be regarded as precise representations of any given section in the two excavations. Furthermore, details from the contracting process are left out altogether from the investigation. It is likely that the partitioning of simulation stages in this analysis does not represent the true order in which the two excavations were realized in the contracting process, and that the final geometries defined in the models do not fully correspond to the true shapes of the investigated cross-sections.

Further uncertainties are associated with the positions of the inclinometers, both of which are located in close proximity to the bridge foundations. It is uncertain if the foundations' suppressive effect is limited to the soil closest to the ground surface, and thus, to which depth the displacements along the length of the inclinometers have been held back.

The finite element analysis did not involve any convergence check, as to ensure that the models are not mesh dependent, due to an inadequate number of elements. Ideally, the meshes would have been refined until no differences could be observed between two subsequent simulations. This procedure would, however, have resulted in extensive and cumbersome analyses, and was therefore excluded from the investigation.

Stiffness evaluation methods

There are uncertainties associated with the two methods used for defining stiffness parameters for each soil layer. In Method 1, the main issue is the lack of true unloading and reloading curves in the CRS tests, and that the water content after each test was not submitted in the test results. This necessitated a compromise, resulting in a swelling index, C_s, which was possibly higher than that, which would have been

retrieved from a true unloading reloading sequence, resulting in a softer simulated response of the soil. However, since the swelling indices defined in this report were specified as tangents to the initial loading curve, while a conventional evaluation process of the parameter utilizes the secant of an unloading-reloading curve, it may be that some of the discrepancy between the two procedures was eradicated in the evaluation process. Regarding water content, the most proper procedure is to use the water content after the CRS test, and back-calculate to the initial void ratio. If the calculated value would then conform to the measured water content before the test, the incremental values of the void ratio would be more trustworthy, as a function of strains, obtained from the CRS-tests. To receive as trustworthy results as possible, it is therefore necessary to have both the water content before and after the consolidation.

When it comes to Method 2, the results in this report indicate that the true deformation behavior of the soil is not sufficiently represented by the chosen parameters M_L, M_0 and $5M_0$, since all simulations resulted in under-estimations of the actual deformations. It is possible that the assumptions made in the method involves too much rationalization when combined with the choices of strength parameters made in this report, i.e. a critical state friction angle of 30 degrees for clay, and thus, does not enable a realistic prediction of the actual soil behavior. There are important differences in the boundary conditions of a soil sample tested in a triaxial apparatus compared to one compressed in a CRS test, and it may be that the effect of horizontal constraints in the CRS test are too great even at fairly low Poisson ratios, and that the radial stresses for this reason suppresses the axial deformation of the sample, leading to an over-estimation of the reference moduli. Better correlation could have been achieved if other parameters were to be adjusted based on soil test simulations. This was, however, not included in this investigation.

The Hardening Soil model

The simulations with Hardening Soil indicate that, in an unloading problem of this nature, the horizontal deformation curves are not easily captured with the model. It should, however, be kept in mind that the two methods used for deriving stiffness parameters are not the optimal procedures, as defined in the formulation of the model. According to this the reference moduli should be extracted directly from triaxial tests. Since no such laboratory data was available for this analysis, it is difficult to determine the appropriateness of Hardening Soil, as a model, in an analysis of a problem of this type. It does, however, seem that the model should not ideally be combined with either of the Methods 1 or 2, utilized in this report, in a project with high demands regarding the precision of predicted horizontal deformations resulting from the unloading of a soil mass, since the resulting deformation curves, in this case, were found to be either over- or under-estimated. In addition to errors associated with less-than-optimal input parameters, the models inability to represent small-strain behavior of the soil is likely to have contributed to the large differences between the deformation curves predicted by the model, and the measured displacements.

HS Small

The sensitivity analysis shows that for HS Small, it is of great importance to find the appropriate small strain response of the soil. The first approach, where G_0^{ref} and $\gamma_{0.7}$ were approximated as averages of the intervals in which each of the parameters can be expected to be represented, is most prone to errors in case the value on C_s is incorrect. This is likely due to the fixed relation between E_{ur}^{ref} and G_0^{ref}, assumed in the approximate approach, due to the lack of laboratory investigations regarding the

dynamic modulus for the clay at the site; the swelling index governs the value on E_{ur}^{ref}, and thus also the value on G_0^{ref}. In the empirical approaches the small strain response is independent of C_s, which is why the result is not significantly affected by changes in the parameter. Even though the three approaches for determining the small strain stiffness give similar deformation curves, particularly for excavation 2 – section B, it is important to note that the input values on G_0^{ref} and $\gamma_{0.7}$ are not the same between the procedures. The approach in which the small strain response is approximated renders a higher initial stiffness than the empirical ones, as was shown in figure 8.12, but the strain increment required for decay of the initial stiffness is smaller. Subsequently, the small strain stiffness moduli for the two approaches are only equal at certain amplitudes of strain. This implies that the degree to which the simulated deformation curves correlate between the three approaches depend on the strains generated in the model.

S-CLAY1

In this problem, it is evident that the simulation results from S-CLAY1 are essentially more dependent on the unloading parameter, κ, than on λ. The sensitivity analysis showed that variations in C_s, which governs the value on κ, had a noticeable effect on the size of predicted deformations, while changes in C_c, governing λ and μ, did not result in any significant alteration of the predicted deformation curve. This last observation is reassuring, since it gives an indication that the magnitude on the parameter μ, which is not easily evaluated experimentally, is not necessarily crucial for the outcome of a simulation. It may be that since the rotational increment, dα, in this case is small throughout the course of the simulation, indicating that the rotational hardening law is not as important as the law for volumetric hardening, which governs changes in p'_m, and thus the expansion of the yield locus. If the rotation of the ellipse only contributes to a fraction of the generated plastic strains in the model, it is perhaps possible that even a major change in the parameter μ will result in barely observable changes in predicted deformations. Similarly to μ, changes in the stiffness parameter λ does not have any substantial effect on the size of the predicted deformations. This is somewhat contradictory, since a comparison of the deformation curves produced using S-CLAY1 and modified Cam clay, show that plastic strains are generated in the simulations with S-CLAY1. It may be, however, that the plastic strains are relatively small compared to the elastic, and that changes in λ, for this reason, does not significantly affect the total deformations in the soil profile.

Surface displacements

The results from the surface measurement evaluation provide an indication that the models´ are not capable of predicting the soil behavior at the surface, further away from the excavations. However, it needs to be kept in mind that the ground pegs are exposed to interference from activities during the contracting process, and that the models created for the two investigated objects involve significant simplifications, in terms of material composition and topography at the ground surface of the site. In addition, as can be seen figure 7.7, the pegs are not located in the investigated sections of the two excavations. This brings uncertainties regarding the credibility of the comparison, since the soil profile varies between different locations at the site, even if the geometry of the excavations can be regarded as constant over the distances from the investigated sections A and B, to the sections in which the control pegs are located. It is therefore likely that these circumstances would have contributed to

discrepancies between simulations and measurements, regardless of the soil models' potential in representing true soil behavior.

10 CONCLUSIONS & RECOMMENDATIONS

From the simulations performed in this investigation, it can be concluded that fabric anisotropy and soil behavior at very small strains are important phenomena to account for, when it comes to the predictions of horizontal displacements mobilized in, and around, the excavations analyzed in this investigation. Simulations executed with the models HS Small and S-CLAY1 enabled more realistic predictions of measured horizontal soil deformations, than those previously acquired using Hardening Soil and the Mohr Coulomb model. Findings also emphasize the importance of properly specified stiffness parameters, irrespective of soil model used for the numerical analyses. In this regard, stiffness evaluation Method 1, in which soil stiffness parameters were based on compression- and swelling indices, proved to generate the most consistently realistic results.

The results from the investigation indicate that the model S-CLAY1 is capable of generating realistic predictions of horizontal deformations, incurred by excavation processes in soft soil. The model is particularly successful in regions of the soil where plastic strains develop due to negative increments in deviatoric stress. At greater depths, however, where stress increments are small, the assumption of stress-independent isotropic elasticity, along with the model's inability to account for small-strain behavior in the soil, results in over-estimations of the true horizontal deformations. It seems that S-CLAY1 provides a good set of tools for analyzing the deformation behavior of soft soil, in projects where plastic strains are likely to be prominent. Yet, considering that this report is first in addressing the performance of S-CLAY1, in a deformation analysis of an unloading problem, further analyses, performed on other excavations, are recommended. These investigations should preferably include results from triaxial tests, from which essential input parameters could be derived directly from the raw data, as to eliminate errors incurred by assumptions.

HS Small is the model which best represents the curvature of the inclinometer readings used as reference in this investigation. It is the only, out of the four models used in the simulations, which manages to represent the drastic decrease in horizontal deformations, as depth increases in the soil profile. Providing that data, regarding the small strain response of the soil, is available, HS Small is likely to be the best option for analyzing the deformation behavior in a problem, similar to the one assessed in this report, in which deep layers of soil are subjected to unloading. The sensitivity analysis, performed on some of the model's most essential stiffness parameters, did however, shed light on the importance of properly specified soil parameters, since the propagation of simulated deformations seems to be highly dependent on the value of G_0^{ref} and $\gamma_{0.7}$.

For future investigations, it would be interesting if it was to be examined how the procedure used in Method 1, in which stiffness parameters were defined based on the compression- and swelling indices of a soil, compare to the conventional methods, i.e. triaxial tests, used for deriving stiffness parameters for the models HS Small and S-CLAY1. If it can be concluded that C_s and C_c provides sufficient results when used as governing stiffness parameters in deformation analyses, less expensive oedometer tests, with unloading and reloading cycles, could perhaps replace triaxial tests in smaller projects, where economy is particularly important.

It would also be relevant to investigate the role of soil sensitivity, which is accounted for in S-CLAY1S, in the development of deformations in an unloading problem.

11 References

Arvidsson, O., Edstam, T., Hultén, C., Nilsson, G. (2006). *Geotekniska förutsättningar för ökad tappning från Vänern till Göta älv*. Swedish Geotechnical Institute. Available: http://www.swedgeo.se. Accessed: 2013-05-09

Benz, T. (2007). PhD-thesis. *Small-Strain Stiffness of Soils and its Numerical Consequences.* Institut für Geotechnik. Stuttgart. Germany.

Bråten, C., Døssland, Å.L., Gjestvang, M., Kaynia, A.M., Loe, M.M., Løset, Ø. (2010) *Dimesnionering for jordskjelv*. Rådgivende Ingenjørers Forening. Published August 13th 2010.

Craig, R.F. (2004). *Craig´s Soil Mechanics*. 7th edition. Formerly Department of Civil Engineering. University of Dundee, UK. Spon Press, Taylor and Francis Group. London and New York.

Hansbo, S. (1975) *Jordmateriallära – Geoteknik*. Ahlmqvist & Wiksell Förlag AB, Stockholm.

Ismail, A. and Teshome, F. (2011). *Analysis of soil deformations in soft clay due to unloading*. Chalmers University of technology. Division of Geo Engineering. Gothenburg. Sweden.

Karstunen, M., Krenn, H., Wheeler, S.J., Koskinen, M. and Zentar, R. (2005). *Effect of Anisotropy and Destructuration on the Behaviour of Murro Test Embankment*. International Journal of Geomechanics. June 2005, 87-96.

Karstunen, M. (2012). *Soil Modelling and Numerical Analyses*. Lectures notes for MSc in Geotechnics, University of Strathclyde.

Karstunen, M. (2013). Professor in Geotechnics at Chalmers University of Technology. Lecture in soil modeling, held in preparation for this thesis. Date not documented.

Kullingsjö, A. (2013). PhD in Geotechnics at Chalmers University of Technology and at Skanska. Interview during a meeting at Chalmers. Mars 18th 2013.

Koskinen, M., Karstunen, M. and Wheeler, S.J. (2002). *Modelling destructuration and anisotropy of a natural soft clay*. Proc. 5th European Conference of Numerical Methods in Geotechnical Engineering. P. Mestat, ed., Presses de l'ENPC/LCPC, Paris, 11-20.

Kvick, O. (2012). *Horisontella jorddeformationers påverkan på ett pålgrundlagt brofundament i lös lera*. Luleå University of Technology. Department of Civil, Environmental and Natural resources engineering. Luleå. Sweden.

Larsson, R., Mulabdic, M. (1991) *Report No 40 - Shear Moduli in Scandinavian Clays*. Swedish Geotechnical Institute. Linköping. Sweden.

Muir Wood, D. (1990). *Soil Behaviour and Critical State Soil Mechanics*. Cambridge: Cambridge Universtiy Press.

Muir Wood, D. (2009). *Soil Mechanics – A One-Dimensional Introduction*. Cambridge: Cambridge Universtiy Press.

Näätänen, A., Wheeler, S., Karstunen, M. and Lojander, M. (1999). *Experimental investigation of an anisotropic hardening model for soft clays*. In Proceedings of the 2nd International Symposium on Pre-failure Deformation Characteristics of

Geomaterials, Torino, Italy, 28-30 September, Edited by M. Jamiolowski, R. Lancelotta and D. Lo Presti. A.A. Balkema, Rotterdam. pp. 541.548.

Ottosen, N., Petersson, H. (1992). *Introduction to the Finite Element Method.* Pearson Education Limited. Edinburgh Gate. Harlow. Essex CM20 JE. England.

Plaxis. (2012a). *Material Models Manual*. Available at: http://www.plaxis.nl.

Schanz, T., Vermeer, P.A., Bonnier, P.G. (1999). *The hardening Soil Model – Formulation and Verification*. Beyond 2000 in Computational Geotechnincs – 10 Years of Plaxis. Balkema, Rotterdam. Netherlands.

Stokoe, K.H., M.B. Darendeli, R.B. Gilbert, F.-Y. Menq, W.K. Choi. (2004) *Development of a New Family of Normalized Modulus Reduction and Material Damping Curves*. International Workshop on Uncertainties in Non-linear Soil Properties and their Impact on Modeling Dynamic Soil Response, UC Berkeley, CA, USA.

Sällfors, G. (2009). *Geoteknik – Jordmateriallära & Jordmekanik*. 4th edition. Chalmers University of technology. Department of Civil and Environmental Engineering. Divisions of Geo Engineering. Gothenburg. Sweden.

Trafikverket. (2013). *Bana Väg i Väst*. Available: http://www.trafikverket.se. Accessed: 2013-05-07.

Wheeler, S.J., Näätänen, A., Karstunen, M. and Lojander, M. (2003). *An anisotropic elasto-plastic model for soft clays*. Can. Geotech. J., 40(2), 403-418.

Appendices

Excavation 1 – Method 1

Identification		SAND	CLAY 1	CLAY 2	CLAY 3	CLAY 4	CLAY 5	FR.MAT
Material model		Hardening Soil	Hardening Soil	Hardening Soil	Hardening Soil	Hardening Soil	Hardening Soil	Hardening Soil
Drainage type		Drained	Undrained (A)	Undrained (A)	Undrained (A)	Undrained (A)	Undrained (A)	Drained
γ_{unsat}	kN/m^3	18	15,3	15,8	16,3	16,5	16	21
γ_{sat}	kN/m^3	21	15,3	15,8	16,3	16,5	16	21
e_{init}	-	0,5	2,44	2,16	1,84	1,74	1,94	0,5
E_{50}^{ref}	kN/m^2	15000	-	-	-	-	-	40000
E_{oed}^{ref}	kN/m^2	15000	-	-	-	-	-	40000
E_{ur}^{ref}	kN/m^2	45000	-	-	-	-	-	120000
power (m)	-	0,5	1	1	1	1	1	0,5
C_C	-	-	2,141	1,474	1,233	1,169	1,089	-
C_S	-	-	0,07734	0,04818	0,03108	0,0249	0,02442	-
φ' (phi)	°	36	30	30	30	30	30	38
Ψ (psi)	°	6	0	0	0	0	0	8
ν'_{ur}	-	0,2	0,15	0,15	0,15	0,15	0,15	0,2
p_{ref}	kN/m^2	100	25,75	39,8	55,65	79,5	115,7	100
K_0^{nc}	-	0,4122	0,5	0,5	0,5	0,5	0,5	0,3843
R_f	-	0,9	0,9	0,9	0,9	0,9	0,9	0,9
Soil type		Medium	Very fine	Very fine	Very fine	Very fine	Very fine	Course
k_x	m/day	1,00	1,94E-04	1,28E-04	5,18E-05	4,02E-05	5,57E-05	1
k_y	m/day	1,00	1,30E-04	8,51E-05	3,46E-05	2,68E-05	3,72E-05	1
$K_{0,x}$	-	0,41	0,587	0,566	0,545	0,566	0,594	0,3843
OCR	-	1,00	1,38	1,28	1,19	1,28	1,41	1

Identification		SAND	CLAY 1	CLAY 2	CLAY 3	CLAY 4	CLAY 5	FR.MAT
Material model		HS Small	HS Small	HS Small	HS Small	HS Small	HS Small	HS Small
Drainage type		Drained	Undrained (A)	Undrained (A)	Undrained (A)	Undrained (A)	Undrained (A)	Drained
γ_{unsat}	kN/m^3	18,0	15,3	15,8	16,3	16,5	16,0	21
γ_{sat}	kN/m^3	21,0	15,3	15,8	16,3	16,5	16,0	21
e_{init}	-	0,5	2,44	2,16	1,84	1,74	1,94	0,5
E_{50}^{ref}	kN/m^2	15000	-	-	-	-	-	40000
E_{oed}^{ref}	kN/m^2	15000	-	-	-	-	-	40000
E_{ur}^{ref}	kN/m^2	45000	-	-	-	-	-	120000
power (m)	-	0,5	1	1	1	1	1	0,5
C_C	-	-	2,141	1,474	1,233	1,169	1,089	-
C_S	-	-	0,07734	0,04818	0,03108	0,0249	0,02442	-
φ' (phi)	°	36	30	30	30	30	30	38
Ψ (psi)	°	6	0	0	0	0	0	8
ν'_{ur}	-	0,2	0,15	0,15	0,15	0,15	0,15	0,2
p_{ref}	kN/m^2	100	25,75	39,8	55,65	79,5	115,7	100
K_0^{nc}	-	0,41	0,5	0,5	0,5	0,5	0,5	0,384
R_f	-	0,9	0,9	0,9	0,9	0,9	0,9	0,9
Soil type		Medium	Very fine	Very fine	Very fine	Very fine	Very fine	Course
k_x	m/day	1	1,94E-04	1,28E-04	5,18E-05	4,02E-05	5,57E-05	1
k_y	m/day	1	1,30E-04	8,51E-05	3,46E-05	2,68E-05	3,72E-05	1
$K_{0,x}$	-	0,4122	0,587	0,566	0,545	0,566	0,594	0,3843
OCR	-	1	1,38	1,28	1,19	1,28	1,41	1
Small-strain approach		Appr.	Appr./Emp.	Appr./Emp.	Appr./Emp.	Appr./Emp.	Appr./Emp.	Appr.
$\gamma_{0.7}$	-	1,5E-04	1.5E-4/3.4E-4	1.5E-4/3.0E-4	1.5E-4/2.6E-4	1.5E-4/2.4E-4	1.5E-4/2.7E-4	1,50E-04
G_0^{ref}	kN/m^2	117200	6780/8001	15450/12620	30110/23020	51770/31640	82470/32460	312500

Identification		SAND	CLAY 1	CLAY 2	CLAY 3	CLAY 4	CLAY 5	FR.MAT
Material model		HS Small	S-CLAY 1/MCC	S-CLAY 1/MCC	S-CLAY 1/MCC	S-CLAY 1/MCC	S-CLAY 1/MCC	HS Small
Drainage type		Drained	Undrained (A)	Undrained (A)	Undrained (A)	Undrained (A)	Undrained (A)	Drained
γ_{unsat}	kN/m^3	18	15,3	15,8	16,3	16,5	16,0	21
γ_{sat}	kN/m^3	21	15,3	15,8	16,3	16,5	16,0	21
e_{init}	-	0,5	2,44	2,16	1,84	1,74	1,94	0,5
E_{50}^{ref}	kN/m^2	15000	-	-	-	-	-	40000
E_{oed}^{ref}	kN/m^2	15000	-	-	-	-	-	40000
E_{ur}^{ref}	kN/m^2	45000	-	-	-	-	-	120000
power (m)	-	0,5	-	-	-	-	-	0,5
C_C	-	-	-	-	-	-	-	-
C_S	-	-	-	-	-	-	-	-
φ' (phi)	°	36	30	30	30	30	30	30
Ψ (psi)	°	6	0	0	0	0	0	0
$\gamma_{0.7}$	-	1,5E-04	-	-	-	-	-	1,50E-04
G_0^{ref}	kN/m^2	117200	-	-	-	-	-	312500
v'_{ur}	-	0,2	0,15	0,15	0,15	0,15	0,15	0,15
p_{ref}	kN/m^2	100	-	-	-	-	-	100
K_0^{nc}	-	0,4122	-	-	-	-	-	0,3843
R_f	-	0,9	-	-	-	-	-	0,9
Soil type		Medium	Very fine	Very fine	Very fine	Very fine	Very fine	Course
k_x	m/day	1	1,94E-04	1,28E-04	5,18E-05	4,02E-05	5,57E-05	1
k_y	m/day	1	1,30E-04	8,51E-05	3,46E-05	2,68E-05	3,72E-05	1
$K_{0,x}$	-	0,4122	0,587	0,566	0,545	0,566	0,594	0,3843
OCR	-	1	1,38	1,28	1,19	1,28	1,41	1
κ	-	-	0,0713	0,044	0,028	0,023	0,023	-
λ	-	-	0,99	0,67	0,55	0,53	0,51	-
M	-	-	1,2	1,2	1,2	1,2	1,2	-
μ	-	-	35/0	52/0	63/0	65/0	68/0	-
β	-	-	0,76	0,76	0,76	0,76	0,76	-
α_0	-	-	0.46/0	0.46/0	0.46/0	0.46/0	0.46/0	-

Excavation 1 – Method 2

Identification		SAND	CLAY 1	CLAY 2	CLAY 3	CLAY 4	CLAY 5	FR.MAT
Material model		Hardening Soil	Hardening Soil	Hardening Soil	Hardening Soil	Hardening Soil	Hardening Soil	Hardening Soil
Drainage type		Drained	Undrained (A)	Undrained (A)	Undrained (A)	Undrained (A)	Undrained (A)	Drained
γ_{unsat}	kN/m^3	18	15,3	15,8	16,3	16,5	16	21
γ_{sat}	kN/m^3	21	15,3	15,8	16,3	16,5	16	21
e_{init}	-	0,5	2,44	2,16	1,84	1,74	1,94	0,5
E_{50}^{ref}	kN/m^2	15000	5981	7098	7739	7528	7286	40000
E_{oed}^{ref}	kN/m^2	15000	1959	2324	2534	2465	2386	40000
E_{ur}^{ref}	kN/m^2	45000	29900	35490	38700	37640	36430	120000
power (m)	-	0,5	1	1	1	1	1	0,5
C_C	-	-	-	-	-	-	-	-
C_S	-	-	-	-	-	-	-	-
φ' (phi)	°	36	30	30	30	30	30	38
Ψ (psi)	°	6	0	0	0	0	0	8
v'_{ur}	-	0,2	0,15	0,15	0,15	0,15	0,15	0,2
p_{ref}	kN/m^2	100	100	100	100	100	100	100
K_0^{nc}	-	0,4122	0,5	0,5	0,5	0,5	0,5	0,3843
R_f	-	0,9	0,9	0,9	0,9	0,9	0,9	0,9
Soil type		Medium	Very fine	Very fine	Very fine	Very fine	Very fine	Course
k_x	m/day	1	1,94E-04	1,28E-04	5,18E-05	4,02E-05	5,57E-05	1
k_y	m/day	1	1,30E-04	8,51E-05	3,46E-05	2,68E-05	3,72E-05	1
$K_{0,x}$	-	0,4122	0,587	0,566	0,545	0,566	0,594	0,3843
OCR	-	1	1,38	1,28	1,19	1,28	1,41	1

Identification		SAND	CLAY 1	CLAY 2	CLAY 3	CLAY 4	CLAY 5	FR.MAT
Material model		HS Small	HS Small	HS Small	HS Small	HS Small	HS Small	HS Small
Drainage type		Drained	Undrained (A)	Undrained (A)	Undrained (A)	Undrained (A)	Undrained (A)	Drained
γ_{unsat}	kN/m^3	18	15,3	15,8	16,3	16,5	16	21
γ_{sat}	kN/m^3	21	15,3	15,8	16,3	16,5	16	21
e_{init}	-	0,5	2,44	2,16	1,84	1,74	1,94	0,5
E_{50}^{ref}	kN/m^2	15000	5981	7098	7739	7528	7286	40000
E_{oed}^{ref}	kN/m^2	15000	1959	2324	2534	2465	2386	40000
E_{ur}^{ref}	kN/m^2	45000	29900	35490	38700	37640	36430	120000
power (m)	-	0,5	1	1	1	1	1	0,5
C_C	-	-	-	-	-	-	-	-
C_S	-	-	-	-	-	-	-	-
φ' (phi)	°	36	30	30	30	30	30	38
Ψ (psi)	°	6	0	0	0	0	0	8
$\gamma_{0.7}$	-	1,50E-04	1,50E-04	1,50E-04	1,50E-04	1,50E-04	1,50E-04	1,50E-04
G_0^{ref}	kN/m^2	117200	81260	96440	105200	105200	99000	312500
v'_{ur}	-	0,2	0,15	0,15	0,15	0,15	0,15	0,2
p_{ref}	kN/m^2	100	100	100	100	100	100	100
K_0^{nc}	-	0,4122	0,5	0,5	0,5	0,5	0,5	0,3843
R_f	-	0,9	0,9	0,9	0,9	0,9	0,9	0,9
Soil type		Medium	Very fine	Very fine	Very fine	Very fine	Very fine	Course
k_x	m/day	1	1,94E-04	1,28E-04	5,18E-05	4,02E-05	5,57E-05	1
k_y	m/day	1	1,30E-04	8,51E-05	3,46E-05	2,68E-05	3,72E-05	1
$K_{0,x}$	-	0,4122	0,587	0,566	0,545	0,566	0,594	0,3843
OCR	-	1	1,38	1,28	1,19	1,28	1,41	1

Identification		SAND	CLAY 1	CLAY 2	CLAY 3	CLAY 4	CLAY 5	FR.MAT
Material model		HS Small	S-CLAY 1	S-CLAY 1	S-CLAY 1	S-CLAY 1	S-CLAY 1	HS Small
Drainage type		Drained	Undrained (A)	Undrained (A)	Undrained (A)	Undrained (A)	Undrained (A)	Drained
γ_{unsat}	kN/m^3	18	15,3	15,8	16,3	16,5	16	21
γ_{sat}	kN/m^3	21	15,3	15,8	16,3	16,5	16	21
e_{init}	-	0,5	2,44	2,16	1,84	1,74	1,94	0,5
E_{50}^{ref}	kN/m^2	15000	-	-	-	-	-	40000
E_{oed}^{ref}	kN/m^2	15000	-	-	-	-	-	40000
E_{ur}^{ref}	kN/m^2	45000	-	-	-	-	-	120000
power (m)	-	0,5	-	-	-	-	-	0,5
C_C	-	-	-	-	-	-	-	-
C_S	-	-	-	-	-	-	-	-
φ' (phi)	°	36	30	30	30	30	30	38
Ψ (psi)	°	6	0	0	0	0	0	8
$\gamma_{0.7}$	-	1,50E-04	-	-	-	-	-	1,50E-04
G_0^{ref}	kN/m^2	117200	-	-	-	-	-	312500
ν'_{ur}	-	0,2	0,15	0,15	0,15	0,15	0,15	0,2
p_{ref}	kN/m^2	100	-	-	-	-	-	100
K_0^{nc}	-	0,4122	-	-	-	-	-	0,3843
R_f	-	0,9	-	-	-	-	-	0,9
Soil type		Medium	Very fine	Very fine	Very fine	Very fine	Very fine	Course
k_x	m/day	1	1,94E-04	1,28E-04	5,18E-05	4,02E-05	5,57E-05	1
k_y	m/day	1	1,30E-04	8,51E-05	3,46E-05	2,68E-05	3,72E-05	1
$K_{0,x}$	-	0,4122	0,587	0,566	0,545	0,566	0,594	0,3843
OCR	-	1	1,38	1,28	1,19	1,28	1,41	1
κ	-	-	0,023	0,018	0,015	0,015	0,016	-
λ	-	-	0,36	0,25	0,2	0,2	0,22	-
M	-	-	1,2	1,2	1,2	1,2	1,2	-
μ	-	-	42	59	74	76	69	-
β	-	-	0,76	0,76	0,76	0,76	0,76	-
α_0	-	-	0,46	0,46	0,46	0,46	0,46	-

Excavation 2 – Method 1

Identification		SAND	CLAY 1	CLAY 2	CLAY 3	CLAY 4	FR.MAT
Material model		Hardening Soil	Hardening Soil	Hardening Soil	Hardening Soil	Hardening Soil	Hardening Soil
Drainage type		Drained	Undrained (A)	Undrained (A)	Undrained (A)	Undrained (A)	Drained
γ_{unsat}	kN/m^3	18	15,3	15,5	16	15,9	21
γ_{sat}	kN/m^3	21	15,3	15,5	16	15,9	21
e_{init}	-	0,5	2,37	2,29	1,98	1,94	0,5
E_{50}^{ref}	kN/m^2	15000	-	-	-	-	40000
E_{oed}^{ref}	kN/m^2	15000	-	-	-	-	40000
E_{ur}^{ref}	kN/m^2	45000	-	-	-	-	120000
power (m)	-	0,5	1	1	1	1	0,5
C_C	-	-	1,85	1,75	1,22	1,27	-
C_S	-	-	0,042	0,037	0,032	0,053	-
φ' (phi)	°	36	30	30	30	30	38
Ψ (psi)	°	6	0	0	0	0	8
v'_{ur}	-	0,2	0,15	0,15	0,15	0,15	0,2
p_{ref}	kN/m^2	100	25,2	33,86	49,15	91,45	100
K_0^{nc}	-	0,4122	0,5	0,5	0,5	0,5	0,3843
R_f	-	0,9	0,9	0,9	0,9	0,9	0,9
Soil type		Medium	Very fine	Very fine	Very fine	Very fine	Course
k_x	m/day	1	1,89E-04	8,39E-05	5,05E-05	4,80E-05	1
k_y	m/day	1	1,26E-04	5,59E-05	3,37E-05	3,20E-05	1
$K_{0,x}$	-	0,4122	0,589	0,505	0,502	0,545	0,3843
OCR	-	1	1,39	1,02	1,01	1,19	1

Identification		SAND	CLAY 1	CLAY 2	CLAY 3	CLAY 4	FR.MAT
Material model		HS Small	HS Small	HS Small	HS Small	HS Small	HS Small
Drainage type		Drained	Undrained (A)	Undrained (A)	Undrained (A)	Undrained (A)	Drained
γ_{unsat}	kN/m^3	18	15,3	15,5	16	15,9	21
γ_{sat}	kN/m^3	21	15,3	15,5	16	15,9	21
e_{init}	-	0,5	2,37	2,29	1,98	1,94	0,5
E_{50}^{ref}	kN/m^2	15000	-	-	-	-	40000
E_{oed}^{ref}	kN/m^2	15000	-	-	-	-	40000
E_{ur}^{ref}	kN/m^2	45000	-	-	-	-	120000
power (m)	-	0,5	1	1	1	1	0,5
C_C	-	-	1,85	1,75	1,22	1,27	-
C_S	-	-	0,043	0,042	0,04	0,053	-
φ' (phi)	°	36	30	30	30	30	38
Ψ (psi)	°	6	0	0	0	0	8
$\gamma_{0.7}$	-	1,50E-04	1,50E-04	1,50E-04	1,50E-04	1,50E-04	1,50E-04
G_0^{ref}	kN/m^2	117200	11690	15700	21670	44210	312500
v'_{ur}	-	0,2	0,15	0,15	0,15	0,15	0,2
p_{ref}	kN/m^2	100	25,2	33,86	49,15	91,45	100
K_0^{nc}	-	0,4122	0,5	0,5	0,5	0,5	0,3843
R_f	-	0,9	0,9	0,9	0,9	0,9	0,9
Soil type		Medium	Very fine	Very fine	Very fine	Very fine	Course
k_x	m/day	1	1,89E-04	8,39E-05	5,05E-05	4,80E-05	1
k_y	m/day	1	1,26E-04	5,59E-05	3,37E-05	3,20E-05	1
$K_{0,x}$	-	0,4122	0,589	0,505	0,502	0,545	0,3843
OCR	-	1	1,39	1,02	1,01	1,19	1

Identification		SAND	CLAY 1	CLAY 2	CLAY 3	CLAY 4	FR.MAT
Material model		HS Small	S-CLAY 1/MCC	S-CLAY 1/MCC	S-CLAY 1/MCC	S-CLAY 1/MCC	HS Small
Drainage type		Drained	Undrained (A)	Undrained (A)	Undrained (A)	Undrained (A)	Drained
γ_{unsat}	kN/m^3	18	15,3	15,5	16	15,9	21
γ_{sat}	kN/m^3	21	15,3	15,5	16	15,9	21
e_{init}	-	0,5	2,37	2,29	1,98	1,94	0,5
E_{50}^{ref}	kN/m^2	15000	-	-	-	-	40000
E_{oed}^{ref}	kN/m^2	15000	-	-	-	-	40000
E_{ur}^{ref}	kN/m^2	45000	-	-	-	-	120000
power (m)	-	0,5	-	-	-	-	0,5
C_C	-	-	-	-	-	-	-
C_S	-	-	-	-	-	-	-
φ' (phi)	°	36	30	30	30	30	38
Ψ (psi)	°	6	0	0	0	0	8
$\gamma_{0.7}$	-	1,50E-04	-	-	-	-	1,50E-04
G_0^{ref}	kN/m^2	117200	-	-	-	-	312500
ν'_{ur}	-	0,2	0,15	0,15	0,15	0,15	0,2
p_{ref}	kN/m^2	100	-	-	-	-	100
K_0^{nc}	-	0,4122	-	-	-	-	0,3843
R_f	-	0,9	-	-	-	-	0,9
Soil type		Medium	Very fine	Very fine	Very fine	Very fine	Course
k_x	m/day	1	1,89E-04	8,39E-05	5,05E-05	4,80E-05	1
k_y	m/day	1	1,26E-04	5,59E-05	3,37E-05	3,20E-05	1
$K_{0,x}$	-	0,4122	0,589	0,505	0,502	0,545	0,3843
OCR	-	1	1,39	1,02	1,01	1,19	1
κ	-	-	0,037	0,037	0,035	0,031	-
λ	-	-	0,81	0,76	0,53	0,55	-
M	-	-	1,2	1,2	1,2	1,2	-
μ	-	-	19/0	20/0	28/0	27/0	-
β	-	-	0,76	0,76	0,76	0,76	-
α_0	-	-	0,46/0	0,46/0	0,46/0	0,46/0	-

Excavation 2 – Method 2

Identification		SAND	CLAY 1	CLAY 2	CLAY 3	CLAY 4	FR.MAT
Material model		Hardening Soil	Hardening Soil	Hardening Soil	Hardening Soil	Hardening Soil	Hardening Soil
Drainage type		Drained	Undrained (A)	Undrained (A)	Undrained (A)	Undrained (A)	Drained
γ_{unsat}	kN/m^3	18	15,3	15,5	16	15,9	21
γ_{sat}	kN/m^3	21	15,3	15,5	16	15,9	21
e_{init}	-	0,5	2,37	2,29	1,98	1,94	0,5
E_{50}^{ref}	kN/m^2	15000	1196	1830	2719	4878	40000
E_{oed}^{ref}	kN/m^2	15000	956,9	600	891	1937	40000
E_{ur}^{ref}	kN/m^2	45000	23920	9148	13600	24390	120000
power (m)	-	0,5	1	1	1	1	0,5
C_C	-	-	-	-	-	-	-
C_S	-	-	-	-	-	-	-
φ' (phi)	°	36	30	30	30	30	38
Ψ (psi)	°	6	0	0	0	0	8
v'_{ur}	-	0,2	0,15	0,15	0,15	0,15	0,2
p_{ref}	kN/m^2	100	100	100	100	100	100
K_0^{nc}	-	0,4122	0,5	0,5	0,5	0,5	0,3843
R_f	-	0,9	0,9	0,9	0,9	0,9	0,9
Soil type		Medium	Very fine	Very fine	Very fine	Very fine	Course
k_x	m/day	1	1,89E-04	8,39E-05	5,05E-05	4,80E-05	1
k_y	m/day	1	1,26E-04	5,59E-05	3,37E-05	3,20E-05	1
$K_{0,x}$	-	0,4122	0,6262	0,5065	0,5032	0,5615	0,3843
OCR	-	1	1,39	1,02	1,01	1,19	1

Identification		SAND	CLAY 1	CLAY 2	CLAY 3	CLAY 4	FR.MAT
Material model		HS Small	HS Small	HS Small	HS Small	HS Small	HS Small
Drainage type		Drained	Undrained (A)	Undrained (A)	Undrained (A)	Undrained (A)	Drained
γ_{unsat}	kN/m^3	18	15,3	15,5	16	15,9	21
γ_{sat}	kN/m^3	21	15,3	15,5	16	15,9	21
e_{init}	-	0,5	2,37	2,29	1,98	1,94	0,5
E_{50}^{ref}	kN/m^2	15000	1562	1830	2719	4878	40000
E_{oed}^{ref}	kN/m^2	15000	512	600	891	1937	40000
E_{ur}^{ref}	kN/m^2	45000	7810	9148	13600	2439	120000
power (m)	-	0,5	1	1	1	1	0,5
C_C	-	-	-	-	-	-	-
C_S	-	-	-	-	-	-	-
φ' (phi)	°	36	30	30	30	30	38
Ψ (psi)	°	6	0	0	0	0	8
$\gamma_{0.7}$	-	1,50E-04	1,50E-04	1,50E-04	1,50E-04	1,50E-04	1,50E-04
G_0^{ref}	kN/m^2	117200	21220	24860	36950	66280	312500
v'_{ur}	-	0,2	0,15	0,15	0,15	0,15	0,2
p_{ref}	kN/m^2	100	100	100	100	100	100
K_0^{nc}	-	0,4122	0,5	0,5	0,5	0,5	0,3843
R_f	-	0,9	0,9	0,9	0,9	0,9	0,9
Soil type		Medium	Very fine	Very fine	Very fine	Very fine	Course
k_x	m/day	1	1,89E-04	8,39E-05	5,05E-05	4,80E-05	1
k_y	m/day	1	1,26E-04	5,59E-05	3,37E-05	3,20E-05	1
$K_{0,x}$	-	0,4122	0,6262	0,5065	0,5032	0,5615	0,3843
OCR	-	1	1,39	1,02	1,01	1,19	1

Identification		SAND	CLAY 1	CLAY 2	CLAY 3	CLAY 4	FR.MAT
Material model		HS Small	S-CLAY 1	S-CLAY 1	S-CLAY 1	S-CLAY 1	HS Small
Drainage type		Drained	Undrained (A)	Undrained (A)	Undrained (A)	Undrained (A)	Drained
γ_{unsat}	kN/m^3	18	15,3	15,5	16	15,9	21
γ_{sat}	kN/m^3	21	15,3	15,5	16	15,9	21
e_{init}	-	0,5	2,37	2,29	1,98	1,94	0,5
E_{50}^{ref}	kN/m^2	15000	-	-	-	-	40000
E_{oed}^{ref}	kN/m^2	15000	-	-	-	-	40000
E_{ur}^{ref}	kN/m^2	45000	-	-	-	-	120000
power (m)	-	0,5	-	-	-	-	0,5
C_C	-	-	-	-	-	-	-
C_S	-	-	-	-	-	-	-
φ' (phi)	°	36	30	30	30	30	38
Ψ (psi)	°	6	0	0	0	0	8
$\gamma_{0.7}$	-	1,50E-04	-	-	-	-	1,50E-04
G_0^{ref}	kN/m^2	117200	-	-	-	-	312500
ν'_{ur}	-	0,2	0,15	0,15	0,15	0,15	0,2
p_{ref}	kN/m^2	100	-	-	-	-	100
K_0^{nc}	-	0,4122	-	-	-	-	0,3843
R_f	-	0,9	-	-	-	-	0,9
Soil type		Medium	Very fine	Very fine	Very fine	Very fine	Course
k_x	m/day	1	1,89E-04	8,39E-05	5,05E-05	4,80E-05	1
k_y	m/day	1	1,26E-04	5,59E-05	3,37E-05	3,20E-05	1
$K_{0,x}$	-	0,4122	0,6262	0,5065	0,5032	0,5615	0,3843
OCR	-	1	1,39	1,02	1,01	1,19	1
κ	-	-	0,086	0,072	0,044	0,024	-
λ	-	-	1,36	0,9	0,45	0,15	-
M	-	-	1,2	1,2	1,2	1,2	-
μ	-	-	43	45	65	63	-
β	-	-	0,76	0,76	0,76	0,76	-
α_0	-	-	0,46	0,46	0,46	0,46	-